

POLITECNICO DI TORINO

Master's degree in Civil Engineering



Master's Degree Thesis

**Thermo-active tunnels: numerical
insights on the role of the internal air**

Supervisors:

Prof. Marco Barla

Ing. Alessandra Insana

Candidate:

Chixuan Liu

December 2020

Summary

The thesis investigates the effect of the thermal activation of tunnel linings on the temperature of internal air. Previously, an in-situ experimental campaign named Enertun prototype, which provides plenty of experimental data for this thesis, was run in the Turin Metro Line 1 south extension project, where two rings of lining were thermally activated with pipe circuit circulating heat conduct fluid. Thermal activation tests of linings with different working modes at different time in the year were performed and in-situ experimental data regarding the thermal performance of the thermo-active tunnel was recorded. By implementing a finite-element software with hydro-thermal analysis function, a 3D finite-element model was built up replicating the internal geometry of the Enertun prototype. With the in-situ experimental data measured with different working mode and different operation parameters at different time in the year, the material properties and boundary conditions used in the numerical model were calibrated and validated. Afterwards, the numerical model is upgraded into the one with 6 rings of linings all equipped with pipe circuit so to study the energy performance of the tunnel when being fully thermally activated. Different simplified input time series of temperature are implemented to understand the performance under different climate conditions while different thermal activation modes are implemented to better understand the response of the internal air.

Acknowledgements

Here I would like to thank sincerely Prof. Marco Barla and Dr. Alessandra Insana for the supports and information during this year. Energy tunnel is always an interesting and promising topic for me, so I am grateful for being able to put my effort on it. Hopefully, this concept will be realized globally in the future to have a more efficient use of the shallow geothermal energy. Special thanks to my families and my friends for the supports in life and to Politecnico di Torino for all the supports for my study.

Content

| | |
|---|-------------|
| List of Figure | V |
| List of Table..... | VIII |
| Chapter 1 Shallow geothermal energy | 1 |
| 1.1 Introduction | 1 |
| 1.2 History of Shallow geothermal energy | 3 |
| 1.3 System exploiting shallow geothermal energy | 5 |
| 1.3.1 Classification of underground thermal energy storage | 5 |
| 1.3.2 Characteristics of underground storage system | 8 |
| 1.4 Advantages and Limitation | 9 |
| 1.4.1 Advantages | 10 |
| 1.4.2 Limitation | 10 |
| Chapter 2 Energy geostructures and tunnels | 11 |
| 2.1 Definition and principle of energy geostructures | 11 |
| 2.2 Classifications of geostructures by realization technology | 11 |
| 2.3 Advantages of energy tunnels..... | 11 |
| 2.4 Classifications of energy tunnels | 12 |
| 2.5 Related research projects about energy tunnels..... | 12 |
| 2.6 A prototype of energy tunnel with Enertun configuration | 14 |
| 2.7 Required analysis for the application of energy tunnels | 17 |
| 2.7.1 Calculation of exploitable heat..... | 17 |
| 2.7.2 Thermo-hydraulic (TH) coupled analysis | 17 |
| 2.7.3 Thermo-mechanical (TM) coupled analysis..... | 20 |
| Chapter 3 A 3D finite-element analysis software | 23 |
| 3.1 Introduction | 23 |
| 3.2 Typical process of model realization in FEFLOW | 24 |
| 3.2.1 Supermesh design..... | 24 |
| 3.2.2 Finite-element mesh | 25 |
| 3.2.3 Problem setting | 26 |
| 3.2.4 Selections | 27 |
| 3.2.5 Parameter Assignment | 27 |
| 3.2.6 Inspection..... | 30 |
| 3.2.7 Simulation | 30 |
| Chapter 4 Numerical insight on the thermal behavior of the Enertun prototype | 31 |
| 4.1 Introduction | 31 |
| 4.2 Introduction of Enertun prototype..... | 31 |
| 4.3 Realization of the geometry of Enertun Prototype..... | 33 |
| 4.4 Calibration and validation of the Enertun numerical model..... | 38 |
| 4.4.1 Verification with the air finite elements inactive..... | 38 |
| 4.4.2 Verification with the air finite elements active | 45 |

| | |
|---|-----------|
| 4.5 Conclusions from the calibration and validation tests | 51 |
| Chapter 5 Influence of the thermal activation on the internal air temperature of tunnel..... | 52 |
| 5.1 Introduction | 52 |
| 5.2 Simplified input time series of temperature..... | 52 |
| 5.3 Response on thermal activation with ground configuration | 55 |
| 5.3.1 Simulation test introduction..... | 55 |
| 5.3.2 Interpretation of simulation test result..... | 55 |
| 5.4 Response on thermal activation with Air configuration..... | 66 |
| 5.4.1 Simulation test introduction..... | 66 |
| 5.4.2 Interpretation of simulation test result..... | 66 |
| 5.5 Conclusions from the simulation tests | 79 |
| Conclusions..... | 80 |
| Reference | 82 |

List of Figure

| | |
|--|----|
| Fig. 1. Temperature variations with depth in Nicosia, Cyprus (Florides and Kalogirou, 2007)..... | 2 |
| Fig. 2. Typical temperature profile recorded along the borehole depth in the four capital cities in Yangtze River Basin (Wang et al., 2019). | 2 |
| Fig. 3. Underground temperatures at the Royal Edinburgh Observatory, average 1838-1854 (Sanner, 2017). | 3 |
| Fig. 4. Schematic of the first known geothermal heat pump of 1945 (Crandall, 1946). | 4 |
| Fig. 5. Ground-coupling methods available in 1947 (Kemler, 1947)..... | 4 |
| Fig. 6. Classification of underground cold storage alternatives (Sanner and Nordell, 1998) | 5 |
| Fig. 7. Operational modes of cold storage UTES with heat pumps (Sanner and Nordell, 1998)..... | 6 |
| Fig. 8. Schematic of underground thermal storage open system (Sanner, 2017). | 7 |
| Fig. 9. Schematic of underground thermal storage closed system (Borehole heat exchangers) (Sanner, 2017)..... | 8 |
| Fig. 10. Schematic representation of a tunnel segmental lining equipped as ground heat exchanger (Barla and Perino, 2014; Barla et al., 2016)..... | 12 |
| Fig. 11. Energy geotextile (geocomposite) installed in an energy tunnel between primary and secondary linings (Brandl, 2006)..... | 13 |
| Fig. 12. Schematic view of the tunnel heating system using geothermal energy (Zhang et al., 2013)..... | 14 |
| Fig. 13. Different configurations of the new energy segmental lining ENERTUN: (a) ground&air, (b) ground and (c) air (Barla & Di Donna, 2018). | 15 |
| Fig. 14. Example of steel cage equipped with pipes before casting (Barla et al., 2018). | 16 |
| Fig. 15. 3D view of the pipes circuit (Insana and Barla, 2020). | 18 |
| Fig. 16. Updated preliminary design charts showing geothermal potential in W/m ² for winter and summer conditions and for different groundwater flow directions with respect to the tunnel axis (0°, 45° and 90°) (Insana and Barla, 2020). | 20 |
| Fig. 17. Example of a FDM mesh for thermo mechanical analyses of the tunnel lining (Barla and Di Donna, 2018). | 22 |
| Fig. 18. User interface of FEFLOW | 23 |
| Fig. 19. Manual and map-based workflows for the generation of different mesh types | 24 |
| Fig. 20. Different types of mesh in FEFLOW (Triangle, Advancing Front, GridBuilder, Transport Mapping, respectively, from Top Left to Bottom Right) | 26 |
| Fig. 21. Problem Settings dialog of FEFLOW..... | 26 |
| Fig. 22. Different groups of input parameters in FEFLOW | 27 |
| Fig. 23. Process Variables in FEFLOW | 28 |
| Fig. 24. Boundary Conditions in FEFLOW | 28 |
| Fig. 25. Material properties in FEFLOW | 29 |

| | |
|---|----|
| Fig. 26. Discrete Features in FEFLOW | 30 |
| Fig. 27. Turin Metro Line 1 and the location of the Enertun prototype (Barla et al., 2018). | 31 |
| Fig. 28. Cross section of tunnel (Barla et al., 2018). | 32 |
| Fig. 29. Geometry of tunnel lining and grout in Autocad | 34 |
| Fig. 30. Geometry Supermesh in FEFLOW | 34 |
| Fig. 31. Detail of the tunnel lining and internal air Supermesh in FEFLOW | 34 |
| Fig. 32. 2D finite-element mesh in FEFLOW | 35 |
| Fig. 33. Definition of 3D model in FEFLOW | 35 |
| Fig. 34. Heat carrier pipe 2D layout..... | 36 |
| Fig. 35. 3D geometry of heat carrier pipe in Autocad | 36 |
| Fig. 36. Heat carrier pipes of Ground configuration in two middle lining rings modeled as discrete feature in FEFLOW | 37 |
| Fig. 37. Heat carrier pipes of Air configuration in two middle lining rings modeled as discrete feature in FEFLOW..... | 37 |
| Fig. 38. Active and inactive elements | 38 |
| Fig. 39. Hydraulic boundary conditions | 40 |
| Fig. 40. Groundwater table of the modeled domain (suggested from calculated fluid pressure)..... | 40 |
| Fig. 41. Heat transfer BC at the intrados of lining | 41 |
| Fig. 42. Calibration phase check compared with measured data and reference data | 42 |
| Fig. 43. Validation phase check compared with measured data and reference data | 43 |
| Fig. 44. Relative position of the lining temperature sensors in the numerical model | 43 |
| Fig. 45. Lining temperature comparison (Sensor-Sl2) | 44 |
| Fig. 46. Lining temperature comparison (Sensor-St4)..... | 44 |
| Fig. 47. Heat-transfer BC for internal air..... | 46 |
| Fig. 48. Temperature BC for internal air | 46 |
| Fig. 49. Comparison between the calculated temperature of the internal air in the center of the middle length of the tunnel model under two different Heat-transport BC and the measured tunnel temperature (Observation point A at the center of tunnel in slice 43 in the model, which is the middle slice, seen as the orange point in the plot)..... | 47 |
| Fig. 50. calibration phase check of the new model | 48 |
| Fig. 51. Validation phase check of the new model | 49 |
| Fig. 52. Lining temperature comparison (Sensor-Sl2) | 50 |
| Fig. 53. Lining temperature comparison (Sensor-St4) | 50 |
| Fig. 54. Numerical model with 6 rings of heat carrier pipes (only ground configuration is shown) | 52 |
| Fig. 55. Simplified Annual temperature of air and tunnel in Turin | 53 |
| Fig. 56. Simplified inlet temperature (Ground & Air configuration)..... | 54 |
| Fig. 57. Observation points in slice 43 | 54 |
| Fig. 58. Temperature field of the 3D model - Test 1 | 56 |

| | |
|--|----|
| Fig. 59. Temperature variation at observation points A&B - Test 1..... | 57 |
| Fig. 60. Temperature variation at observation points A&B - Test 2..... | 57 |
| Fig. 61. Temperature variation at observation points A&B - Test 3..... | 58 |
| Fig. 62. Temperature field of the 3D model - Test 4..... | 59 |
| Fig. 63. Temperature variation at observation points A&B - Test 4..... | 59 |
| Fig. 64. Temperature variation at observation points A&B - Test 5..... | 60 |
| Fig. 65. Temperature variation at observation points A&B - Test 6..... | 61 |
| Fig. 66. Temperature field of the 3D model - Test 7..... | 62 |
| Fig. 67. Temperature variation at observation points A&B - Test 7..... | 62 |
| Fig. 68. Temperature variation at observation points A&B - Test 8..... | 63 |
| Fig. 69. Temperature variation at observation points A&B - Test 9..... | 64 |
| Fig. 70. Temperature field of the 3D model - Test 10..... | 67 |
| Fig. 71. Temperature variation at observation points A&B - Test 10..... | 67 |
| Fig. 72. Temperature variation at observation points A&B - Test 11..... | 68 |
| Fig. 73. Temperature variation at observation points A&B - Test 12..... | 69 |
| Fig. 74. Temperature field of the 3D model - Test 13..... | 69 |
| Fig. 75. Temperature variation at observation points A&B - Test 13..... | 70 |
| Fig. 76. Temperature variation at observation points A&B - Test 14..... | 71 |
| Fig. 77. Temperature variation at observation points A&B - Test 15..... | 72 |
| Fig. 78. Temperature field of the 3D model - Test 16..... | 72 |
| Fig. 79. Temperature variation at observation points A&B - Test 16..... | 73 |
| Fig. 80. Temperature variation at observation points A&B - Test 17..... | 74 |
| Fig. 81. Temperature variation at observation points A&B - Test 18..... | 74 |
| Fig. 82. Temperature variation at observation points A&B - Test 19..... | 76 |
| Fig. 83. Temperature variation at observation points A&B - Test 20..... | 77 |

List of Table

| | |
|--|----|
| Table 1 List of performed tests (Insana and Barla, 2020). | 33 |
| Table 2 Material properties used for model comparison (Insana and Barla, 2020) | 39 |
| Table 3 Material properties for calibration phase of the numerical model | 45 |
| Table 4 Simulation tests information (Ground configuration) | 55 |
| Table 5 Test interpretation result summary (Observation point A, Ground configuration)..... | 65 |
| Table 6 Test interpretation result summary (Observation point B, Ground configuration)..... | 65 |
| Table 7 Simulation tests information (Air configuration) | 66 |
| Table 8 Test interpretation result summary (Observation point A, Air configuration) | 77 |
| Table 9 Test interpretation result summary (Observation point B, Air configuration) | 78 |

Chapter 1

Shallow geothermal energy

1.1 Introduction

Currently, the energy supply relies highly on fossil fuel resources. However, due to the limited reserve of such kind of energy, the cost to exploit it is increasingly expensive. Moreover, the combustion of fossil fuel leads to the vast emission of CO₂, SO₂ and NO_x, which aggravates the greenhouse effect and pollutes the environment.

Being aware of the seriousness of the pollution and global warming, people is urgently seeking for alternative energy that is sustainable and reliable to meet the sustainability of economy and environment. Underground geothermal energy is one of the alternative energies in the list.

Among different types of underground geothermal energy, Shallow Geothermal Energy (SGE) is an excellent one. Thermal energy is passively stored into (or extracted from) ground and groundwater in different quantity following the seasonal changes. Hence, the ground together with the groundwater can work as a geothermal energy storage.

Beneath a depth of 10-15m, the ground temperature will not be influenced by the seasonal change but keep nearly constant at annual mean air temperature, which varies from 5-25 °C, while in Europe from 8 °C to 16 °C. Consequently, the ground temperature is lower than the air temperature in the summer and higher than the air temperature in the winter. This fact makes it possible to exploit the thermal energy of shallow ground by extracting heat from shallow ground in winter and injecting heat in summer.

The variation of temperature at different depths in summer and winter in Nicosia, Cyprus is shown in **Fig. 1** (Florides and Kalogirou, 2007). That measured in different cities in Yangtze River Basin, China is shown in **Fig. 2** (Wang et al., 2019). Such constant temperature of the shallow ground is proven among different cities around the world.

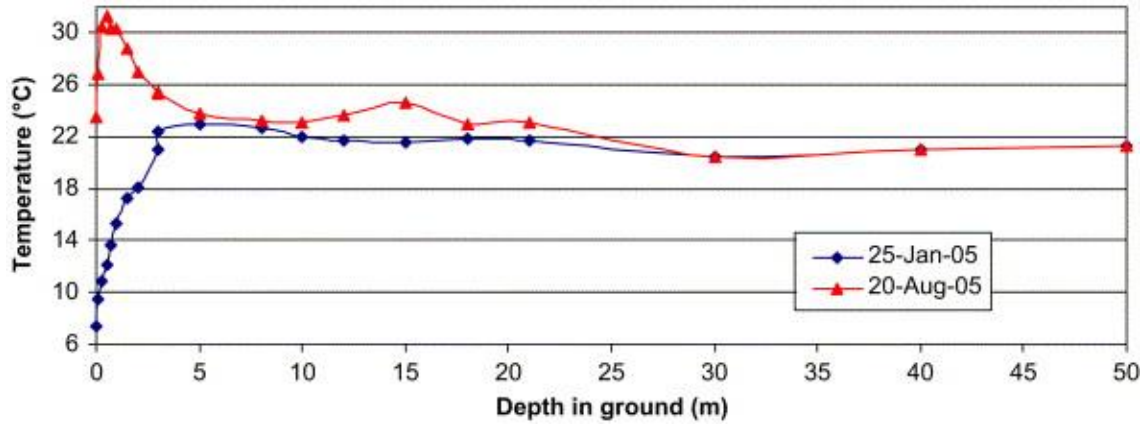


Fig. 1. Temperature variations with depth in Nicosia, Cyprus (Florides and Kalogirou, 2007).

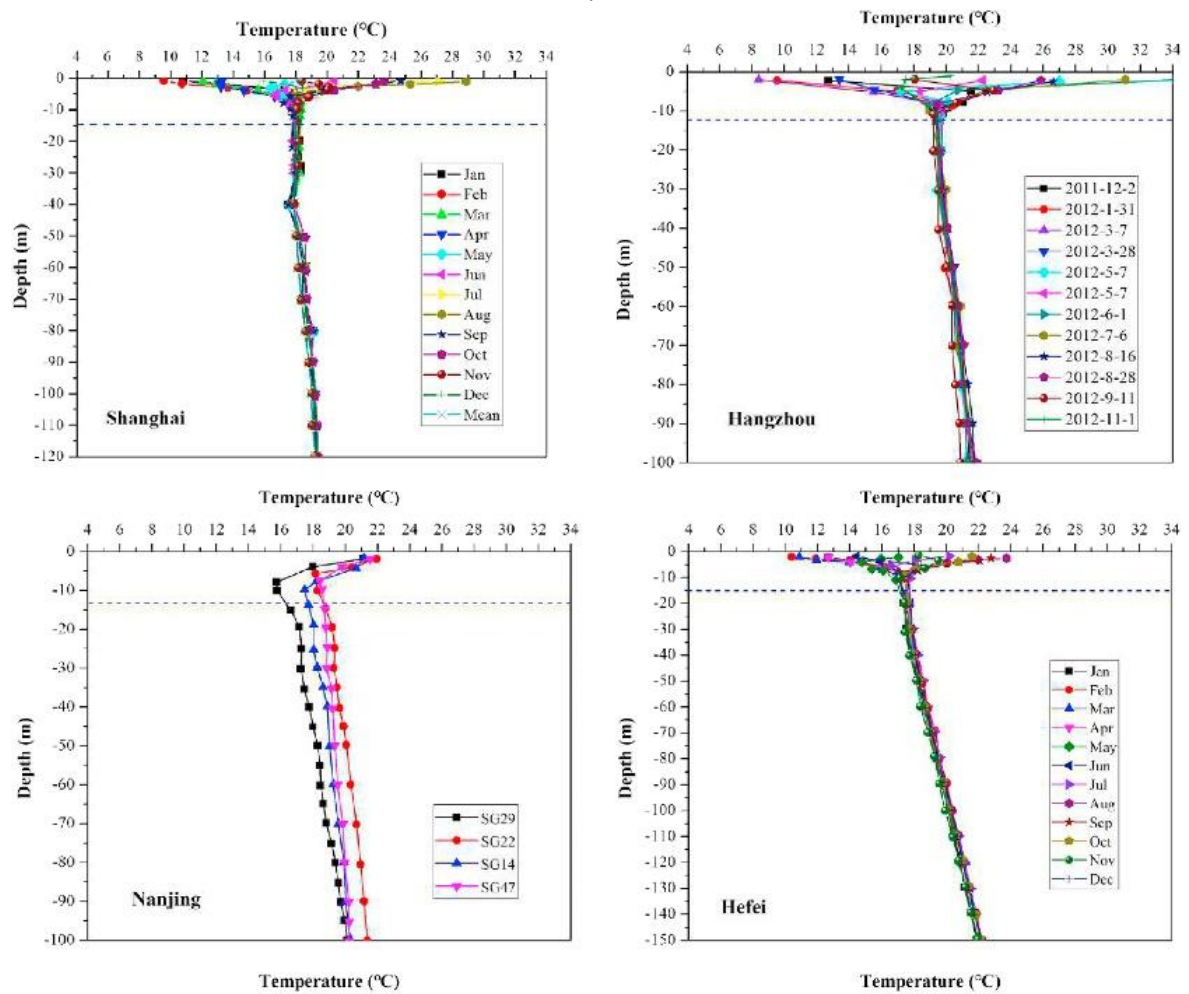


Fig. 2. Typical temperature profile recorded along the borehole depth in the four capital cities in Yangtze River Basin (Wang et al., 2019).

1.2 History of Shallow geothermal energy

A constant temperature in the underground was first proven in the seventeenth century by Lavoisier, a French physicist and chemist. He installed a thermometer in the deep vaults beneath the Paris Observatory at a depth of approximately 20m below street level. In 1778, Buffon reported that the temperature reading measured with this thermometer kept constant throughout the year. Following that, in 1799, Humboldt noted that the mean annual underground temperature in Paris equals 12 °C with a variation of no more than 0.024 °C (Lee, 2013).

Years later, an exact measurement of ground temperature was done since 1838 over many years on the grounds of the Royal Observatory in Edinburgh, Scotland. The result is shown in **Fig. 3** (Sanner, 2017).

In 1945, a ground-source heat pump equipped with 3 circuits totalling 152 m and a compressor with 2.2 kW, exploiting shallow geothermal energy, was first installed in Indianapolis, USA. From the monitoring data of it from October 1945 to May 1946, it was estimated that approximately 5.1 tons of coal were saved due to the application of this heat pump compared to conventional heating during 1630 operating hours in this winter with lows of -24 °C (Sanner, 2017). The schematic of this first known heat pump is shown in **Fig. 4** (Crandall, 1946).

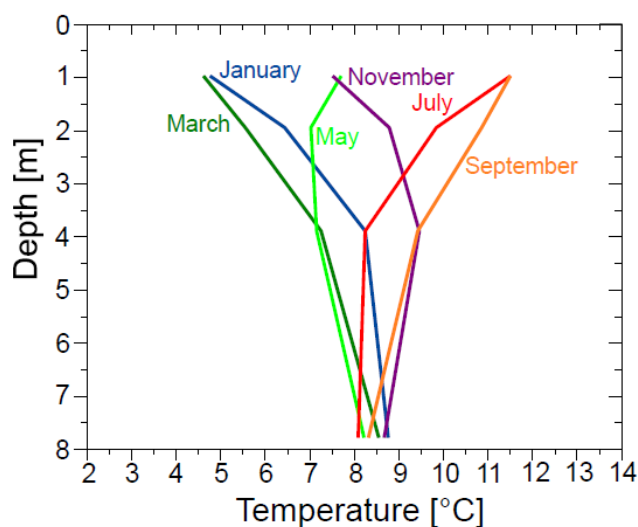


Fig. 3. Underground temperatures at the Royal Edinburgh Observatory, average 1838-1854 (Sanner, 2017).

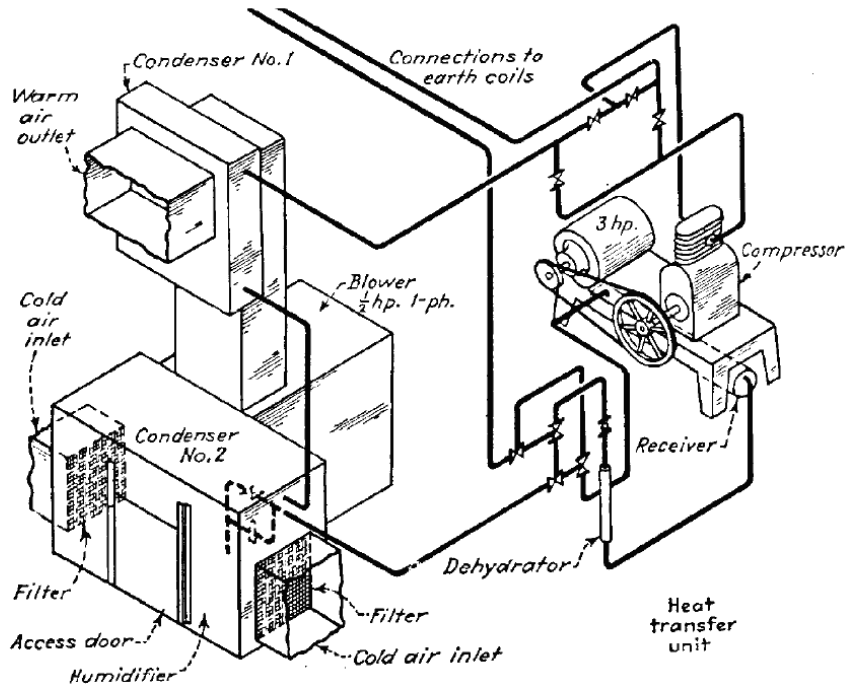


Fig. 4. Schematic of the first known geothermal heat pump of 1945 (Crandall, 1946).

Back at that time, different schematics of heat pump were designed and available for use. Kemler (1947) summarized and listed them in his article including vertical U-pipes, coaxial pipes, helicoidal pipes, horizontal pipes and groundwater wells, which will be shown in **Fig. 5**.

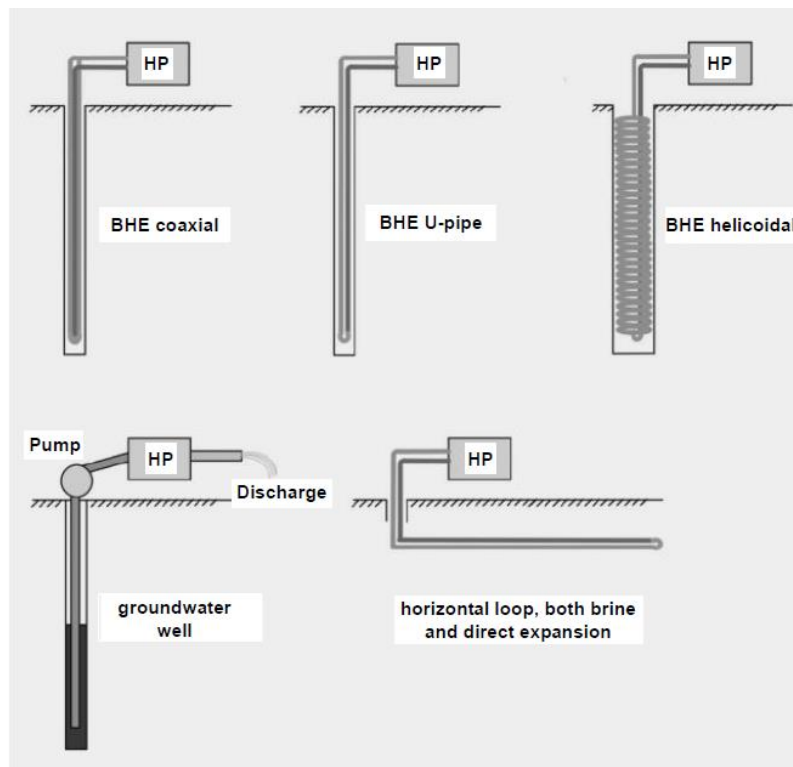


Fig. 5. Ground-coupling methods available in 1947 (Kemler, 1947).

1.3 System exploiting shallow geothermal energy

Demand and supply of energy are variable throughout the year. Underground can work as a thermal energy storage (TES) to buffer the fluctuation of variability of energy demand and energy supply (Lee, 2013).

Since the temperature of the shallow ground keeps constant throughout year, in summer when the air temperature is higher than that of underground energy will be stored into underground while energy will be extracted in winter. Such system using underground as a natural energy storage is called underground thermal energy storage (UTES).

1.3.1 Classification of underground thermal energy storage

1.3.1.1 Storage temperature

UTES can be classified according to different aspects, one of which is in terms of storage temperature (low or high).

High-temperature UTES systems are characterized by a storage temperature of over 40-50 °C, which takes usually solar collectors or waste heat as heat sources.

In this thesis, low temperature UTES will be focused since the application of energy tunnel exploiting shallow geothermal energy pertains to this concept.

The storage temperature of low-temperature UTES (also called cold storage system) ranges from 0 °C to a maximum of 40-50 °C. Such system can be used for cooling, combined cooling and heating, and low-temperature heating. Heat pump can be implemented in the system. The concept of ground source heat pumps (GSHP) is similar to UTES and the distinction between is vague. GSHP is somehow special application of UTES.

Sanner and Nordell (1998) classified cold storage systems into different groups as shown in **Fig. 6**.

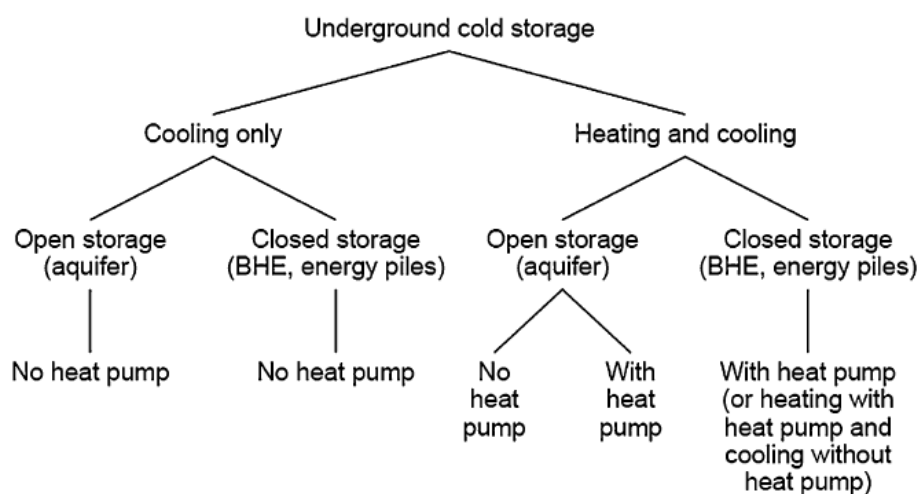


Fig. 6. Classification of underground cold storage alternatives (Sanner and Nordell, 1998)

Furthermore, three possible working modes of underground cold storage system together with a heat pump were summarized as mode 1, mode 2 (direct cooling only) and mode 3 (cooling with heat pump only) seen in **Fig. 7**. They can operate in either mode 1 and mode 2, mode 1 and mode 3, or all the three modes (direct cooling in spring and during low demand, cooling by heat pump in summer or during peak demand) (Sanner and Nordell, 1998).

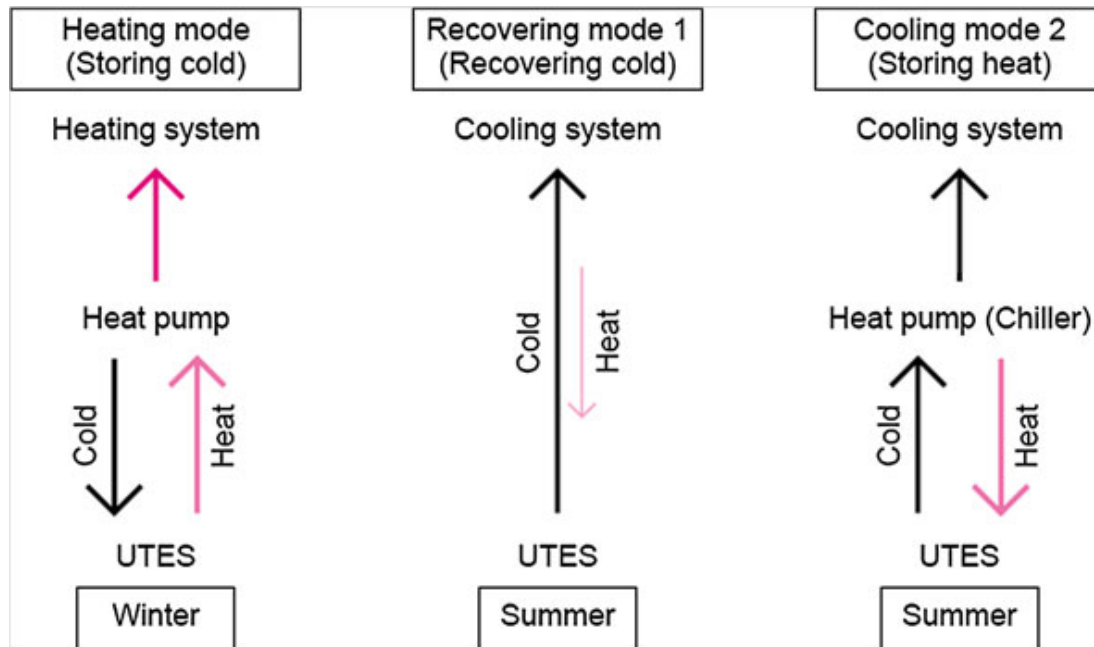


Fig. 7. Operational modes of cold storage UTES with heat pumps (Sanner and Nordell, 1998).

Charging sources of such kind of underground energy storage includes but is not limited to surface water, solar collectors, pipes below paved surface, hot air in glassed space, low-temperature waste heat or some other heat sources (Lee, 2013).

1.3.1.2 Storage and extraction technology

The underground storage system can also be classified into open system and closed system, into which shallow geothermal energy is classified generally.

In open systems, aquifers in the underground (and the solid earth) will be used as a heat source (or heat sink). Usually, there are two groundwater wells used to extract and inject water from (or into) the ground. Water is allowed to flow freely in the underground so to exchange heat with the groundwater (or solid earth). A schematic of the open system is shown in Fig. 8 (Sanner, 2017). However, in this system the surrounding groundwater is involved and hence some environmental issues can arise, which is a disadvantage.

Some requirements are to be met in order to implement the open system.

- Sufficient permeability of the ground so to allow the designed amount of groundwater flow freely.
- The chemical components of the groundwater are to be checked so to avoid problems like scaling, clogging and corrosion.

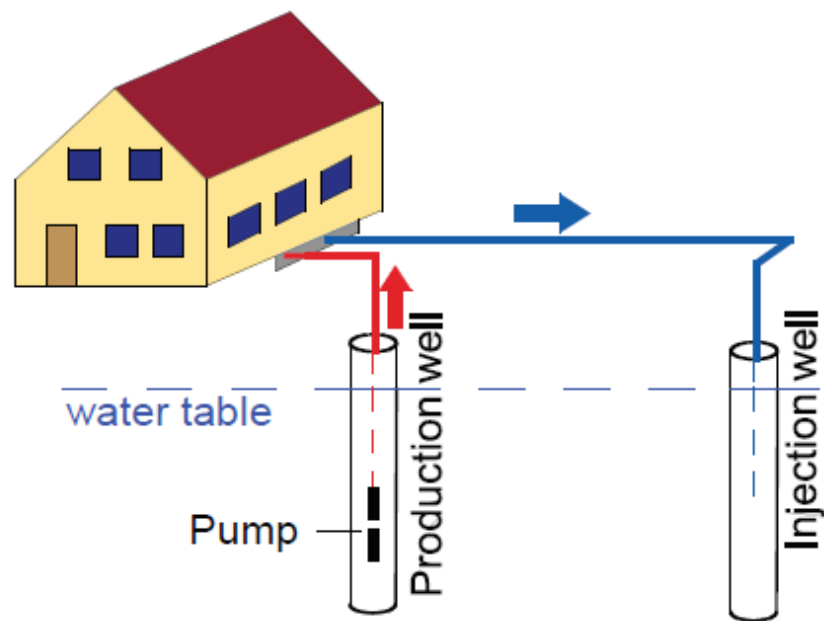


Fig. 8. Schematic of underground thermal storage open system (Sanner, 2017).

Closed system of UTES is usually vertical so to exploit the shallow geothermal energy. Also, to put it vertical is a way to save the use of ground surface considering the high price for land. The heat collector pipes are installed vertically into the ground where the heat carrier fluid will be circulated through the heat collector pipes. The heat collector pipes should be impermeable and the heat carrier fluid should be pumpable. Surrounding groundwater helps to exchange heat between the heat carrier fluid and the ground. In cases when multiple pipes are used, they should be connected to achieve the even distribution of flow and heat. The shape of the pipes can be U-shaped, coaxial and etc. A schematic of the closed system is shown in Fig. 9 (Sanner, 2017).

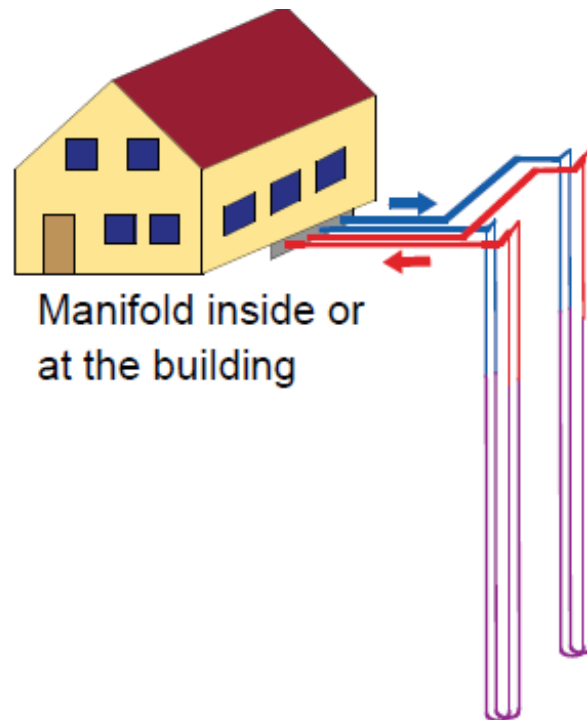


Fig. 9. Schematic of underground thermal storage closed system (Borehole heat exchangers) (Sanner, 2017).

1.3.2 Characteristics of underground storage system

Lee (2013) summarized the characteristics of underground storage system exploiting shallow geothermal energy based on the works of EU Commission SAVE Program and Nordic Energy Research (2004) in terms of efficiency, availability, application, temperature, humidity and load. This result is suitable for ground source cooling.

1.3.2.1 Efficiency

To evaluate the efficiency of a system which processes cooling or heating, the term seasonal performance factor (SPF) can be introduced. It is the ratio between the output of useful cold (or heat) and the input of external energy (e.g. electricity).

The typical SPF of a conventional cooling machine ranges between 2-4. However, the SPF of an underground storage system exploiting shallow geothermal energy can rise up to 20-50, depending on the type of UTES and the loss of energy (Lee, 2013).

1.3.2.2 Availability

In almost any cases, the conventional cooling or heating machine can be replaced by underground storage system. To implement UTES, certain geological and hydrogeological conditions are to be met. However, it is not hard to meet those conditions considering the available choices of underground storage system are sufficient to meet the different requirements.

The choice of different types of UTES is affected by the local provisions. For instance, if the specific aquifer is preserved for drinking water supply, it is usually not allowed to

be used as the heat (or cold) source for the underground storage systems. Moreover, the design quantity of produced heat (or cold) gives requirement to the size of aquifer (or ground) to be exploited as the heat (or cold) source.

1.3.2.3 Potential Application Sector

Several potential applications are summarized and listed considering different climate conditions around the world including

- air conditioning system in residential, commercial, institutional buildings and sometimes industrial buildings
- cool processing for manufacturing industries, food processing, telecom applications, IT facilities and electric generation with combustion technologies
- cooling for food preservation
- cooling and heating for greenhouse agriculture industry
- cooling for fish farming in dams

1.3.2.4 Temperature Level

The different applications give different requirements when it comes to the supply temperature. Furthermore, the different choices of the underground storage systems result in different capacity in terms of supply temperature. Generally, the supply temperature for air conditioning ranges from 6 °C to 15 °C.

1.3.2.5 Humidity

The normal requirement for air conditioning in terms of humidity is 40-60% RH. While the supply temperature of underground storage system is relatively higher, additional de-humidification is required in humid climate zone.

However, for some specific application which requires high humidity (e.g. food preservation), underground storage system is favorable for being able to provide relatively higher supply temperature.

1.3.2.6 Load Coverage

Considering the different size of the underground storage system, the ability in terms of load coverage is different. Usually, UTES of smaller size is designed for base load and cut the peak with the use of heat pump.

1.4 Advantages and Limitation

Consumption of energy for space heating and cooling is tremendous. It is estimated that 85% of the energy used for cooling can be saved if all the cooling systems will be changed into UTES system. Hence, the advantages of UTES is quite considerable. In the meanwhile, there are also limitation to the implementation of UTES as well (EU Commission SAVE Program and Nordic Energy Research, 2004).

1.4.1 Advantages

- Saving of energy

The replacement of conventional chiller with UTES system can save 70-85% of used electricity and nearly 100% of cooling demand can be covered with such system exploiting shallow geothermal energy. Furthermore, heat pump can be integrated into the system to meet both the cooling and heating demand with a even higher efficiency.

- Environmental impacts

With the saving of electricity, the emission of polluted gases (CO₂, SO_x and NO_x) will reduce as well. This will help to ease the greenhouse effect, improve the condition for the damaged ozone layer and some other environmental problem can be solved.

- Profitability

The payback time of the UTES system is generally favorable and the long-last life cycle makes it a profitable choice. With careful design and analysis, UTES system can have an even lower cost compared to the traditional cooling plant.

- Noise

The operation of UTES system is generally noiseless.

- Health aspects

Thanks to the benefit of a closed system, UTES will not produce water aerosols in air, and hence the risk of Legionella bacteria problems can be eliminated.

1.4.2 Limitation

Obviously, there are some limitations to exploit shallow geothermal energy using the UTES systems. Firstly, specific pre-investigations are to be expected in order to understand the feasibility to implement such kind of systems, especially when the system is more extensive. Secondly, some extra effort is expected in order to achieve the permit for the application of UTES system, especially the first time in the region. Occasionally, the restriction about groundwater resource protection and the assessment of environmental impact may even turn down the possibility to implement the systems. Furthermore, some operational problems may occur, though not so frequently, e.g., clogging of the well, but a proper design can avoid problems of this kind. Finally, the payback time will have to be considered. If some other sources of energy are needed to cover the peak load, the payback time is generally longer (Lee, 2013).

Chapter 2

Energy geostructures and tunnels

2.1 Definition and principle of energy geostructures

To better exploit the shallow geothermal energy, a variety of geothermal energy systems are invented, which can be divided into two groups: open-loop shallow geothermal energy systems and closed-loop shallow geothermal energy systems. Energy geostructures pertain to the latter. The function of energy geostructures is realized by the contact between the surface of the structure and the ground. Structures of this type possess the dual role of structural support and temperature regulation. The mechanism is to embed a loop of pipes, which are filled with heat carrier fluid, into the concrete members of the structures. By circulating the heat carrier fluid with a circulation pump, heat (or cold) can be transferred between ground and buildings to which such circuits are connected.

2.2 Classifications of geostructures by realization technology

Geostructures can be classified into different groups according to the technologies used to realize such structures, which includes but are not limited to

- Geostructures of deep foundation piles
- Geostructures of diaphragm wall
- Geostructures of anchors
- Geostructures of tunnel linings

2.3 Advantages of energy tunnels

Compared to the other geostructures, the inherent extensive configuration of tunnels involves incredible amount of contact surface between ground, hence a larger amount of potential exploitable heat consequently. Moreover, the internal air of a tunnel can be a heat source in some conditions (Barla et al., 2019). A schematic representation of a segment of energy tunnel is shown in **Fig. 10** (Barla and Perino, 2014; Barla et al.,

2016).

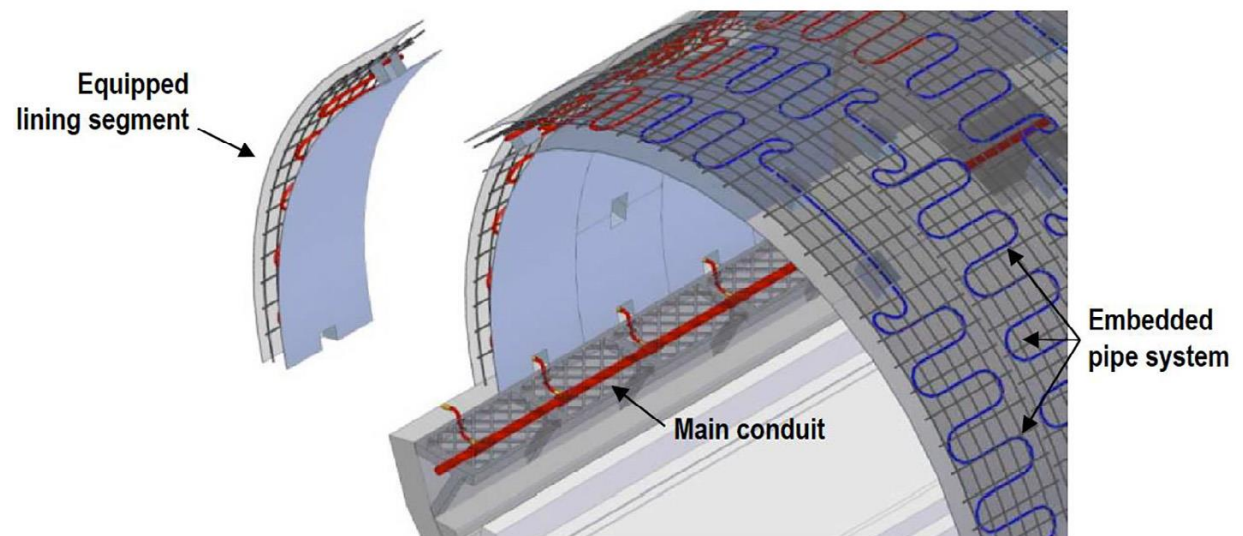


Fig. 10. Schematic representation of a tunnel segmental lining equipped as ground heat exchanger (Barla and Perino, 2014; Barla et al., 2016).

2.4 Classifications of energy tunnels

Tunnels are not identical in terms of thermal conditions, which leads to the categorization of tunnels when it comes to thermal activation. There are two groups, Hot tunnel and Cold tunnel.

Hot tunnels are characterized by a high internal temperature (approximately 30 °C in summer) due to busy traffic (e.g., Urban tunnels) and high overburden (e.g., Alpine tunnel). Diameter of such tunnels is usually smaller (approximately 7 m). High internal air of the tunnel can also heat the surrounding ground.

Cold tunnels, on the other hand, possess a lower internal temperature (approximately 15 °C throughout a year) with moderate traffic and larger diameter (10-12 m). Such type of tunnels is not likely to heat the surrounding ground (Barla et al., 2018).

2.5 Related research projects about energy tunnels

To realize the construction of energy tunnels, different approaches were introduced in different projects. Markiewicz and Adam (2009) introduced a way to realize the concept of energy tunnel with conventional tunneling methods (e.g., New Austrian Tunneling Method) by applying absorber pipes between the primary and secondary linings of the tunnel. The absorber pipes are attached to the non-woven geosynthetics offsite. Similarly, Brandl (2006) presented a pilot research project in Vienna Metro where energy tunnel was introduced for heating and cooling of the Metro stations. Apart from absorber pipes between primary and secondary linings, such pipes were placed also

within road/railway structure. The energy geotextile used in this project is shown in **Fig. 11**.

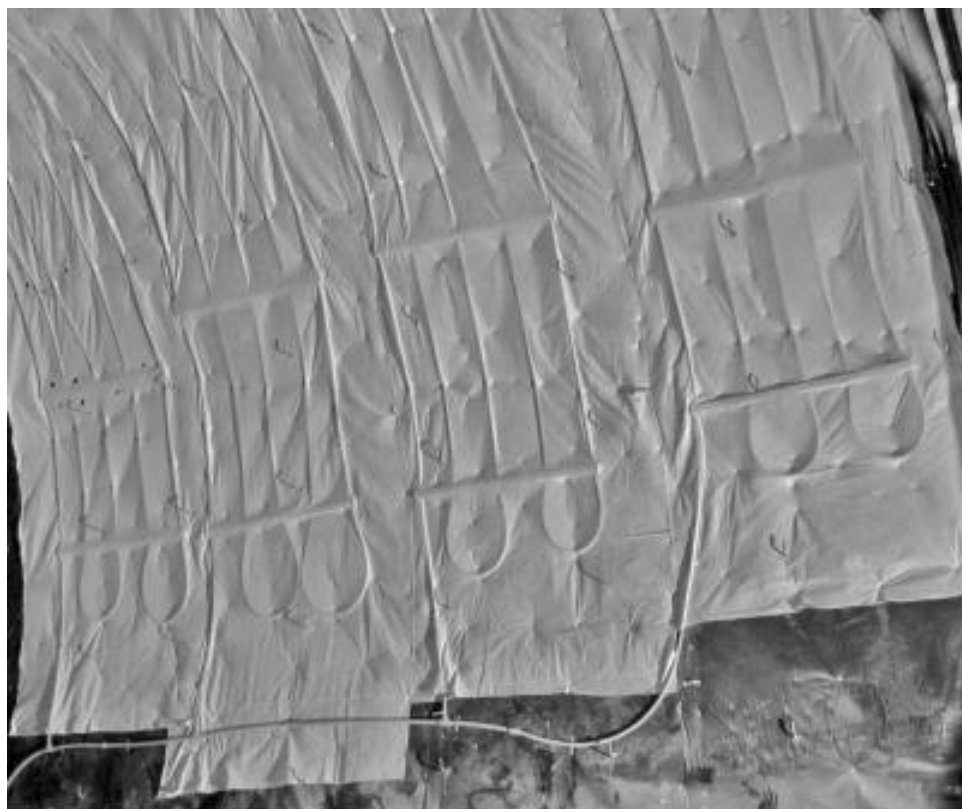


Fig. 11. Energy geotextile (geocomposite) installed in an energy tunnel between primary and secondary linings (Brandl, 2006).

Zhang et al. (2013) introduce the Tunnel lining GHE heating system, which treats the ground as a heat source, to protect the tunnel against freezing damage. The tunnel is located in Yakeshi city of Inner Mongolia Autonomous Region, China, where the annual air temperature lies below 0°C . In such a cold region, tunnel heating system is required for the sake of safety and durability of the tunnel, which is usually fueled by electricity and coal carbon. As suggested by the preliminary research, the surrounding ground of the middle part of the tunnel alignment is characterized by a higher constant temperature, which was then turned into the heat source to warm the tunnel entrance to replace the use of electricity or coal.

This heating system consists of primary circuit, secondary circuit and a heat pump. The primary circuit is placed between the primary and secondary lining at the middle part of tunnel in order to extract heat. The secondary circuit is situated between the secondary lining and the insulation layer in the tunnel entrance in order to warm the tunnel system. The heat carrier fluid with anti-freezing will be circulated within this closed loop. The schematic of this tunnel heating system is shown in **Fig. 12**.

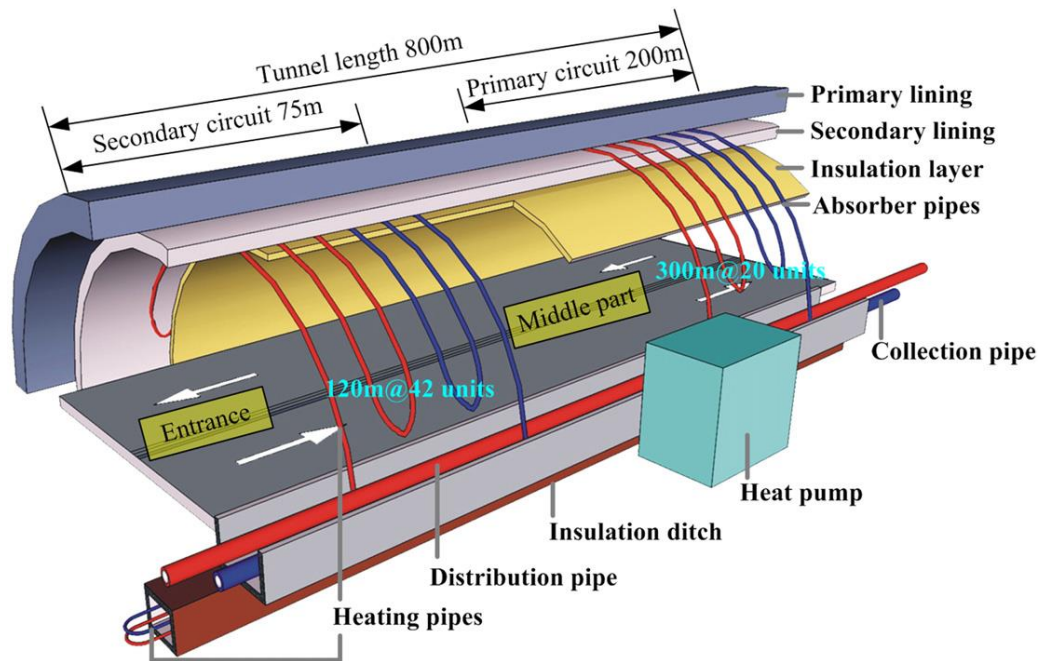


Fig. 12. Schematic view of the tunnel heating system using geothermal energy (Zhang et al., 2013).

2.6 A prototype of energy tunnel with Enertun configuration

As TBM is widely used today, to combine the concept of energy tunnel and TBM is promising. Differing from conventional tunneling method, the absorber pipe will be installed into the precast segmental lining during its manufacture, which makes it possible to optimize the configuration of the absorber pipes to reach a higher thermal performance. Meanwhile, in such way, the construction process will not be delayed due to the extra time invested to install the absorber pipes onsite.

An innovative heat-transfer pipe configuration called Enertun was proposed by Barla et al. (2018). The absorber pipes will be installed during the manufacturing of the precast segmental lining with three different types of configuration for various applications, namely ground configuration, air configuration and ground & air configuration, as shown in **Fig. 13**. With the Enertun configuration, the hydraulic head loss reduces by approximately 20-30%, and the thermal performance of the tunnel lining increases at the same time.

The ground configuration is designed to exchange heat with ground and thus the absorber pipes are positioned in the extrados of the lining. Such configuration is supposed to be applied in urban area (e.g., Metro tunnel) where the demand for heat exchanging is huge.

The air configuration is designed to exchange heat with the internal air in tunnel and thus the absorber pipes are positioned in the intrados of the lining. Such configuration is supposed to be applied to tunnels with need of cooling of the internal temperature

(e.g., Alpine tunnel).

The ground & air configuration is designed to realize both of functions mentioned above, which suggests that absorber pipes will be placed both in the extrados and intrados of the tunnel lining. In this way, the heat exchange with ground and internal air can take place simultaneously or partially to meet the requirement from customers.

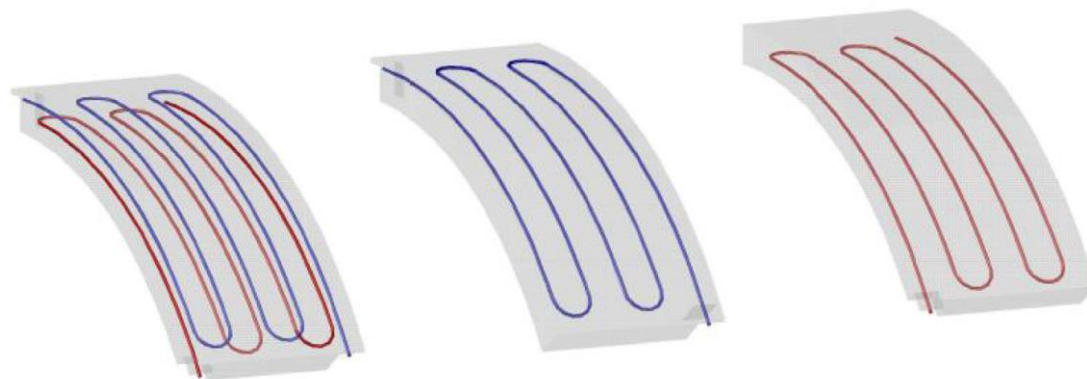


Fig. 13. Different configurations of the new energy segmental lining ENERTUN: (a) ground&air, (b) ground and (c) air (Barla & Di Donna, 2018).

A prototype of the energy tunnel Enertun, composed of two rings totally thermally activated with ground & air configuration, was realized in Turin Metro Line 1 South Extension successfully, where many different tests were run and some useful information was obtained from both the monitoring data and the numerical modelling. The total longitudinal length of this prototype reaches 2.8m with 116m/ring of pipes at extrados and 110m/ring of pipes at intrados.

In terms of the manufacturing of Enertun, as the design of absorber pipes circuit took place after that for the lining, the location of the pipe circuit should respect the functional layout of the lining design. Consequently, the pipe circuit was placed inside the bending rebars. The heat carrier fluid employed in this project is propylene glycol mixed with water allowing to work down to a temperature of -20°C . Regarding the pipes for this purpose, they are fabricated from reticulated polyethylene (Pe-Xa) and are composed of three strata with different function. Such kind of functional pipes guarantee the resistance to temperature changes, high pressure and high corrosion, which leads to the high durability of the system. Meanwhile, plenty of monitoring sensors and gauges were installed at different location in order to obtain useful in-situ data. A segment of the energy tunnel lining before casting is shown in **Fig. 14** (Barla et al., 2018).

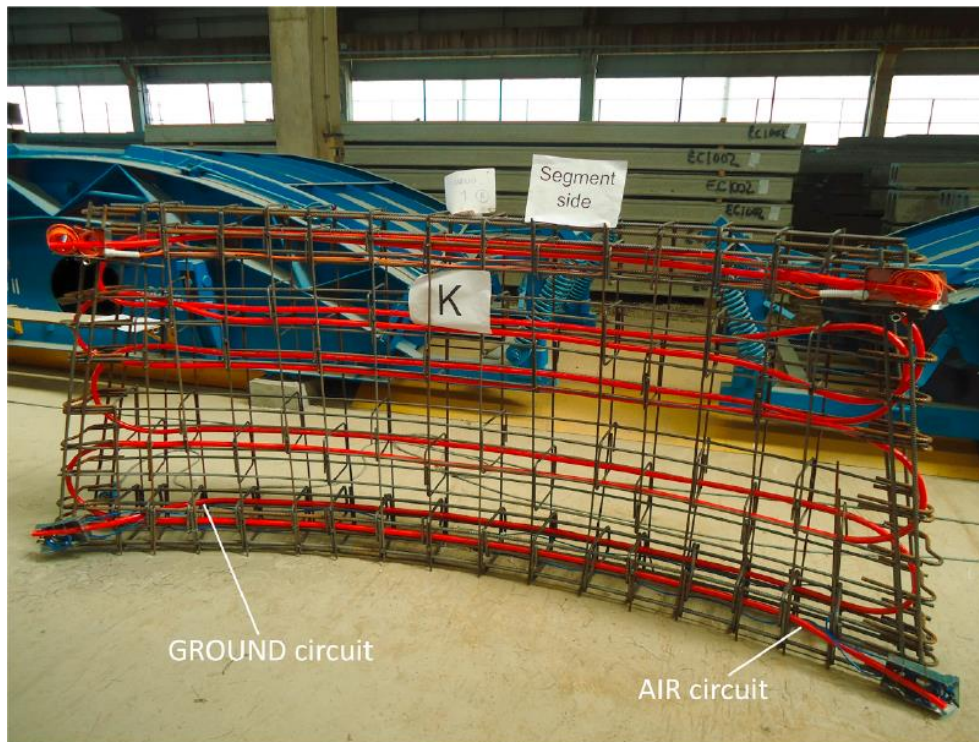


Fig. 14. Example of steel cage equipped with pipes before casting (Barla et al., 2018).

It is of significance to point out that in this prototype of Enertun, each of the ring circuits formed by one single lining ring will connect to the header pipes in parallel by introducing hydraulic valves between the header pipes and ring circuit. In this way, each ring can be run and checked individually.

The header pipes then connect a heat pump, which connects the secondary circuit represented by the potential users. The employment of the heat pump enables the adjustment of target temperature set by users.

In terms of the performance of this Enertun prototype, some tests were run successfully showing positive results. The first test with the ground configuration and heating mode was performed during winter of 2017/2018, with a target temperature of 45°C set by the heat pump. Starting from around 10°C (with fluctuation since the secondary was exposed to external air), an inlet temperature of $35\text{-}40^{\circ}\text{C}$ and an outlet temperature of $30\text{-}35^{\circ}\text{C}$ at secondary circuit were reached. Regarding the primary circuit, an inlet temperature of 2.3°C and an outlet temperature of 4.4°C were reached starting from around 14.2°C . An extracted thermal power of 51.30 W/m^2 was attained from this test of heating mode lasting for 7.82 days (Barla et al., 2019).

Some further researches and tests of both heating and cooling mode were conducted with this Enertun prototype resulting in the extracted thermal power ranging from 40.8 W/m^2 to 66.4 W/m^2 . It is observed that the extracted thermal power from cooling mode is generally higher than that of heating mode due to a higher flow rate and higher temperature difference between the ground and heat carrier fluid (Insana and Barla, 2020).

2.7 Required analysis for the application of energy tunnels

2.7.1 Calculation of exploitable heat

In order to apply the thermal activation of a tunnel, two main aspects must be fulfilled, which are a promising amount of exploitable heat (or cold) and an acceptable thermal-induced mechanical effect.

Exploitable heat is a key feature to assess the feasibility of the application of Energy tunnel. To calculate it, the following equation is given:

$$Q = M \cdot c_p \cdot (T_i - T_o) \quad (1)$$

where Q (in W) is the exploitable heat of the site, M (in kg/s) is the mass flow rate, c_p (in $J \cdot kg^{-1} \cdot ^\circ C^{-1}$) is the specific heat capacity at constant pressure of the heat carrier fluid, T_i (in $^\circ C$) is the inlet temperature of the fluid heat carrier in pipes and T_o (in $^\circ C$) is the outlet temperature of the heat carrier fluid in pipes.

If a real-scale in-situ test of prototype energy tunnel at the site under consideration can be carried out, the exploitable heat can be obtained easily knowing each term in the equation above. It can be the most straight-forward way to obtain this information of the site. However, the necessity to run such a real-scale test should be justified since in some cases the budget may not allow this test to be run. Generally, due to the large length of tunnel project, real-scale test is hard to be performed and hence numerical simulation is a better idea to obtain the exploitable heat.

2.7.2 Thermo-hydraulic (TH) coupled analysis

Alternatively, thermo-hydraulic (TH) coupled analysis can reach the identical goal in a numerical way, but the model should be validated with in-situ data from experimental campaigns otherwise the output may be affected by some degrees of uncertainty. By reproducing the model using finite element software, this problem can be solved numerically. An example of TH analysis solved by FEM software is shown in **Fig. 15** (Insana and Barla, 2020). Such a problem is governed by mass conservation, energy conservation and Darcy's Law in Eulerian coordinate system for a saturated medium composed of a solid and a liquid (water) phase (Di Donna et al., 2016).

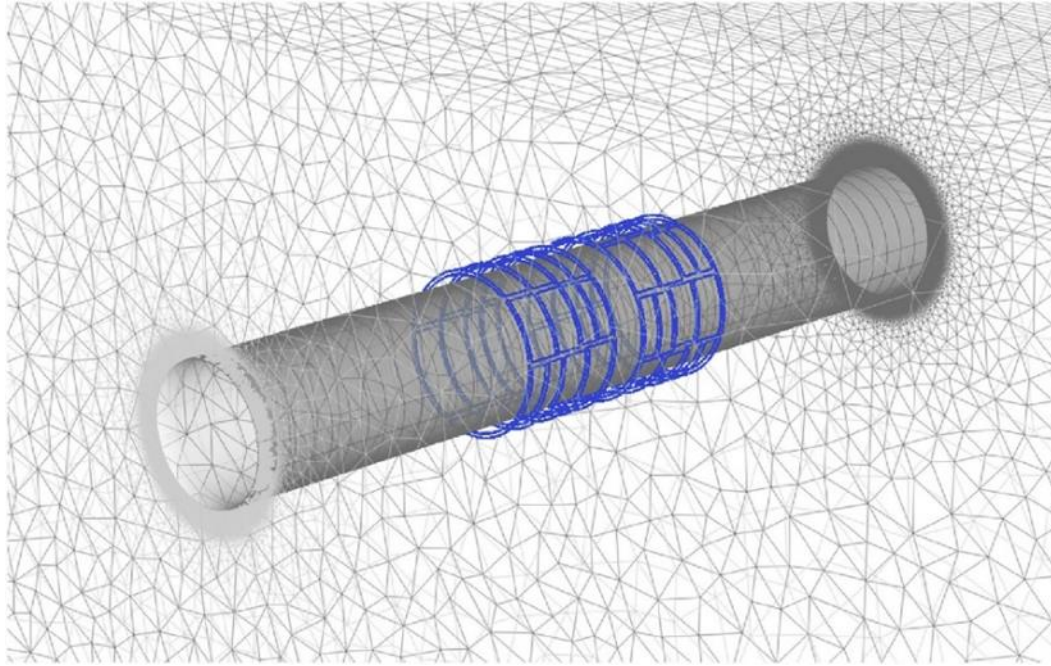


Fig. 15. 3D view of the pipes circuit (Insana and Barla, 2020).

The following equations are to be considered for the TH analysis.

- Mass conservation:

$$S \cdot \frac{\partial p}{\partial t} + \nabla \cdot v_{f,i} = 0 \quad (2)$$

$$v_{f,i} = n v_{w,i} \quad (3)$$

where $\nabla \cdot$ denotes divergence operator, $S = n \cdot \gamma_w + (1 - n) \cdot \gamma_s$ is the specific storage coefficient, n is the porosity, γ_w and γ_s are the compressibility of fluid and solid phase, respectively, p is the pressure and $v_{f,i}$ is the Darcy's fluid velocity vector, $v_{w,i}$ is the vector of water velocity with respect to the solid skeleton.

- Darcy's law:

$$v_{f,i} = -K_{ij} \nabla h_w \quad (4)$$

Where ∇ denotes gradient operator, K_{ij} is hydraulic conductivity tensor and h_w is the hydraulic head vector defined as:

$$h_w = \frac{p}{\rho_w g_i} + y \quad (5)$$

where ρ_w is the fluid phase density, g_i is the gravity vector and y is the elevation (vertical coordinate).

- Energy conservation (Consider both conduction (transient) and convection):

$$[n \rho_w c_w + (1 - n) \rho_s c_s] \frac{\partial T}{\partial t} + n \rho_w c_w v_{w,i} \nabla T - \lambda_{ij} \nabla^2 T = 0 \quad (6)$$

Where the first term on left hand side represent the heat storage, the second term represents the convection and the third for conduction. ∇ denotes gradient operator, c_w and c_s are heat capacity of fluid and solid phase, respectively, T is the temperature and λ_{ij} is the term that includes heat conductivity and dispersion.

$$\lambda_{ij} = [n\lambda_w + (1 - n)\lambda_s]\delta_{ij} + \rho_w c_w \left[\alpha_T \sqrt{v_{w,i} v_{w,j}} \delta_{ij} + (\alpha_L - \alpha_T) \frac{v_{w,i} v_{w,j}}{\sqrt{v_{w,i} v_{w,j}}} \right] \quad (7)$$

Where λ_w and λ_s are the thermal conductivity of fluid and solid phase, respectively, δ_{ij} is the Kronecker delta, α_L and α_T are the longitudinal and transversal thermal dispersivity, respectively.

To run this model, the characteristics of the site and different materials involved in the project should be evaluated including the parameters that regard the thermal performance (e.g. thermal conductivity, heat transfer coefficient, etc.). Following this step, certain of hydraulic and thermal boundary conditions (e.g. boundary temperature, hydraulic head at boundaries, etc.) are required to be clarified. Finally, the analysis can be initiated by imposing the velocity of heat carrier fluid inside pipes and the inlet temperature of the fluid. As a result, the outlet temperature of the heat carrier fluid will be obtained and so the exploitable heat can be calculated. It is vital to note that the calibration of parameters used in the model is necessary before the initialization of the analysis (Insana and Barla, 2020). Though less costly compared to a real-scale test, such a model requires certain tests to be performed in order to know the thermal performance of material.

Consequently, the development of a design chart regarding the exploitable heat of a site is beneficial at the preliminary phase of the project as to assess the feasibility of the application of energy tunnel at a specific site. A design chart created numerically considering the innovative pipe configuration (Enertun) inside tunnel lining was proposed by Barla and Di Donna (2018) validated with the experimental data from Franzius and Pralle (2011) and Lee et al. (2012). Groundwater flow velocity, Ground temperature and Ground thermal conductivity are taken into account in this design chart. As these three parameters are relatively easier to be acquired, the feasibility of an energy tunnel can be assessed in a more economical and faster way. Furthermore, based on the data obtained from the Enertun prototype installed in Turin Metro Line 1 South expansion, Insana and Barla (2020) proposed a new updated design chart again for heating and cooling mode, respectively. Apart from the mentioned aspects of the site, the direction of groundwater flow was also considered. Moreover, fluid inlet temperature, fluid velocity, pipe size and heat transfer coefficient were proven to be influential to the performance of the energy tunnel. The design chart is shown in **Fig. 16**.

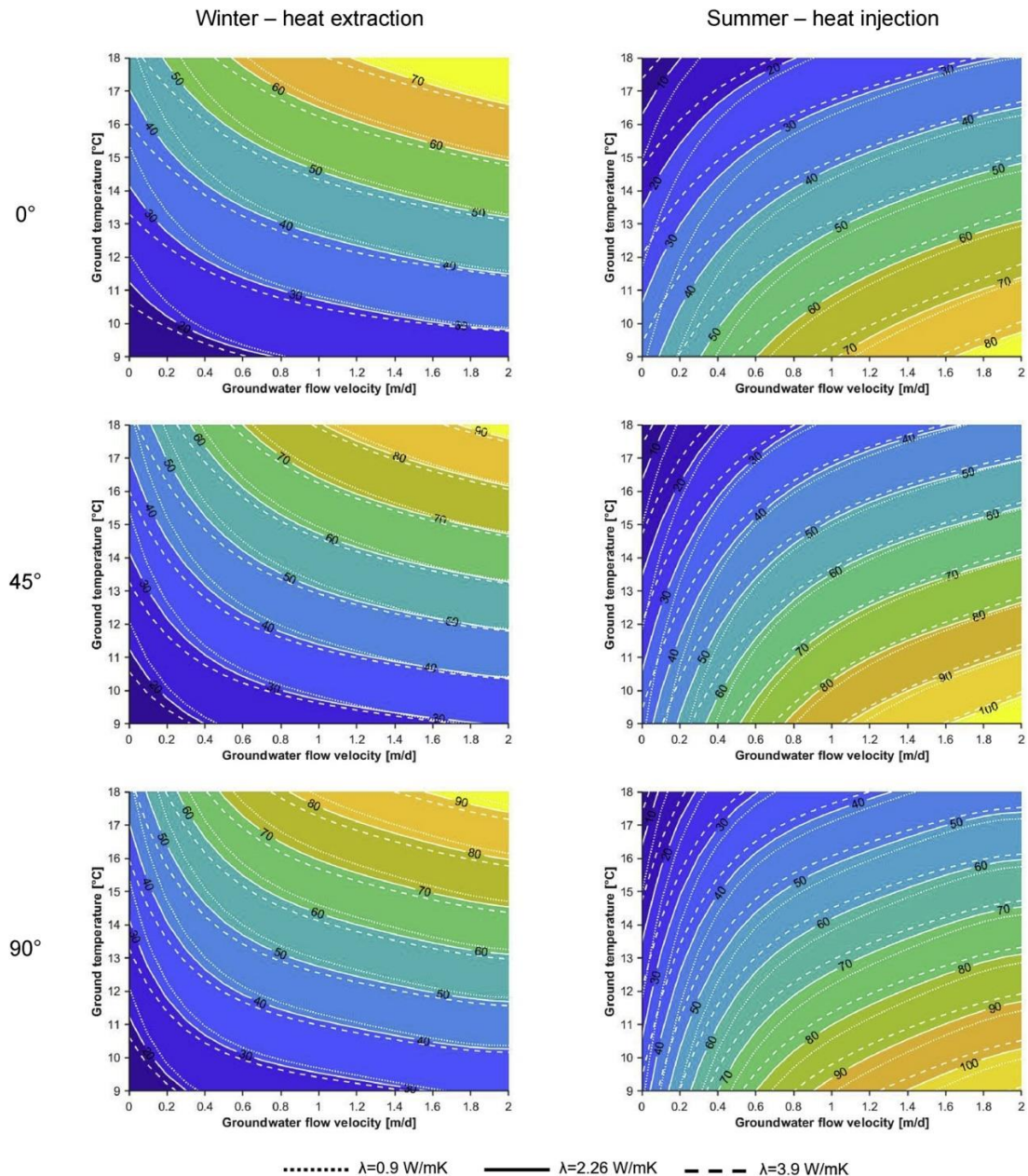


Fig. 16. Updated preliminary design charts showing geothermal potential in W/m^2 for winter and summer conditions and for different groundwater flow directions with respect to the tunnel axis (0° , 45° and 90°) (Insana and Barla, 2020).

2.7.3 Thermo-mechanical (TM) coupled analysis

In terms of structural performance, a thermo-mechanical analysis (TM) can be performed to evaluate the induced mechanical effects by temperature changes. Finite element methods or finite difference methods are to be utilized to solve the problem numerically, which requires the reproduction of the model geometry, in-situ state of stress, consideration for the construction sequence and the modified constitutive law (Barla and Di Donna, 2018). Such kind of constitutive law takes into account also the stress variation due to temperature change (Ohnishi and Kobayashi, 1995). The temperature changes adopted for this model as a boundary condition at the contour of

the pipes will be based on that coming from the TH analysis. Only thermal conduction is considered for the TM coupled analysis in this case (Barla and Di Donna, 2018). The following equations are to be considered for the TM analysis.

- Equilibrium equation:

Consider a volume of a saturated porous medium filled with a homogeneous fluid (water).

$$\nabla \cdot \sigma_{ij} + \rho g_i = 0 \quad (8)$$

where $\nabla \cdot$ denote the divergence operator, σ_{ij} is the total stress, ρ is the density of a soil-water mixing medium and g_i is the body force.

- Compatibility equation:

$$\varepsilon_{ij} = \frac{1}{2} \left(\frac{\partial u_i}{\partial x_j} + \frac{\partial u_j}{\partial x_i} \right) \quad (9)$$

where ε_{ij} is the strain and u is the deformation vector.

- Constitutive law:

Effects of temperature changes can be implemented in a constitutive law for a solid medium.

$$d\sigma_{ij} = C_{ijkl}(d\varepsilon_{kl} - d\varepsilon_{kl}^p + \beta_{kl}dT) \quad (10)$$

where $d\sigma_{ij}$ is the incremental total stress tensor, C_{ijkl} is an elastic matrix, $d\varepsilon_{kl}$ is the incremental strain tensor, $d\varepsilon_{kl}^p$ is the plastic incremental strain tensor and the term of $\beta_{kl}dT$ denotes the thermal deformation, in which β_{kl} is the thermal expansion coefficient.

By implementing the equations above, the thermal mechanical problem can be solved. It is significant to note that in this case the thermal mechanical coupling is one-way, that is thermal changes give rise to mechanical response. Nonetheless, such mechanical response does not result in temperature changes no more, which is generally negligible. An example of FDM model is shown in **Fig.17** (Barla and Di Donna, 2018).

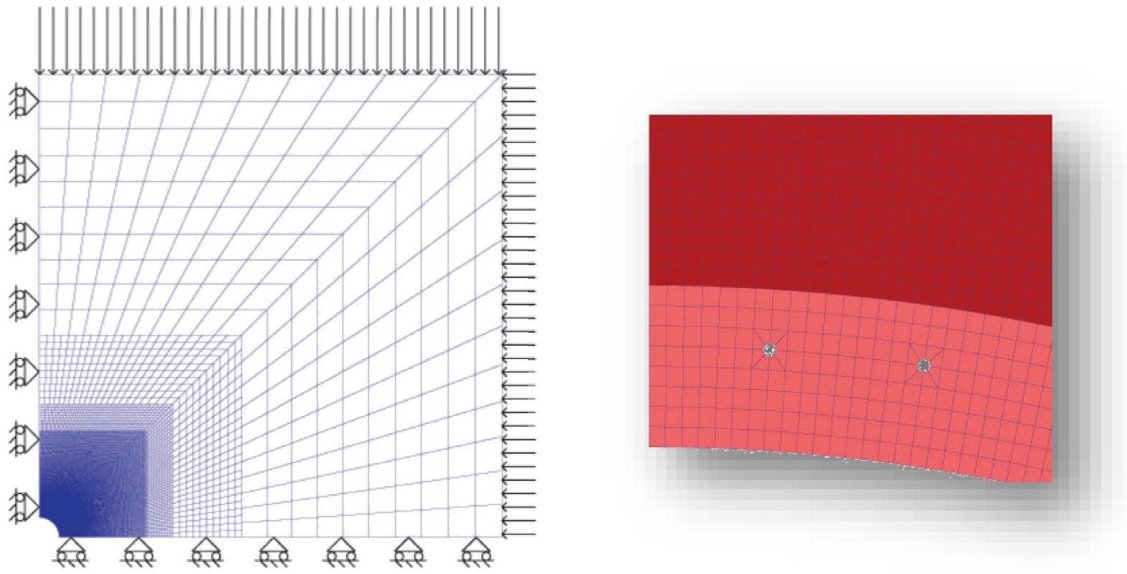


Fig. 17. Example of a FDM mesh for thermo mechanical analyses of the tunnel lining (Barla and Di Donna, 2018).

Moreover, this aspect regarding the thermo-mechanical performance in this project can be verified with the monitoring data from the real-scale energy tunnel prototype, where the thermal-induced stress and strain are comparable to those observed due to seasonal temperature fluctuation, which is totally coverable within the elastic behavior of the material of lining (Barla et al., 2019).

Chapter 3

A 3D finite-element analysis software

3.1 Introduction

In order to investigate the behavior of the tunnel equipped with EneTun considering TH coupled analysis, the software FEFLOW is used. In this chapter, a general introduction of FEFLOW and a basic workflow of how the simulation is run in FEFLOW are presented.

FEFLOW is one of the most comprehensive, well-tested programs for the simulation of flow, groundwater age, mass- and heat-transport processes in porous media. With the various functions available in FEFLOW, complex model can be built to realize the complex geometrical information needed for the model. The typical user interface of FEFLOW is shown in **Fig. 18**.

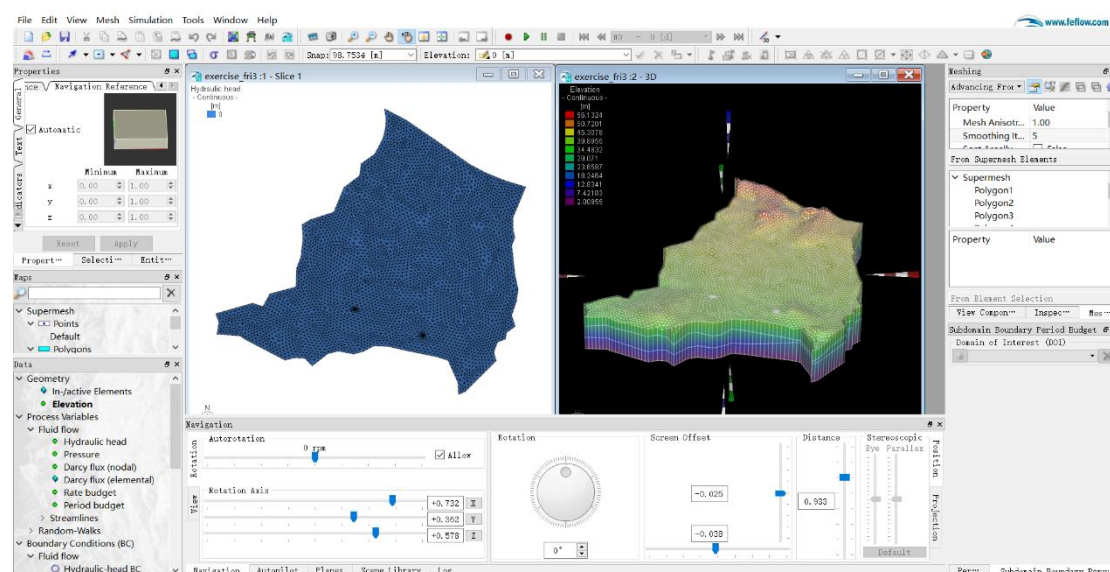


Fig. 18. User interface of FEFLOW

As it is a software based on finite element method, a finite-element mesh will be created to fill the envisioned domain with so-called Element, the corners of which is the so-called Nodes. Afterwards, by defining the model properties (e.g., Problem Class, etc.), Initial Conditions, Boundary Conditions and Material Properties based on finite-element mesh, the model with the expected behavior simulation can be performed. Various options of workflow to generate meshes of different types are shown in **Fig. 19** to meet different goals with different available input information.

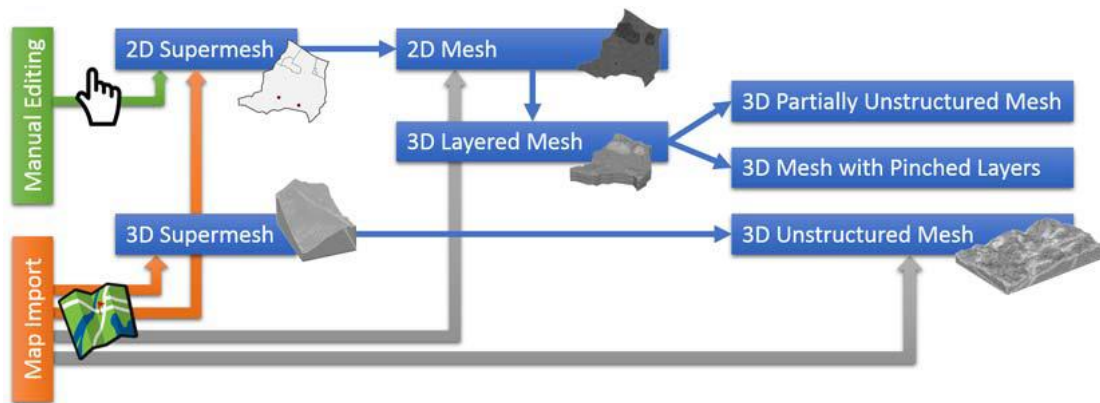


Fig. 19. Manual and map-based workflows for the generation of different mesh types

3.2 Typical process of model realization in FEFLOW

3.2.1 Supermesh design

The so called Supermesh in FEFLOW is framework for the generation of a finite-element mesh. All the needed geometrical information will be contained in Supermesh to generate finite-element mesh.

Bearing in mind that if a 3D-layered mesh is needed for the model finally, a 2D Supermesh is to be created a priori, either by manual editing or map importing.

There are several Supermesh element available:

- Supermesh Polygons

It is a subdivision of the model area into a number of separate polygons. By the application of such element, the boundary of Supermesh polygons will be respected when generating finite-element mesh, boundary condition can be applied more precisely and also parameter assignment and results evaluation later will be easier later.

- Supermesh Lines

Lines in the Supermesh are applied to represent linear structures in the finite-element mesh to be created. By the application of such element, the Supermesh lines will be respected when generating finite-element mesh, the mesh nearby will be refined, and at the meanwhile parameter assignment and results evaluation later will be easier later.

- Supermesh Points

They make sure that a finite-element node is set at exactly this location during mesh generation, they allow for local mesh refinement around the point, and they can be used for parameter assignment. Supermesh Points are to be placed at observation points or locations of wells.

Instead of editing the Supermesh elements manually, they can be imported from background maps by utilizing the function **Convert to Supermesh** or select the option **Supermesh import from maps** at the very beginning of the creation of new model. Such maps can be created via CAD software saved as .dxf files.

3.2.2 Finite-element mesh

Results of the simulation will be calculated at each Nodes then interpolated within each finite element. Thus, the denser the mesh is, the more accurate the result is. However, a denser mesh requires higher computational efforts.

For 2D application and 3D-layered meshing, a 2D finite-element mesh is to be defined, after which, if needed, the finite-element mesh can be expanded in z direction to realize the 3D application.

There are several options of mesh generation with either triangle or quad elements to discretize the domain.

- **Advancing Front**

Advancing Front is a relatively simple triangular meshing algorithm, which can be used to realize regularly shaped elements. Any lines or points in Supermesh will be neglected.

- **GridBuilder**

GridBuilder is a flexible triangulation algorithm developed by Rob McLaren at the University of Waterloo, Canada, which supports polygons, lines and points in Supermesh. In the meanwhile, refinement at points, lines or polygon edges is possible.

- **Triangle**

Triangle is a triangulation algorithm developed by Jonathan Shewchuk at UC Berkeley, USA. Complex combinations of points, lines and polygons in Supermesh will be supported with an extremely fast generation speed. Minimum finite element angle and local mesh refinement with maximum element size at lines or points are allowed to be specified.

- **Transport Mapping**

Transport Mapping is an algorithm to generate quadrilateral finite-element mesh. Lines and points in Supermesh will be neglected and polygons in Supermesh are required to be characterized by exactly four nodes.

After the generation of 2D finite-element mesh, the 3D-layered mesh can be generated via **3D layer configuration** in the **Edit** panel. To do so, the number of layers (or slices), the thickness of layers and the elevation of the upper most layer are to be defined.



Fig. 20. Different types of mesh in FEFLOW (Triangle, Advancing Front, GridBuilder, Transport Mapping, respectively, from Top Left to Bottom Right)

3.2.3 Problem setting

FEFLOW allows simulation of different applications including flow, groundwater age, mass- and heat- transport processes in either saturated, or in variably saturated media. To define different simulated process, all the available options are displayed in the **Problem Settings** dialog via the **Edit** menu.

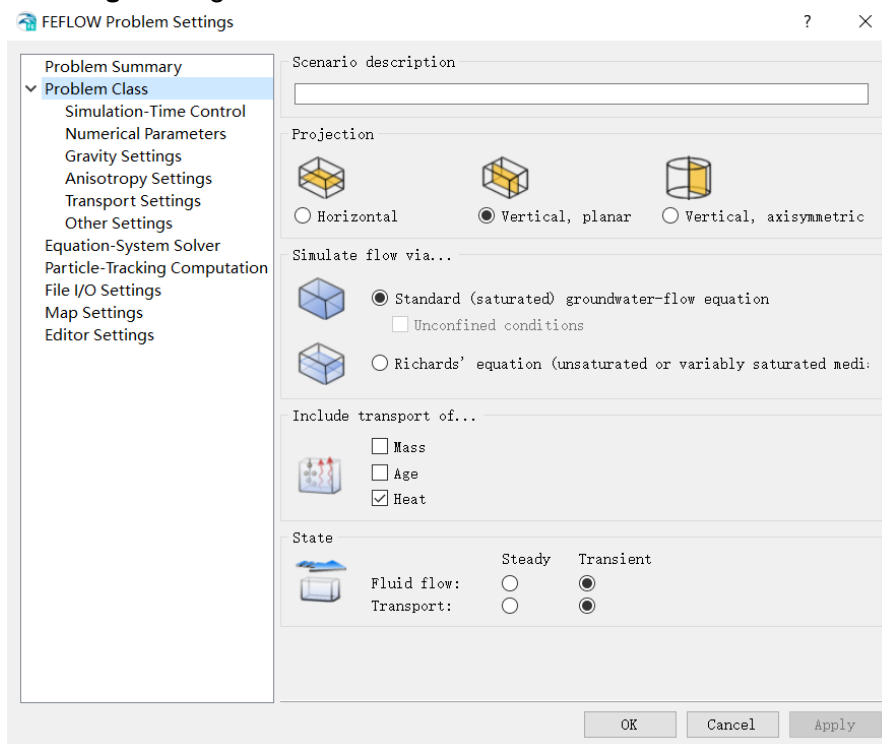


Fig. 21. Problem Settings dialog of FEFLOW

3.2.4 Selections

Selections of nodes, elements, edges and faces are of great importance, since it is the basis for parameter input, visualization and postprocessing.

It is worth pointing out that selections can be stored for repeated use with the **Store current selection** option in the invoked context menu by right-clicking in the active view or on an empty part in the **Selections** panel.

Another important tool is **Copy Selection to Slices/Layers** in the **Selection** toolbar, with which the corresponding selected nodes on the slices below the current one can also be selected by specifying the target slices.

3.2.5 Parameter Assignment

Parameters of different types are to be defined or changed during the different phase of the modeling or simulation. Different groups of input parameters are distinguished in FEFLOW shown in **Fig. 22**. Among them, Process Variables, Boundary Conditions and Material Properties are to be discussed as followed.

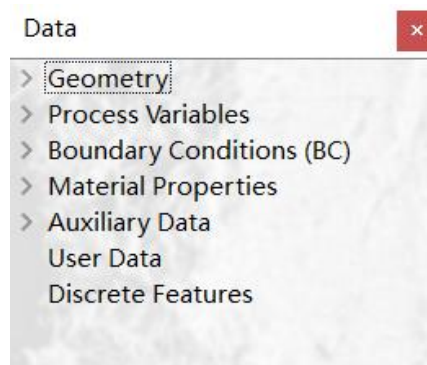


Fig. 22. Different groups of input parameters in FEFLOW

3.2.5.1 Process Variables

There are variables of three types defined in FEFLOW.

Primary variables describe the initial conditions when setting up the model, during and after the simulation these process variables reflect the then-current conditions (e.g., Hydraulic head).

Secondary variables are derived from the original primary variables. If they are input, the input is converted into the original primary variable based on current conditions (e.g., Pressure).

Third type variables are auxiliary variables supporting results evaluation and visualization, which are not allowed to be input (e.g., Darcy flux).

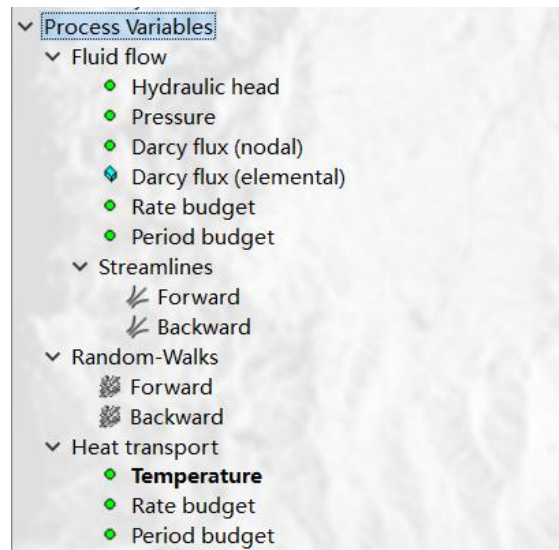


Fig. 23. Process Variables in FEFLOW

3.2.5.2 Boundary Conditions

The first type of BC is **Dirichlet-type BCs**. Such type of BCs specifies time-constant or time-varying value for the primary variable at a node, i.e. **Hydraulic head BC** for flow and **Temperature BC** for heat transport. The inflow or outflow to/from the model domain at the node can be calculated from the simulation result. This type of BCs can be defined by selecting target nodes and assigning values.

The second type of BCs is **Neumann-type BCs**, also called flux-type boundary, describing an in- or outflow of water/mass/energy at element edges (2D) or element faces (3D), including **Fluid-flux BC**, **Heat-flux BC** and so on. It is nodally defined for at least two adjacent nodes (2D) or all nodes of a vertical or horizontal element face (3D) to be considered as effective in FEFLOW.

The third type of BCs is **Cauchy-type BCs**, describing rivers, lakes, and known hydraulic heads in a distance from the model boundary. Such type of BCs includes **Fluid-transfer BC**, **Heat-transfer BC** and so on. Assignment law is similar to that of Neumann-type BCs.

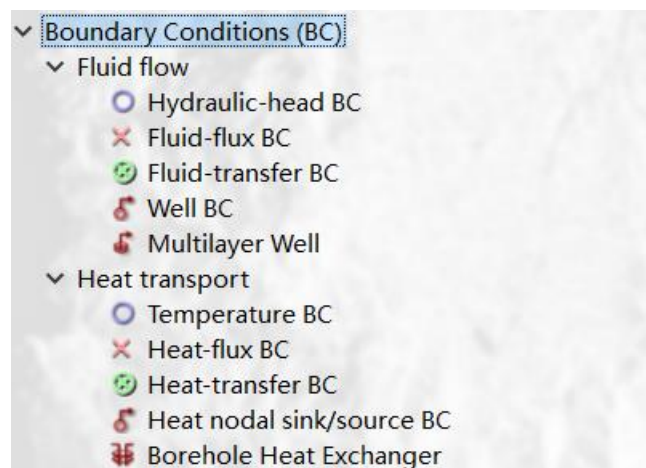


Fig. 24. Boundary Conditions in FEFLOW

3.2.5.3 Material Properties

Material properties describe the related characteristics of the porous medium for the considered flow or transport processes, which are defined elementally. The relevant material properties to be specified in FEFLOW are shown in **Fig. 25**.

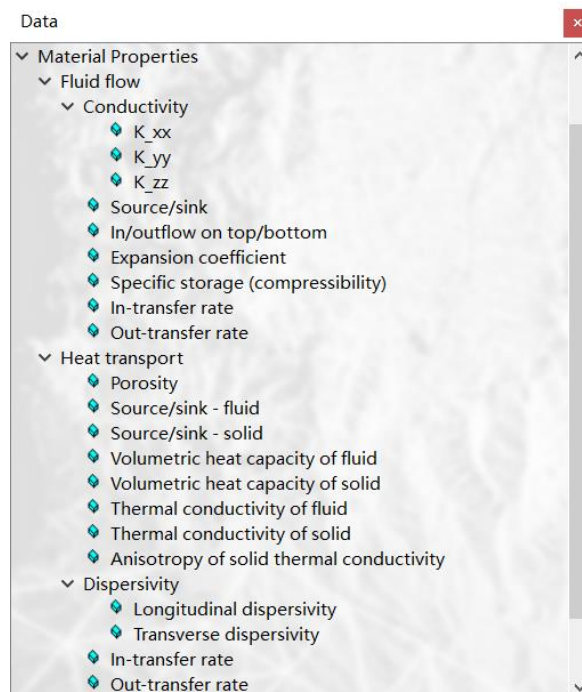


Fig. 25. Material properties in FEFLOW

3.2.5.4 Discrete Features

Discrete features are used to simulate highly conductive one- or two- dimensional features, i.e., drains, faults and pipes, which are finite elements of a lower dimension than that of the basic finite-element mesh.

To apply discrete features, geometry and flow and heat-transport properties in our case are required to be defined. Furthermore, three different flow laws are available including Darcy, Hagen-Poiseuille and Manning-Strickler.

This function is suitable for the simulation of Enertun pipes in the tunnel linings with the properties to be defined as shown in **Fig. 26**.

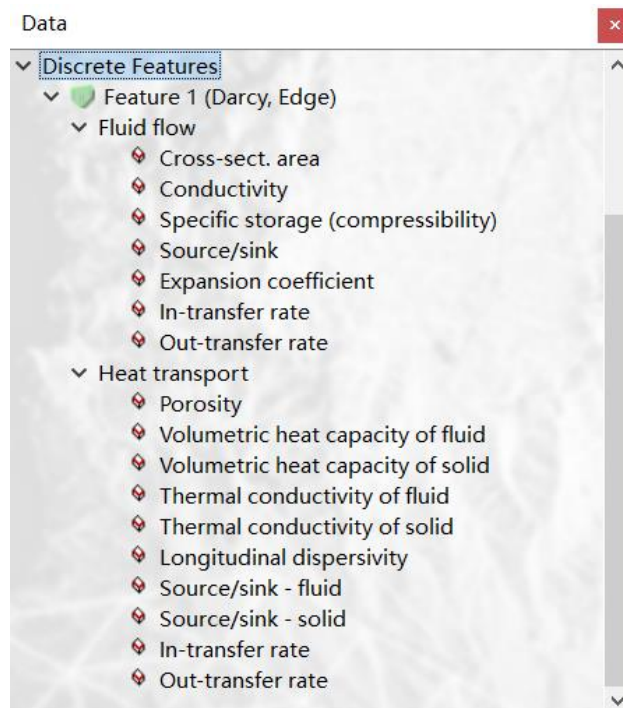


Fig. 26. Discrete Features in FEFLOW

3.2.6 Inspection

Inspection function is available for the active parameters in the current view and the attributes of maps. The properties of the target location will be shown in the view if it is constant or inspection panel if it is transient.

3.2.7 Simulation

Before the initialization of simulation, it is important to have a check on all the input parameters and other model properties in the **Problem Summary** page in the **Problem Settings** dialog.

Simulation results can be stored in formats of .dar file (reduced results) or .dac file (full simulation record). Both of them can be stored at the same time.

The reduced format stores only text output for observation points and well location at all the time steps. On the other hand, full simulation record stores all nodal values of the primary variables at all time steps by default.

Start button in the **Simulation** toolbar is to be used to start the simulation, **Pause** button to pause it, **Stop** button to exit the simulation mode. **Record** button is to be pressed before simulation to record the results.

After the simulation finishes, the model remains in paused mode to allow simulation results for postprocessing. If the simulation mode is exited via Stop button, these data are then removed from memory and so streamline/pathline calculation or budget analysis are no longer possible. Loading of the full simulation record file (.dac) is required for postprocessing in this situation.

Chapter 4

Numerical insight on the thermal behavior of the Enertun prototype

4.1 Introduction

In this chapter, the model construction of the Enertun prototype with FEFLOW is illustrated. With the measured data in-situ, the behavior of the numerical model is calibrated and validated.

4.2 Introduction of Enertun prototype

An experimental site of Enertun segmental lining was installed in the tunnel of Turin Metro Line 1 South Extension, which is currently under construction. The prototype is located about 42 m northwards from Bengasi station in the Lingotto-Bengasi Section as shown in **Fig. 27**, aimed to test the thermal behavior of the thermally activated linings (Barla et al., 2018).

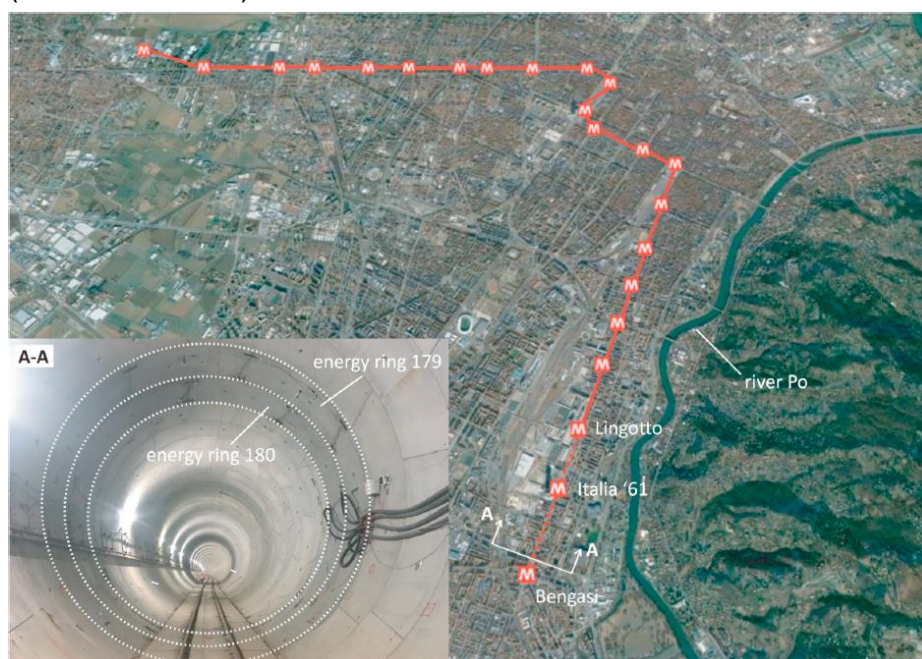


Fig. 27. Turin Metro Line 1 and the location of the Enertun prototype (Barla et al., 2018).

The tunnel can be grouped as cold tunnel with the temperature of the internal air temperature similar to that of ground surface and negligible thermal influence from the passing train operation.

The tunnel linings are characterized by an external diameter of 7.48m with a 30 cm-thick concrete lining. An 11 cm-thick layer of grout was introduced all around the tunnel lining.

The groundwater table at the site is found with a depth between 11.7 m and 12.4 m, flowing towards East to Po river with an average velocity of 1.4 to 1.5 m/day as shown in **Fig. 28** (Barla et al., 2018).

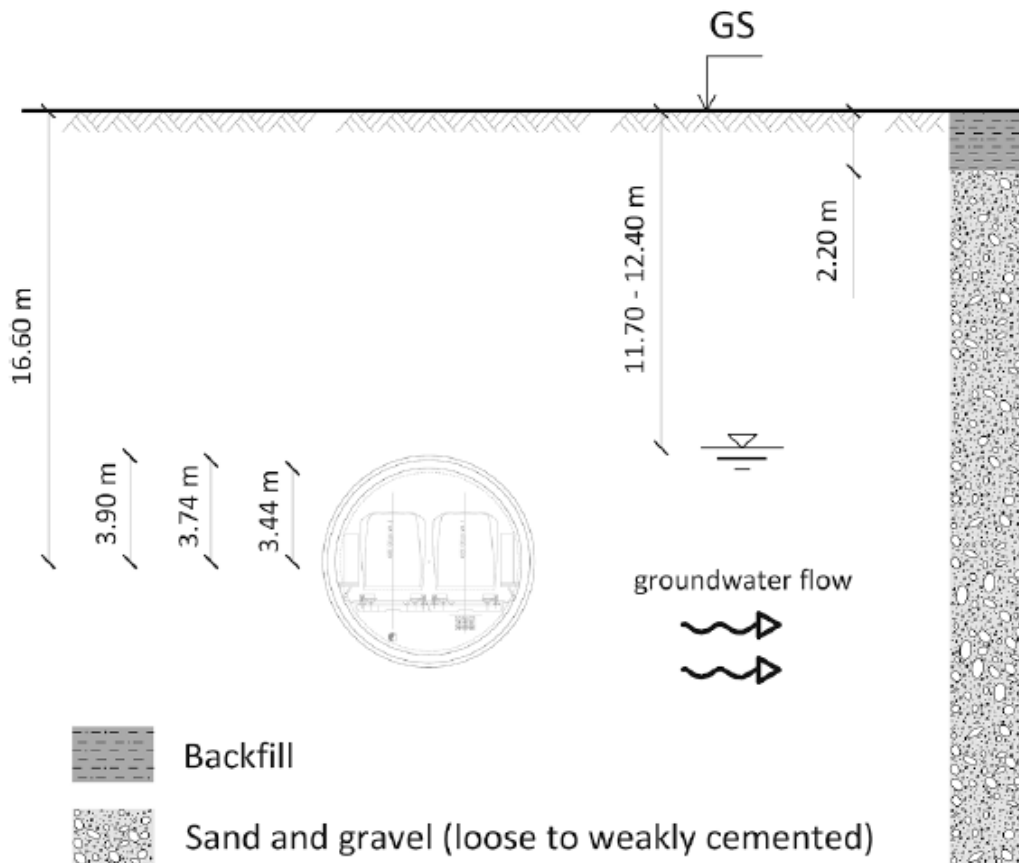


Fig. 28. Cross section of tunnel (Barla et al., 2018).

When it comes to the heat carrier pipe, the cross section is 201 mm² with an external diameter of 20 mm and the thickness of 2 mm (Insana and Barla, 2020).

Furthermore, several experimental tests were run to simulate summer/winter heating/cooling conditions with different operational parameters including volumetric flow rate and fluid velocity. The information of the tests is summarized in **Table 1**.

Table 1 List of performed tests (Insana and Barla, 2020).

| Test code | Circuit | Mode | Volumetric flow rate | Fluid velocity | Starting time | Ending time | Duration |
|-----------------------|---------|---------|----------------------|----------------|---------------------|---------------------|----------|
| | | | [m ³ /h] | [m/s] | [dd/mm/yy hh:mm] | [dd/mm/yy hh:mm] | [d] |
| 180215_G_H_T45_179180 | Ground | Heating | 1.3 | 0.9 | 15/02/2018 14:13 | 17/02/2018 09:57 | 1.82 |
| 180218_G_H_T45_179180 | Ground | Heating | 1.3 | 0.9 | 18/02/2018 13:57 | 20/02/2018 09:50 | 1.83 |
| 180222_G_H_T45_179180 | Ground | Heating | 1.3 | 0.9 | 22/02/2018 14:32 | 26/02/2018 12:50 | 3.93 |
| 180305_G_H_T45_179180 | Ground | Heating | 0.8 | 0.55 | 05/03/2018 14:05 | 07/03/2018 14:17 | 2.01 |
| 180309_G_H_T45_179180 | Ground | Heating | 1 | 0.69 | 09/03/2018 13:59 | 12/03/2018 15:47 | 3.07 |
| 180320_G_H_T45_179180 | Ground | Heating | 1.3 | 0.9 | 20/03/2018 14:00 | 28/03/2018 11:11 | 7.82 |
| 180407_G_H_T45_179180 | Ground | Heating | 1.3 | 0.9 | 07/04/2018 10:00 | 16/04/2018 18:00 | 9.33 |
| 180508_G_H_T45_179180 | Ground | Heating | 1.3 | 0.9 | 08/05/2018 10:04 | 20/05/2018 18:00 | 12.33 |
| 180727_G_C_T10_179180 | Ground | Cooling | 1.4 | 0.97 | 27/07/2018 11:29 | 30/07/2018 11:31 | 3 |
| 180801_A_H_T55_179180 | Air | Heating | 1.3 | 0.9 | 01/08/2018 10:56 | 03/08/2018 15:56 | 2.21 |
| 180804_A_H_T55_179180 | Air | Heating | 1.3 | 0.9 | 04/08/2018 20:00 | 06/08/2018 10:00 | 1.58 |
| 180807_G_C_T10_179180 | Ground | Cooling | 1.4 | 0.97 | 07/08/2018 12:22 | 09/08/2018 07:31 | 1.8 |

4.3 Realization of the geometry of Enertun Prototype

To investigate the thermal-hydro coupled behavior of the tunnel equipped with heat carrier pipe and also the response of the internal air insides tunnel, a new model was built for this specific project of Enertun prototype, the procedure of which is illustrated as followed.

The model of the Enertun prototype is realized numerically in FEFLOW with a height of 74.8 m, a width of 149.6 m and a thickness of 8.4 m corresponding to 6 rings of tunnel linings. Each of the tunnel ring is 1.4 m thick.

In order to reproduce the full geometry of the Enertun prototype including the tunnel linings, the grout around the linings and the external, a geometrical sketch is drawn in Autocad first and then imported in FEFLOW via .dxf file.

Since circle drawing is not supported in FEFLOW, the tunnel lining rings will be drawn as 60 linear segments so to be sufficiently accurate to reproduce the geometry. Since the thermal activated pipes will be placed in the linings, the linings will consist of 3 layers of 10 cm thick and plus an external layer of grout of 11 cm as shown in **Fig. 29**. However, this simplification is a bit different from the realistic prototype considering some construction details, in which the Air configuration and Ground configuration are 6 cm apart from the intrados and extrados, respectively.

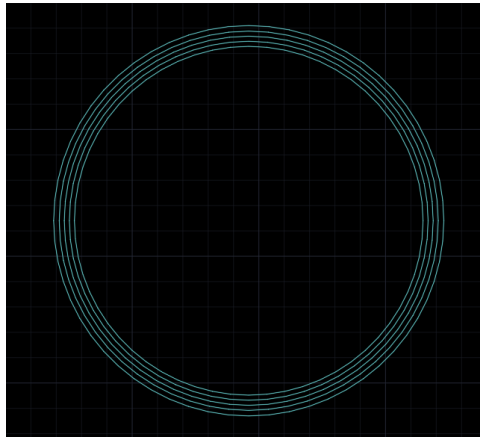


Fig. 29. Geometry of tunnel lining and grout in Autocad

In FEFLOW, the geometry created in Autocad is added as map. The lines consisting the lining, grout and the external of the model should be then converted into Supermesh lines for the sake of model realization in the phase of mesh generation. After the importation of map and conversion of lines automatically, Supermesh points at the ends of each linear segments consisting linings and grout should be inserted manually. Finally, a Supermesh polygon will be inserted following the external of model manually. The Supermesh is shown in **Fig. 30**. A detail of the tunnel lining is shown in **Fig. 31**.

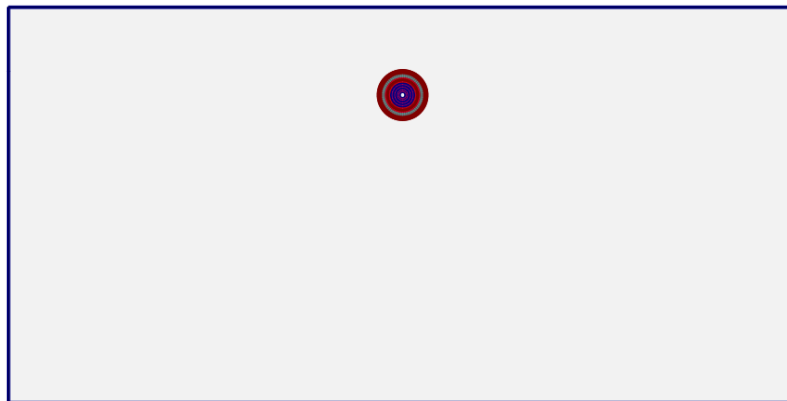


Fig. 30. Geometry Supermesh in FEFLOW

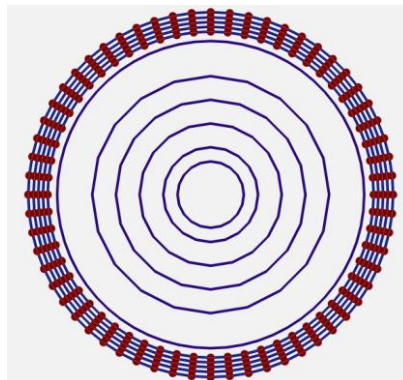


Fig. 31. Detail of the tunnel lining and internal air Supermesh in FEFLOW

With the definition of Supermesh, it is ready for the generation of a 2D finite-element mesh, which is triangle based as chosen. As seen in **Fig. 32**, the elements consisting the tunnel lining and grout fully respect the actual geometry that we created in Autocad since the introduction of Supermesh lines and points.

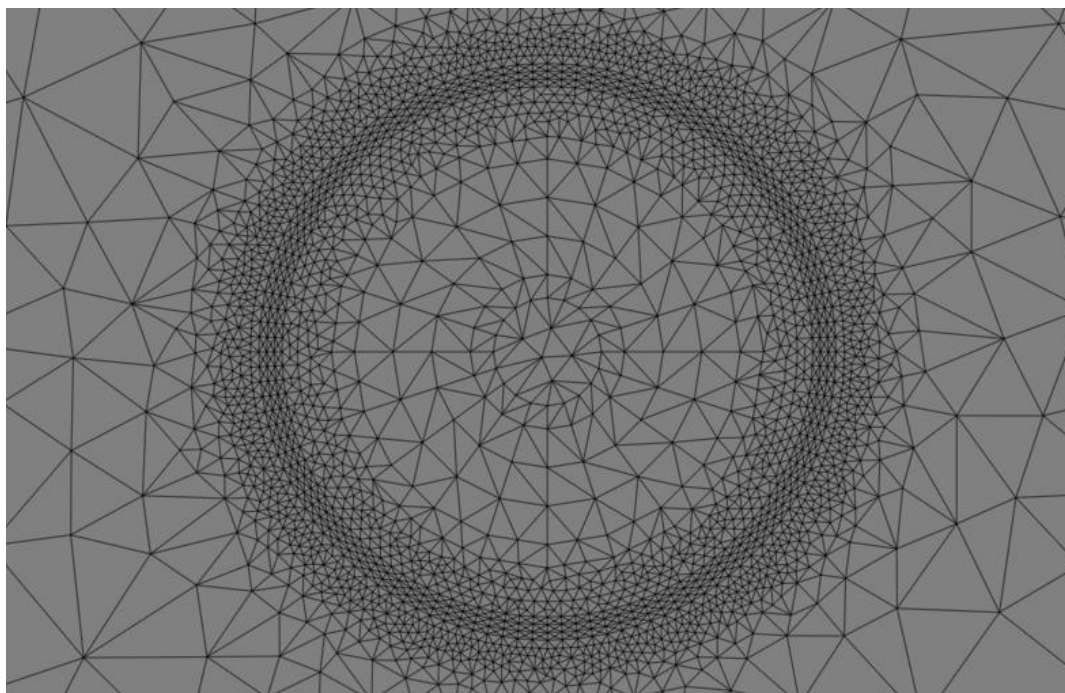


Fig. 32. 2D finite-element mesh in FEFLOW

Based on the 2D finite-element mesh, a 3D model with layered mesh consisting of triangular prisms can be defined with the 3D layer configurator. Reminding that the model is composed by 6 rings of 1.4m, the 3D model will be divided into 84 layers of 0.1 m in z axis, correspondingly 85 slices as shown in **Fig. 33**.

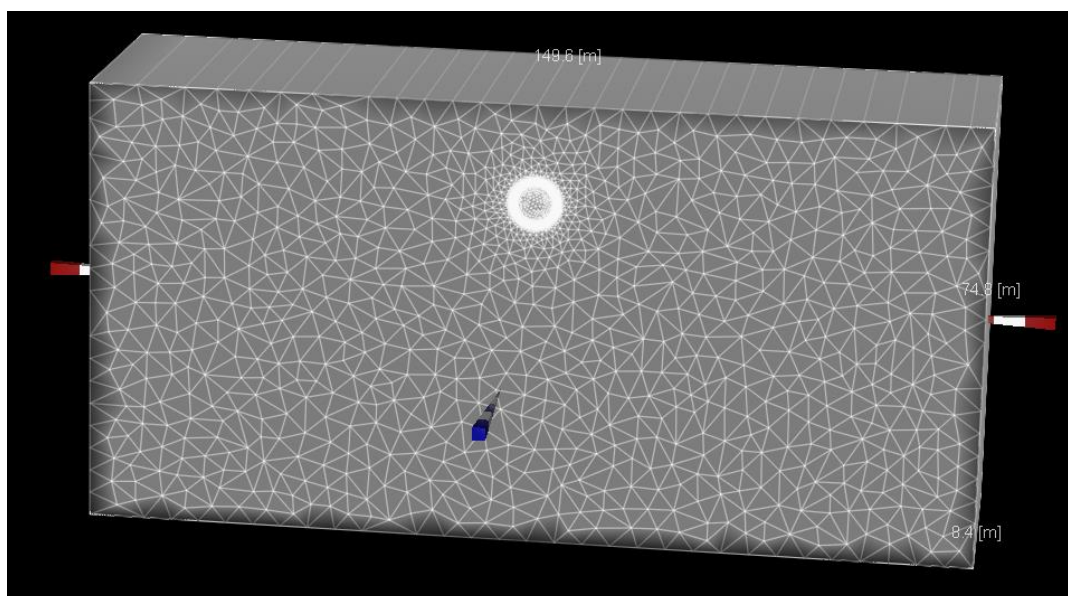


Fig. 33. Definition of 3D model in FEFLOW

By saving the 3D geometry Autocad file into .dxf file, the geometry created in Autocad can be imported into FEFLOW by using the 'add map' function. After that, we need to convert the map into Edge path so to have the corresponding edge path in selection and to avoid selecting thousands of edge path manually. Then, discrete feature will be defined with the pipe configuration so to model the heat carrier pipes, as shown in **Fig. 36** for ground configuration and **Fig. 37** for air configuration.

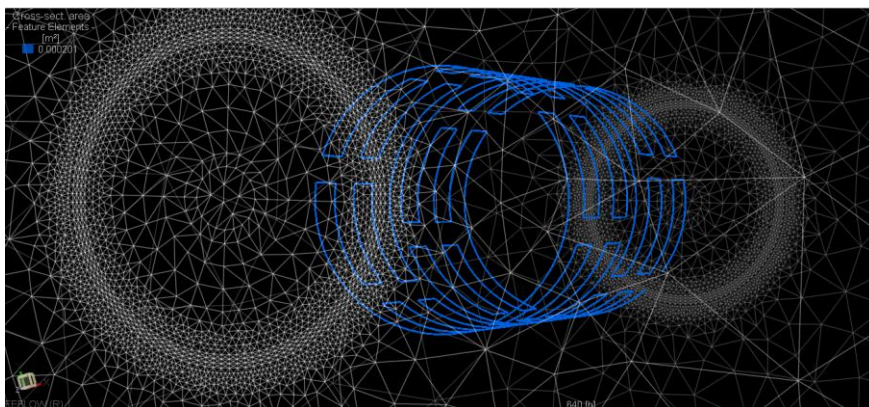


Fig. 36. Heat carrier pipes of Ground configuration in two middle lining rings modeled as discrete feature in FEFLOW

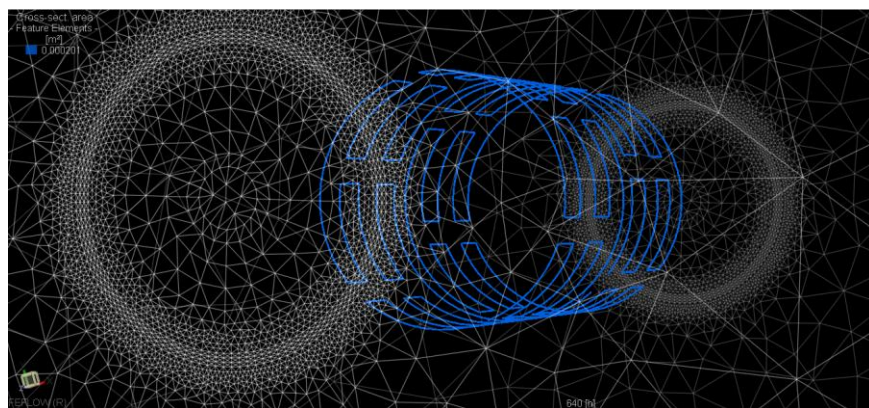


Fig. 37. Heat carrier pipes of Air configuration in two middle lining rings modeled as discrete feature in FEFLOW

4.4 Calibration and validation of the Enertun numerical model

4.4.1 Verification with the air finite elements inactive

To check whether the model is built properly, firstly, a preliminary check can be performed comparing the results of the model developed by Insana and Barla (2020), in which the internal air was replaced by Heat-transfer BC and the corresponding equivalent heat transfer coefficient. In order to run such a comparison, the finite elements representing the internal air in the new model will be temporarily deactivated. The distribution of the active and inactive elements is shown in **Fig. 38**. Furthermore, heat transfer BC is applied at the nodes of the lining intrados together with the corresponding heat transfer coefficient as suggested. At the meanwhile, the material properties to be used will be that suggested by Insana and Barla (2020) as well during the calibration phase as seen in **Table 2**.

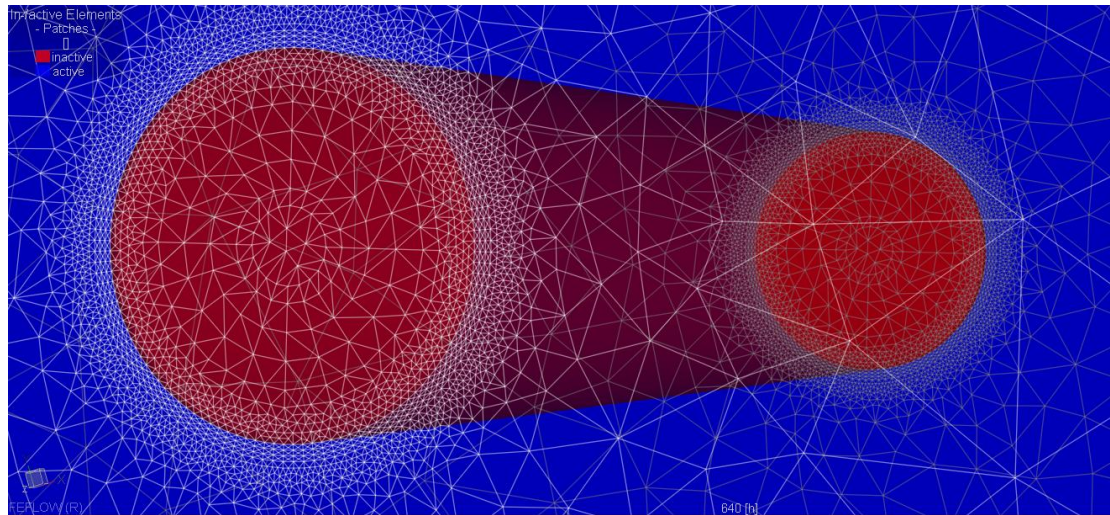


Fig. 38. Active and inactive elements

Table 2 Material properties used for model comparison (Insana and Barla, 2020)

| Material | Property | Symbol | Unit | Value |
|---------------|---|------------------|-----------------------|-----------|
| Ground | Horizontal hydraulic conductivity | K_{xx}, K_{zz} | m/s | 4.150E-03 |
| | Vertical hydraulic conductivity | K_{yy} | m/s | 2.075E-04 |
| | Specific storage | S_y | 1/m | 1.000E-04 |
| | Porosity | n | - | 0.250 |
| | Fluid-phase thermal conductivity | λ_w | W/mK | 0.650 |
| | Solid-phase thermal conductivity | λ_s | W/mK | 2.800 |
| | Fluid-phase volumetric thermal capacity | $\rho_w C_w$ | MJ/(m ³ K) | 4.200 |
| | Solid-phase volumetric thermal capacity | $\rho_s C_s$ | MJ/(m ³ K) | 2.000 |
| | Transverse aquifer thermal dispersivity | α_T | m | 0.310 |
| | Longitudinal aquifer thermal dispersivity | α_L | m | 3.100 |
| Tunnel lining | Specific storage | S_y | 1/m | 1.000E-04 |
| | Solid-phase thermal conductivity | λ_s | W/mK | 1.120 |
| | Solid-phase volumetric thermal capacity | $\rho_s C_s$ | MJ/(m ³ K) | 2.190 |
| | Horizontal hydraulic conductivity | K_{xx}, K_{zz} | m/s | 1.000E-16 |
| | Vertical hydraulic conductivity | K_{yy} | m/s | 1.000E-16 |
| | Porosity | n | - | 0.000 |
| | Transverse thermal dispersivity | α_T | m | 0.500 |
| | Longitudinal thermal dispersivity | α_L | m | 5.000 |
| Grout | Specific storage | S_y | 1/m | 1.000E-04 |
| | Solid-phase thermal conductivity | λ_s | W/mK | 0.655 |
| | Solid-phase volumetric thermal capacity | $\rho_s C_s$ | MJ/(m ³ K) | 2.190 |
| | Horizontal hydraulic conductivity | K_{xx}, K_{zz} | m/s | 1.000E-16 |
| | Vertical hydraulic conductivity | K_{yy} | m/s | 1.000E-16 |
| | Porosity | n | - | 0.000 |
| | Transverse thermal dispersivity | α_T | m | 0.500 |
| | Longitudinal thermal dispersivity | α_L | m | 5.000 |
| Pipes | Specific storage | S_y | 1/m | 1.000E-04 |
| | Fluid-phase thermal conductivity | λ_w | W/mK | 0.542 |
| | Fluid-phase volumetric thermal capacity | $\rho_w C_w$ | MJ/(m ³ K) | 4.110 |
| | Longitudinal thermal dispersivity | α_L | m | 5.000 |
| | Cross-section area | A | m ² | 2.010E-04 |
| | Hydraulic aperture | b | m | 0.800 |
| Air | Heat transfer coefficient | ϕ | W/m ² K | 5.300 |

Firstly, the hydraulic condition should be verified, where the flow velocity and the ground water table (zero pressure line) will be checked.

The hydraulic head is constant on the left and right edge of the model as suggested from the site survey, which are 62.7 m on the left and 62.1 m on the right, respectively, set as Hydraulic-head BC in FEFLOW, see **Fig. 39**.

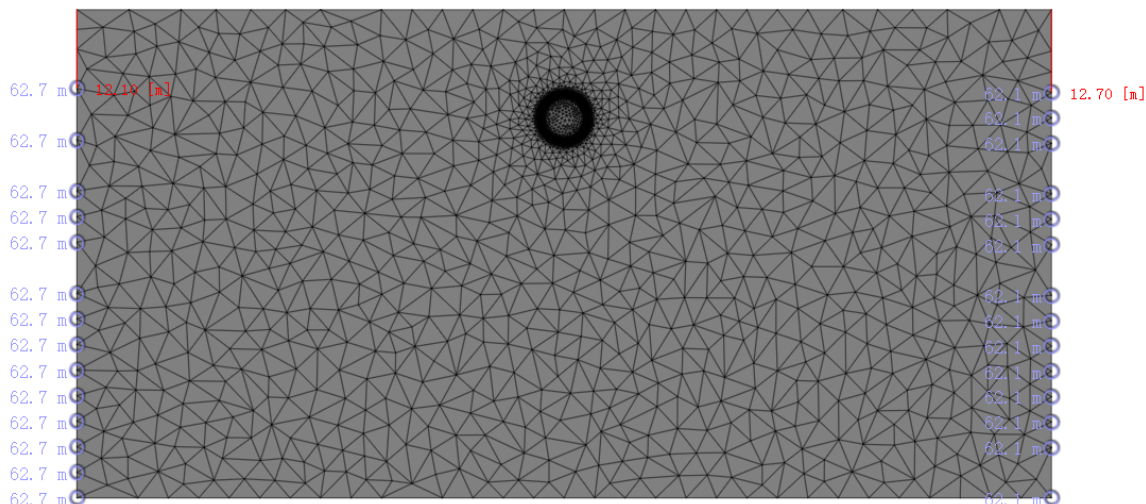


Fig. 39. Hydraulic boundary conditions

As a consequence, the velocity of the groundwater flow will be equal to approximately 1.5 m/day as calculated in the model, in coherent with the data measured in-situ. Furthermore, the groundwater table above the tunnel will equal approximately 12.4 m as shown in **Fig. 40**, which is in good agreement with the measured data as well. Negative pressure is present in the circuit pipes inside the lining.

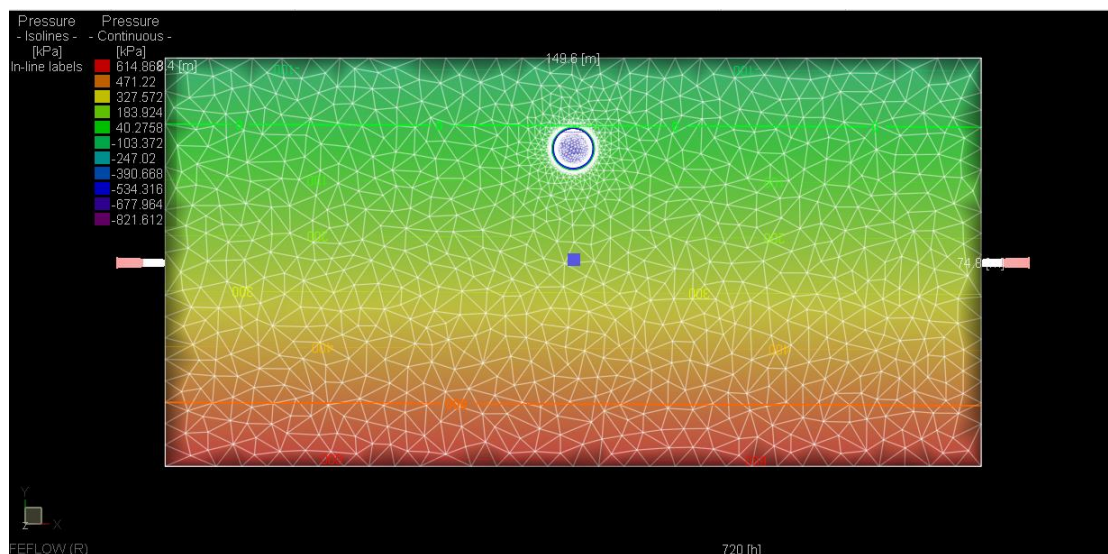


Fig. 40. Groundwater table of the modeled domain (suggested from calculated fluid pressure)

Furthermore, in order to have comparable results used to check whether the model is correctly built, the heat transfer BC of the measured time series of the internal air temperature in the tunnel is applied at the intrados of the lining as shown in **Fig. 41** and the corresponding heat transfer coefficient is applied as seen in **Table 2**.

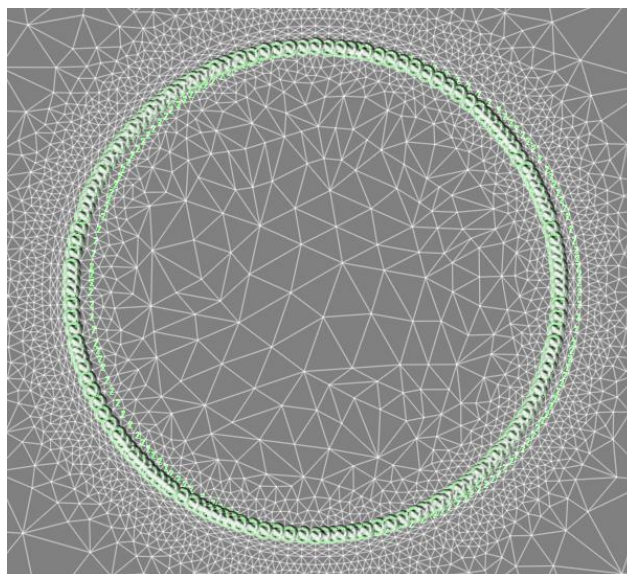


Fig. 41. Heat transfer BC at the intrados of lining

Temperature BC is applied on the top and the bottom of the model. On top of the model, the measured time series of the atmospheric temperature is applied. On the bottom, a constant temperature of 17.3 °C is applied as suggested from the measurements taken place in the experimental site. Moreover, after the preliminary simulation of 30 days, the measured time series of the inlet temperature of the heat carrier fluid is applied at the inflow point of the circuit pipe as Temperature BC as well.

To calibrate and validate the model, the calculated outlet temperature of the heat carrier fluid is the featured parameter used to compared with that measured, so to know the reliability of the new model similarly as the methodology applied by Insana and Barla (2020).

A continuous ground heating mode test, 180320_G_H_T45_179180 is to be used to perform the calibration phase comparison, in which the calculated outlet temperature of the heat carrier pipe will be compared. Before applying the monitored time series of air and tunnel temperature to the model, the data will be processed first so to reduce the size of the monitored data, which is huge originally. The rules used to process the raw data are:

- Rule 1: If three consecutive measured data are equal, only the last one is retained
- Rule 2: If three consecutive measured data are monotonically increasing or decreasing, only the first and the last ones are retained
- Rule 3: The data processing is run with an iteration step by step for each measured data in MATLAB

After the data processing, the size of temperature time series was reduced to less than one sixth of the original one with high accuracy compared to the raw data, hence the calculation time was reduced greatly. A preliminary simulation of 30 days is performed prior to the thermal activation of the lining so to obtain a representative thermo-hydraulic state before running the test simulation.

The calibration phase check yields a good result compared to the measured data and the calculated data from that obtained by Insana and Barla (2020). The difference between the calculated temperature from the new model and the measured temperature is generally less than 0.3 °C, which is within the acceptable range considering the thermistor accuracy of 0.5 °C, as seen in **Fig. 42**.

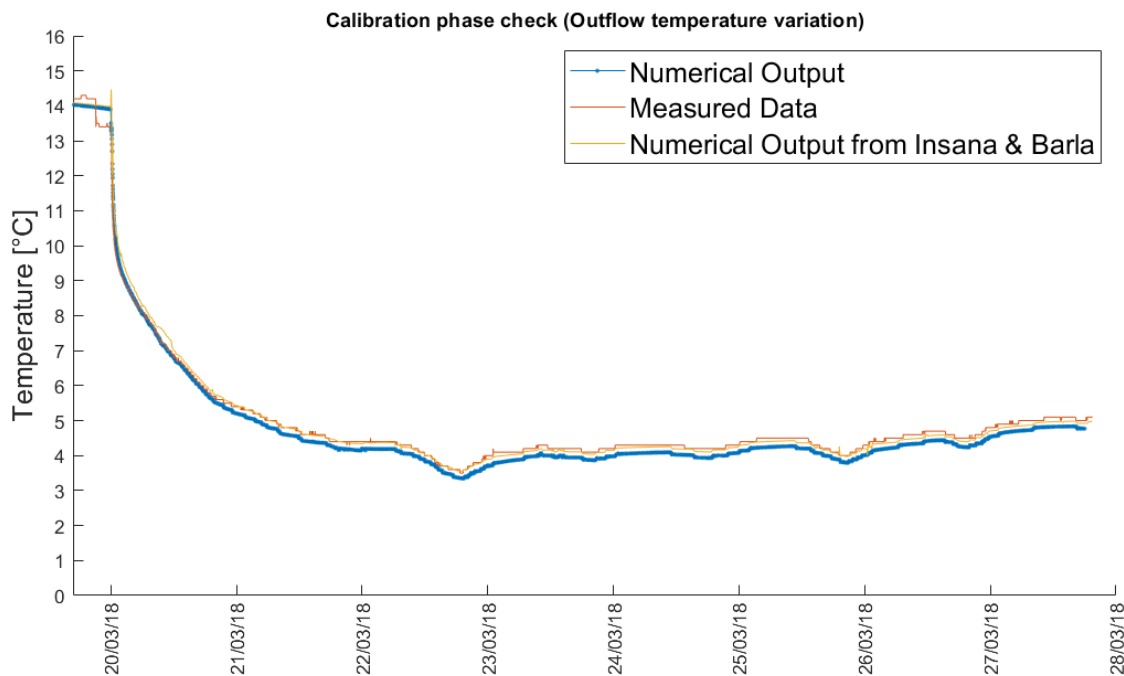


Fig. 42. Calibration phase check compared with measured data and reference data

Afterwards, four validation phase checks are performed considering different functions of thermal activation, namely two tests of Ground Heating (180305_G_H_T45_179180 and 180309_G_H_T45_179180), one test of Ground Cooling (180727_G_C_T10_179180) and one test of Air Heating (180804_A_H_T55_179180). Also, these four tests are characterized by different volumetric flow rate. The results are acceptable and stable as seen in **Fig. 43**.

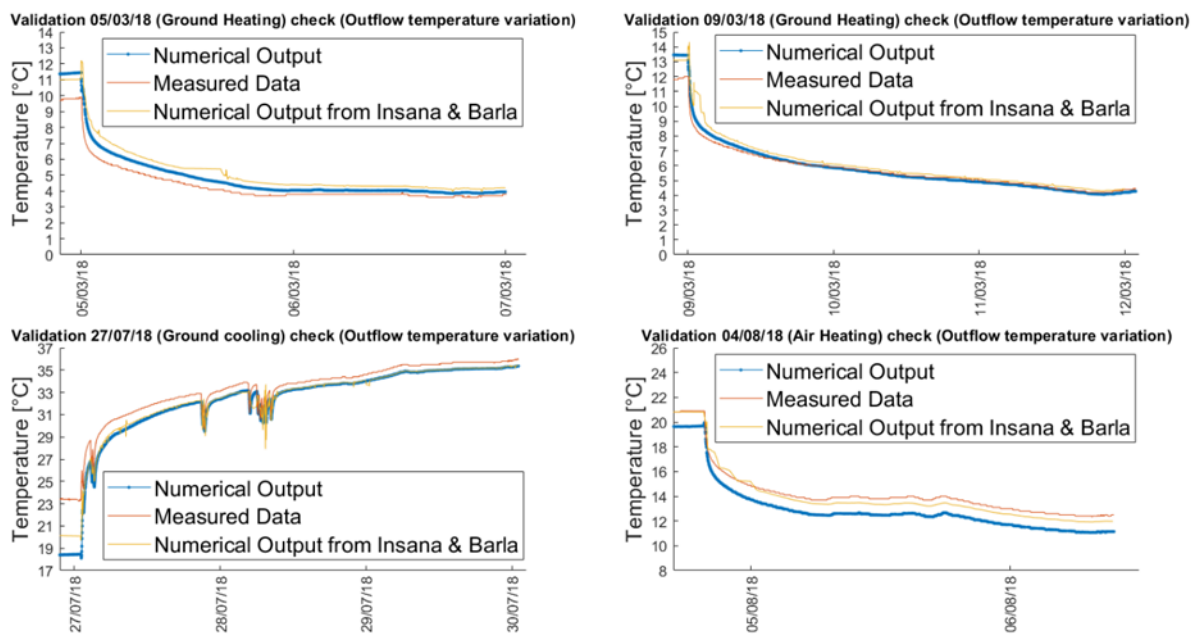


Fig. 43. Validation phase check compared with measured data and reference data

Furthermore, the measured lining temperature of the calibration phase test is compared with the calculated one. Due to the orientation of thermal pipes in the model, the corresponding position of the sensors is different from that in the prototype but the thermal pipe length that the heat carrier fluid goes through is respected, which is the main feature that influence the temperature in the corresponding lining position. The relative position of the sensor in the numerical model is shown in **Fig. 44**.

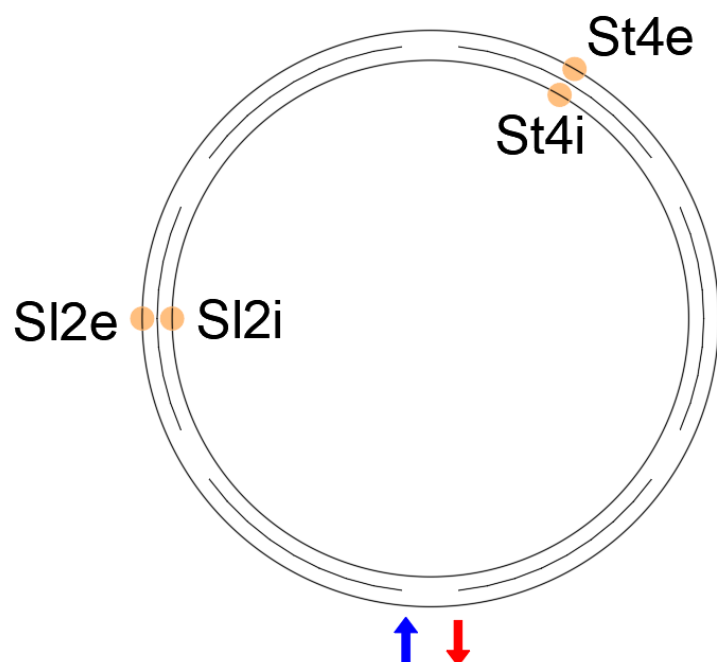


Fig. 44. Relative position of the lining temperature sensors in the numerical model

Knowing the correct positions of the sensors, the calculated lining temperature is compared with the measured lining temperature in the Enertun prototype tests and the results is shown in **Fig. 45** and **Fig. 46**. As it is observed from the plots, the performance of the numerical model is acceptable both compared with the measured data and the calculated data from Insana and Barla (2020), considering the accuracy of the sensors is 0.5 °C.

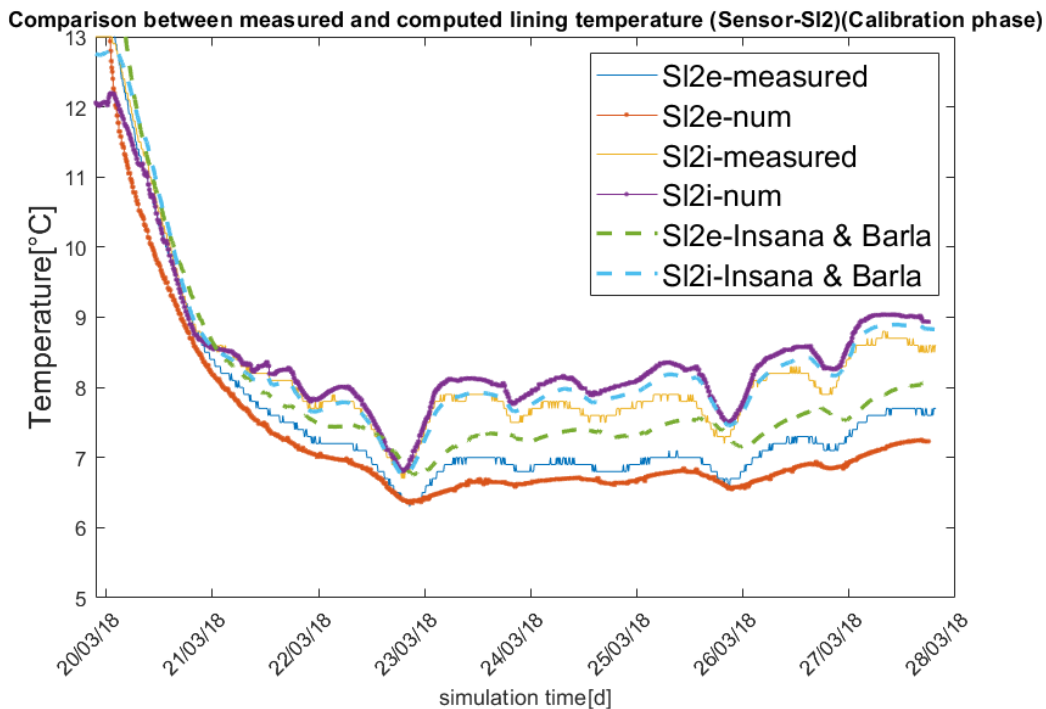


Fig. 45. Lining temperature comparison (Sensor-SI2)

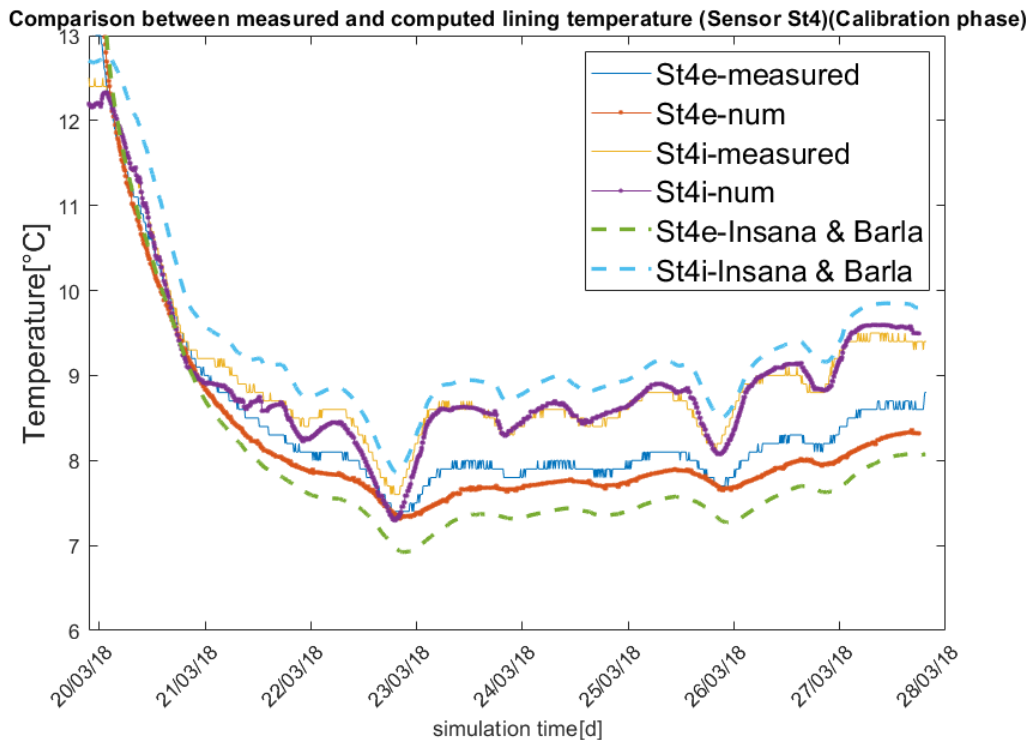


Fig. 46. Lining temperature comparison (Sensor-St4)

4.4.2 Verification with the air finite elements active

With an acceptable result from the preliminary verification of the new model, we can now activate the elements simulating internal air and proceed with the calibration and validation of the new model.

4.4.2.1 Material properties

The material properties to be assigned are based on those used in numerical realization of the same project by Insana and Barla (2020) similarly as in the preliminary verification, in which, however, the way to model the behavior of internal tunnel air is different from that in this thesis. Consequently, only the parameters for ground, tunnel linings, grout, pipes and air will be used as the first trial for calibration in Table 2, while the properties used for air is reported in **Table 3**, in which all the properties except for Fluid-phase thermal conductivity and Fluid-phase volumetric thermal capacity are suggested by Barreca (2017).

Table 3 Material properties for calibration phase of the numerical model

| Material | Property | Symbol | Unit | Value |
|-----------------------------------|---|------------------|-----------------------|-----------|
| Air | Horizontal hydraulic conductivity | K_{xx}, K_{zz} | m/s | 0.010 |
| | Vertical hydraulic conductivity | K_{yy} | m/s | 0.010 |
| | Specific storage | S_y | 1/m | 1.000E-04 |
| | Porosity | n | - | 1.000 |
| | Fluid-phase thermal conductivity | λ_w | W/mK | 2.514E-2 |
| | Fluid-phase volumetric thermal capacity | $\rho_w C_w$ | MJ/(m ³ K) | 1.212E-3 |
| | Transverse thermal dispersivity | α_T | m | 0.500 |
| Longitudinal thermal dispersivity | α_L | m | 5.000 | |

4.4.2.2 Choice of Heat Transport BC

The time series of air temperature without thermal activation will be applied on the upper boundary of the model as Temperature BC, while 17.3 °C is assigned constant as Temperature BC on the lower boundary of the model as Temperature BC.

To capture the behavior of the internal air temperature, there are two choices of Heat transport BC, namely Heat-transfer BC and Temperature BC.

- Heat-Transfer BC

A pre-defined reference temperature will be applied as the boundary condition combined with a heat transfer rate, which will be defined separately. The transfer heat will be calculated as the production of the relevant area, heat transfer rate and the difference between the reference temperature and the current temperature of the internal air.

The Heat-transfer BC is applied on the first layer of internal air in the model with the time-series of the measured internal air temperature without thermal activation of the energy tunnel. The heat transfer rate is defined separately, which is approximately 15W/m²K for air. Moreover, a fluid flux BC is applied as well (Barreca, 2017).

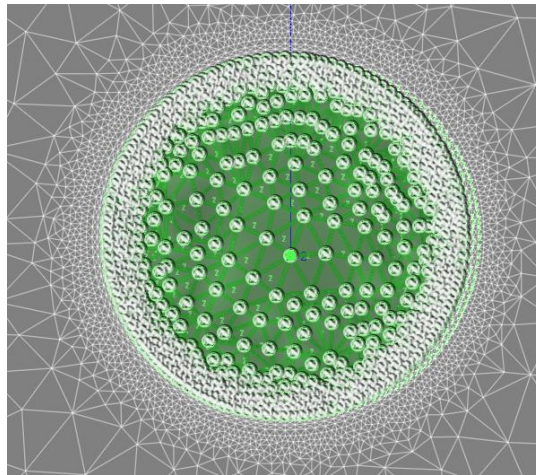


Fig. 47. Heat-transfer BC for internal air

- Temperature BC

Pre-defined temperature is applied to targeted nodes, which will result in an inflow of energy into the model when neighboring nodes have a lower temperature or an outflow from the model when there is a temperature gradient from the neighboring nodes towards the boundary condition.

The Temperature BC is applied to all the nodes of the first slice of the internal air with the time-series of the measured internal air temperature without thermal activation of energy tunnel (Barreca, 2017).

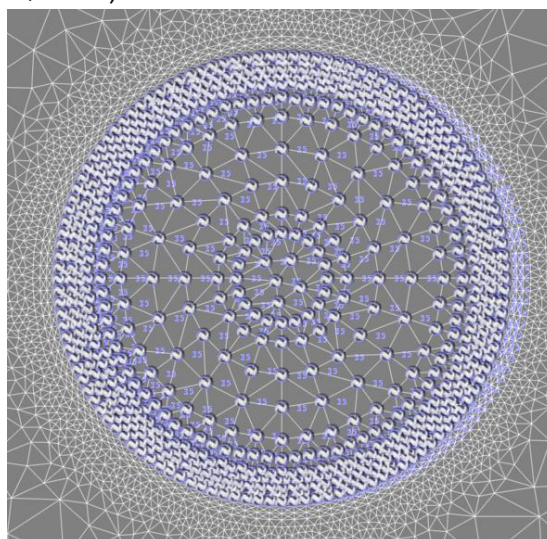


Fig. 48. Temperature BC for internal air

After these two choices of Heat transport BC were implemented, respectively, it is found that Temperature BC is a better choice to follow the measured temperature during the 30 days before the continuous ground heating mode test (180320_G_H_T45_179180) under the same fluid-flux condition as seen in **Fig. 49**. The air flow velocity used in this trial test is 0.4 m/s, which is within the normal range of internal air velocity for tunnel and provides strong convection. Hence, under such a strong convection, the temperature at the observation point A, which is located at the

middle length of the tunnel opening, should be able to follow the applied temperature at the first slice of the tunnel opening. However, Heat-transfer BC was found not able to capture the rapid spike and drop of the applied tunnel air temperature.

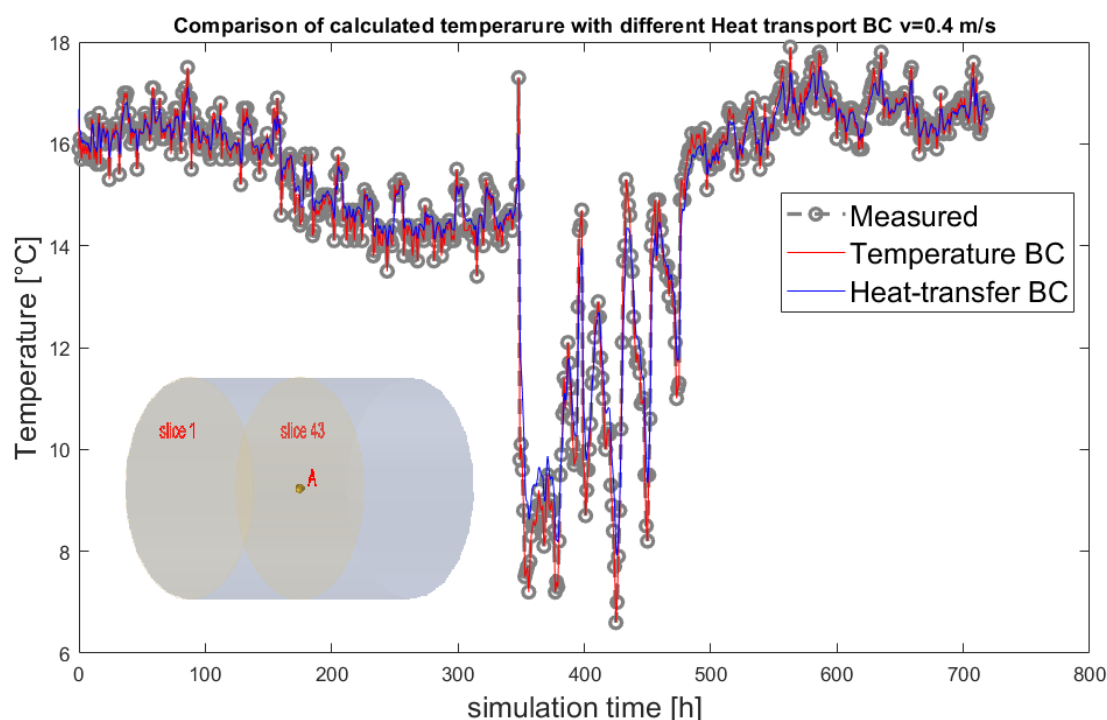


Fig. 49. Comparison between the calculated temperature of the internal air in the center of the middle length of the tunnel model under two different Heat-transport BC and the measured tunnel temperature (Observation point A at the center of tunnel in slice 43 in the model, which is the middle slice, seen as the orange point in the plot)

4.4.2.3 Internal air velocity

As it is expected, a higher flow velocity of the internal air will facilitate the heat distribution inside the tunnel. On the other hand, a lower air flow velocity will result in a more inhomogeneous distribution of the air temperature both radially and axially.

Turin metro tunnel, when being in operation, is characterized by an air flow velocity ranging from 0.1 m/s to 0.5 m/s under a forced ventilation system on the capacity of daily use. The effect of moving trains is neglected due to the low speed of running trains and the contact with the external air which impedes the development of change on air flow (Barreca, 2017). However, the Enertun prototype was realized in the Turin metro extension tunnel and those in-situ tests were run before the extension tunnel will be open for transportation. Hence, the air flow velocity can be less than 0.1 m/s due to the absence of running trains. Unfortunately, the air flow velocity was not measured in-situ. The simulation results of calibration and validation tests suggest an internal air velocity ranging from 0.005 m/s to 0.015 m/s during the Enertun prototype experimental campaign.

4.4.2.4 Numerical simulation result

After the definition of all the material properties and boundary condition, it is ready to run the calibration check of the new model with the measured data of test 180320_G_H_T45_179180. The result of the calculated outflow temperature variation is shown in **Fig. 50**. As it is observed, the simulated outflow temperature variation follows the measured data so well after the thermal activation gets stable, with a maximum difference between the calculated temperature and measured temperature of approximately 0.2 °C, which is acceptable considering the embedded thermistor accuracy of 0.5 °C. Moreover, the performance of the model with the internal air element active is better than the model which deactivates the internal air elements when comparing the outflow temperature of the pipe circuit.

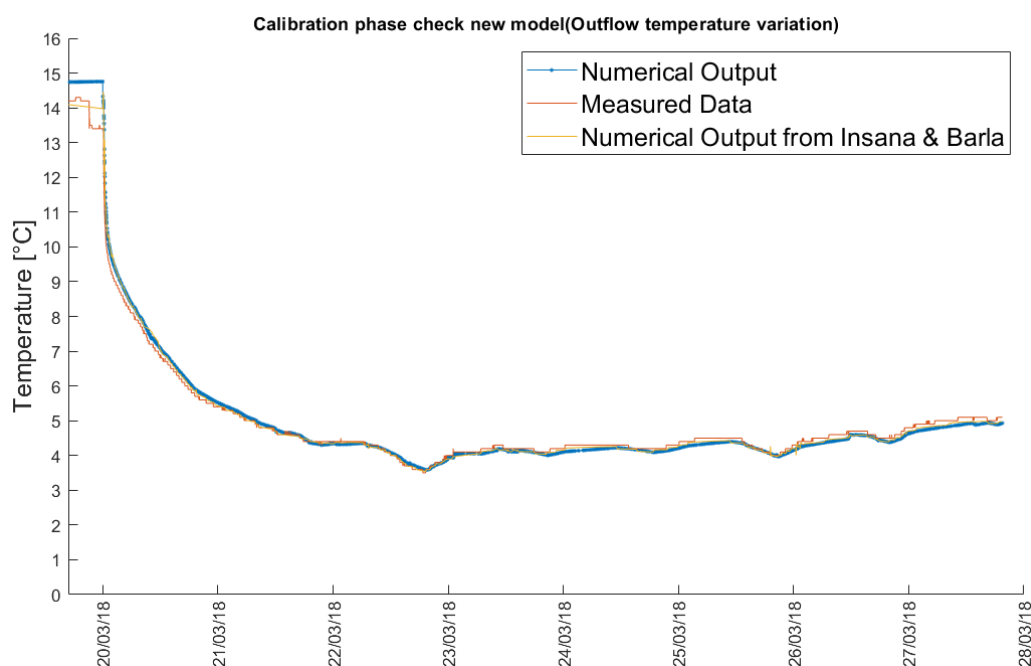


Fig. 50. calibration phase check of the new model

Furthermore, four validation phase checks of the model with air elements active are performed considering different functions of thermal activation similarly as done in the preliminary verification, namely two tests of Ground Heating (180305_G_H_T45_179180 and 180309_G_H_T45_179180), one test of Ground Cooling (180727_G_C_T10_179180) and one test of Air Heating (180804_A_H_T55_179180). The information of these tests is listed in **Table. 1**. Comparing the calculated and measured outflow temperature, the results of the four validation tests are acceptable as seen in **Fig. 51**. Furthermore, with different trials of fluid flux value, it is observed that the outflow temperature of the pipe circuit is less influenced by the change of internal air condition compared to the lining temperature, which means that the performance of the thermal activation in terms of absorbing heat or cold from users is less influenced by the short-term change in the internal air of tunnel.

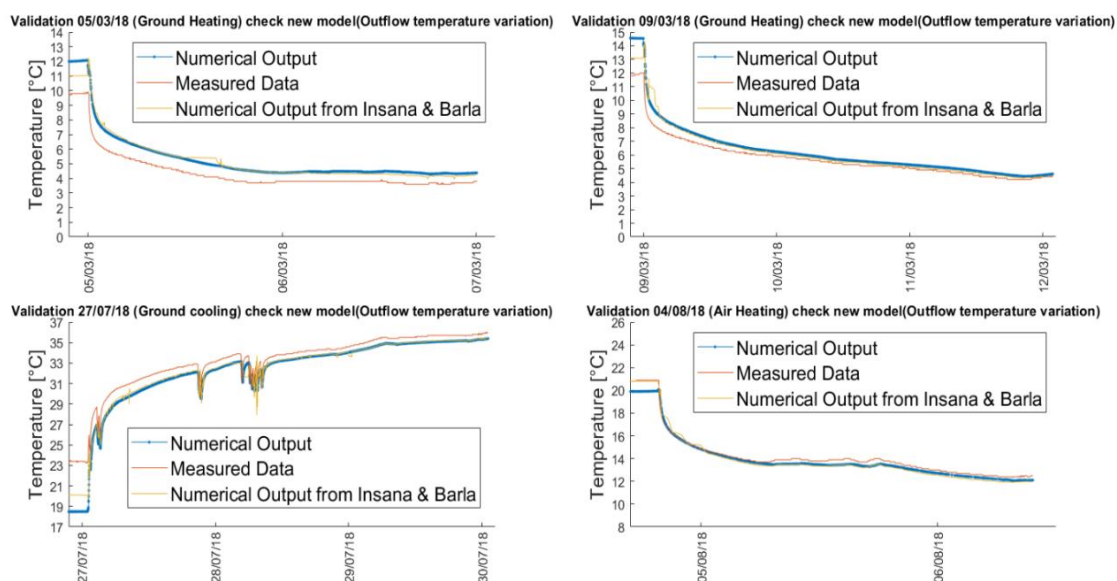


Fig. 51. Validation phase check of the new model

The calculated lining temperature is compared with the measured data as well. The internal air temperature of tunnel is measured very close to the intrados of lining (Insana, 2020). It is reasonable that, in winter, the air temperature close to the lining intrados is higher than that at the tunnel opening center since the lining and ground possess a higher temperature than the internal air in general during winter. Hence, applying the internal air temperature measured close to the intrados at all the nodes of the tunnel opening at slice 1 can lead to a bias in the calculated lining temperature, which should be higher than the measured lining temperature as expected. Instead of using the internal air temperature measured close to the intrados, the measured external air temperature is used as input for the internal air temperature, knowing that the experimental site is generally open to the external air (Insana, 2020). The result of the lining temperature for SI2 sensor is shown in **Fig. 52**, in which the gap between the calculated and measured temperature is generally 0.5 °C, which is acceptable considering the accuracy of the sensor. In terms of St4 sensor, the result is even better considering a gap of 0.4 °C at intrados in general as shown in **Fig. 53**. While for the lining temperature calculated at the extrados, the model yields a good result matching the measured data both for SI2 and St4 sensors with a gap less than 0.3°C in general. However, it is worth pointing out that the lining temperature is sensitive to the change in the internal air, including temperature change and fluid flux condition change. A high value of the fluid flux leads to a strong convection in the internal air, which will force the internal air close to the intrados to follow the air temperature variation tendency. In such way, the air close to the lining intrados will lose the bumper effect in terms of temperature fluctuation. The strong temperature change of the air close to the lining intrados leads to a strong temperature variation in the lining temperature as well. Nevertheless, despite the strong fluctuation of the air temperature and lining temperature, the outflow temperature of pipe circuit is much more stable to follow the trend of the inflow temperature of pipe circuit.

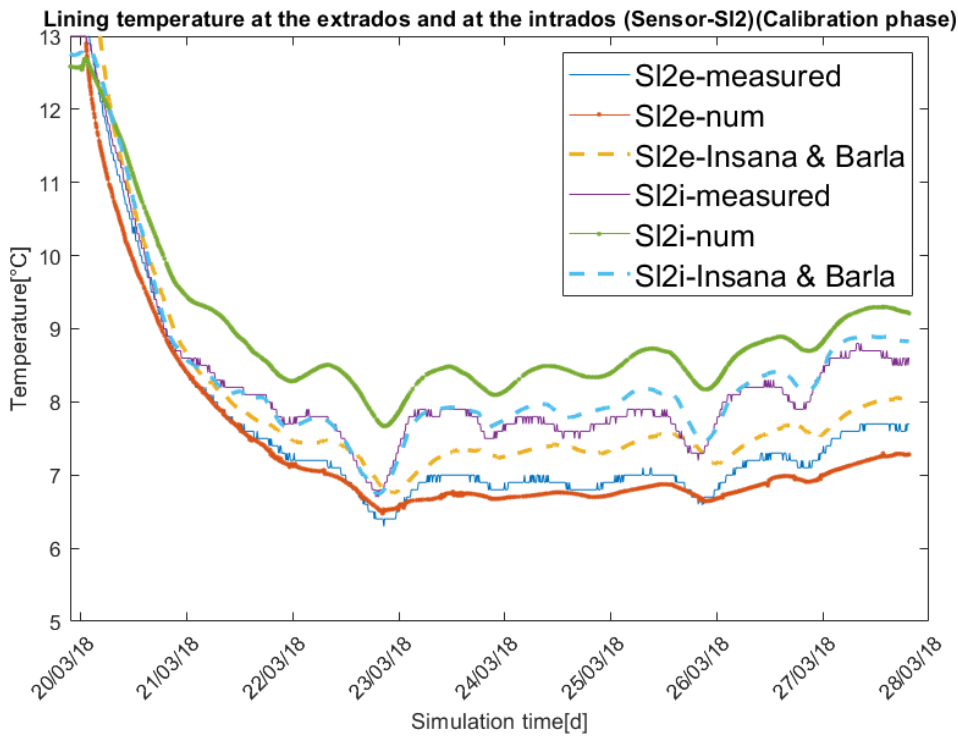


Fig. 52. Lining temperature comparison (Sensor-SI2)

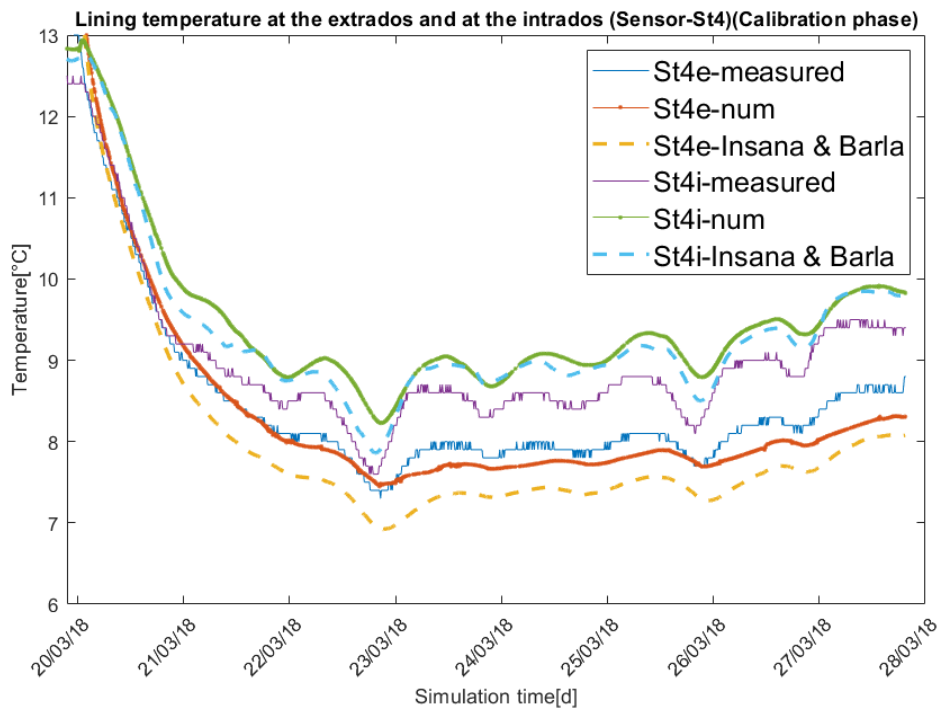


Fig. 53. Lining temperature comparison (Sensor-St4)

4.5 Conclusions from the calibration and validation tests

- Temperature BC is found to be a better choice compared to Heat transfer BC in the trial test in our study. Under a strong convection condition, the calculated internal air temperature at the measured point can follow the rapid change of the input temperature greatly with Temperature BC while Heat transfer BC can not lead to the same effect.
- The methodology implemented to calibrate and validate the model with respect to the measured data in this chapter is to examine different boundary conditions and the corresponding assigned value, to be specific, where to apply Temperature BC and the value of the Fluid-flux BC. After plenty of trials, for the internal air, Temperature BC on the all the nodes of the tunnel opening of the first slice. Moreover, the assigned value for Fluid-flux varies from test to test ranging from 0.005 m/s to 0.015 m/s during the calibration and validation phase so to reproduce the test result in terms of lining temperature and pipe circuit outflow temperature. However, in normal cases, the pipe circuit is used during the service life of the tunnel, which will lead to a higher value of air flow velocity. Therefore, a fluid flux BC of 0.1 m/s is assigned to take this fact into account in the next chapter.
- For the model with the internal air activated, the calculated outflow temperature of pipe circuit is generally less than 0.5 °C compared to the measured data, which is sufficiently accurate considering the accuracy of the temperature sensor of 0.5 °C during the calibration and validation tests. Moreover, the lining temperature is checked for the calibration test, in which the gap between the calculated and measured lining temperature at intrados is generally 0.5 °C for SI2 sensor and 0.4 °C for St4 sensor, which is acceptable, while the result for the calculated temperature at the lining extrados is even better considering a smaller gap of less than 0.3 °C in general both for SI2 and St4 sensors.

Chapter 5

Influence of the thermal activation on the internal air temperature of tunnel

5.1 Introduction

After the calibration and validation of the model that replicates the Enertun prototype, the reliability of the numerical model is satisfied. The next step is to investigate how will the thermal activation of the tunnel lining influence the internal air temperature of tunnel. The numerical model used is the one that is calibrated and validated but with 6 rings of Enertun heat carrier pipes equipped, as seen in **Fig. 54**.

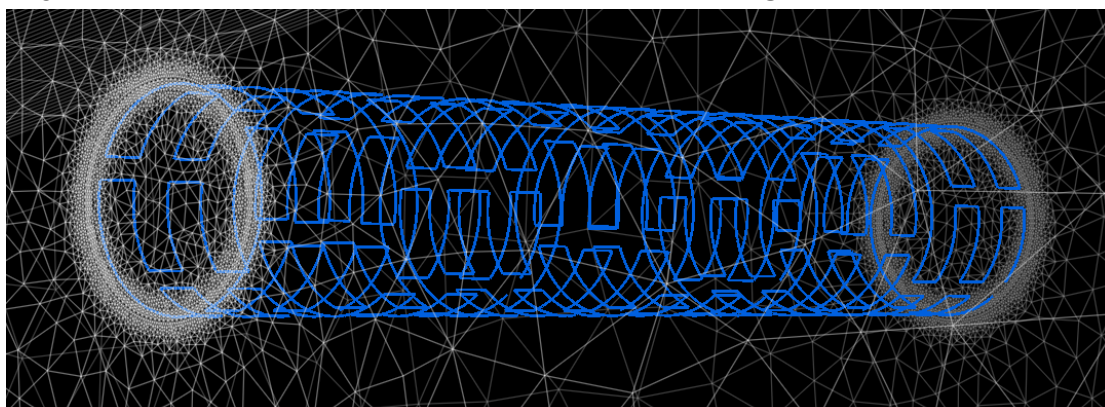


Fig. 54. Numerical model with 6 rings of heat carrier pipes (only ground configuration is shown)

5.2 Simplified input time series of temperature

As observed from the record of annual variation of the air temperature and tunnel temperature, it is useful to simplified the annual temperature with a sinusoidal function considering the annual mean temperature and the seasonal fluctuation of the air and the tunnel internal air. However, the daily fluctuation of temperature is ignored. The air temperature and tunnel air temperature time series start from April. Those used for Turin and $\pm 3^{\circ}\text{C}$ on the base of Turin data are reported as followed in **Fig. 55**.

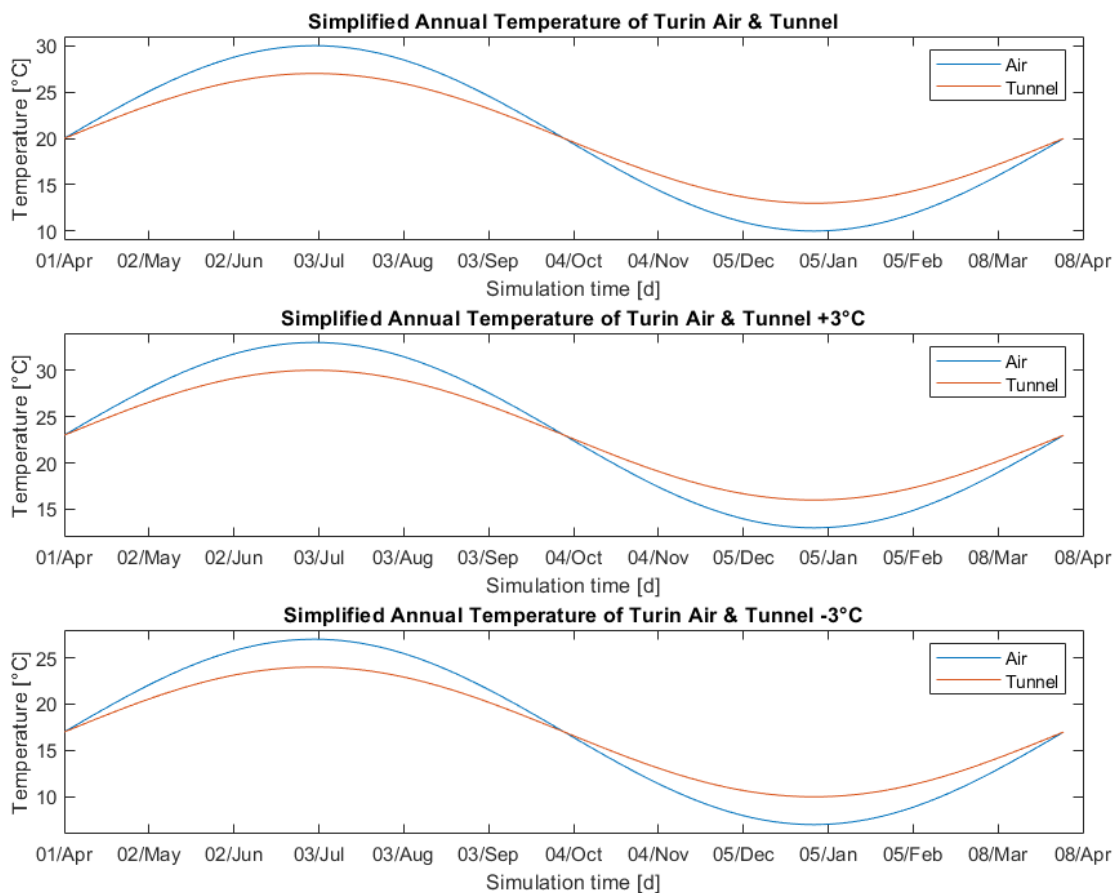


Fig. 55. Simplified Annual temperature of air and tunnel in Turin

In terms of the inlet temperature variation of the heat carrier pipe (both Ground configuration and Air configuration), the simplification of the inlet temperature performed regarding the record of the Enertun prototype. For summer (from May to August), it is set as 36 °C. For winter (from November to February of the subsequent year), it is set as 2 °C. For the other month, so to say spring and autumn when thermal activation is kept off, it is set as 17.3 °C, which is shallow ground temperature of Turin. The simplified Inlet temperature time series for ground configuration start from April, which coincides with that of the air temperature and tunnel air temperature time series. The simplified inlet temperature of Ground configuration is shown in **Fig. 56**.

In order to control the thermal activation process automatically in the numerical model, another time series can be applied for the fluid flux BC of the pipe circuit. The velocity for the fluid flow velocity in the pipe circuit is set to be 0.9 m/s when it is on and 0 m/s when it is off (Rosso, 2020). Considering different thermal activation modes, the fluid flow velocity time series is plotted together with inflow temperature in **Fig. 56**.

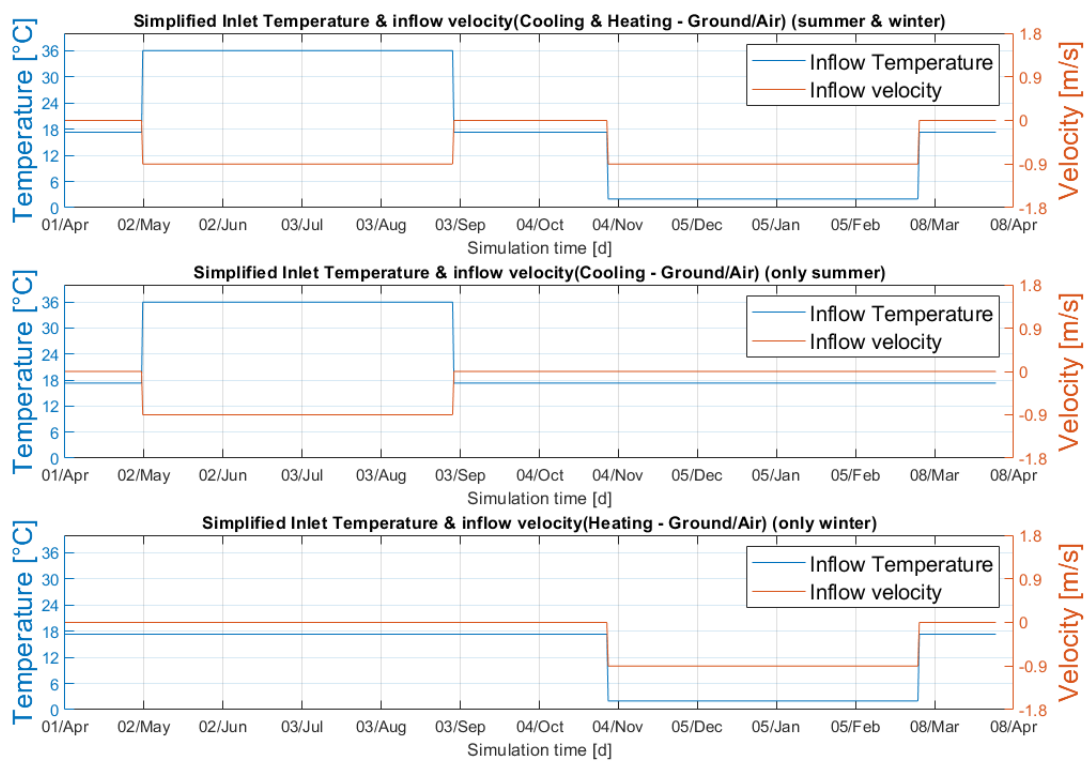


Fig. 56. Simplified inlet temperature (Ground & Air configuration)

Furthermore, two observation points A and B are set in slice 43, which is of the middle length of the model, to capture the temperature variation of the internal air at the tunnel center and close to the tunnel lining intrados as shown in **Fig. 57**.

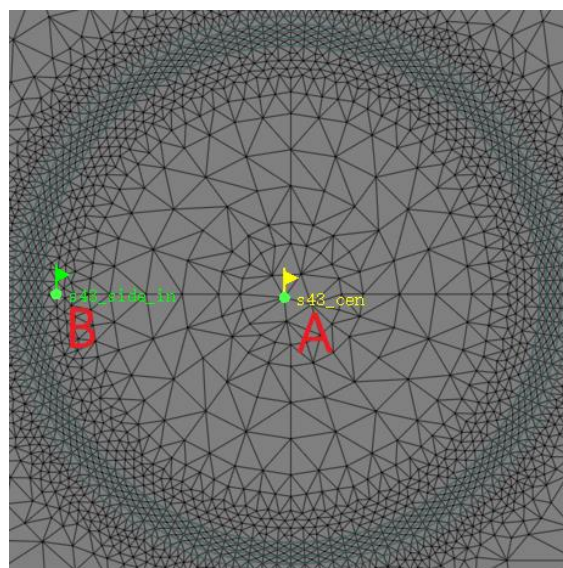


Fig. 57. Observation points in slice 43

5.3 Response on thermal activation with ground configuration

5.3.1 Simulation test introduction

To simulate the response of internal air on thermal activation of the tunnel linings with Ground configuration, several simulations are run with the boundary conditions summarized as followed and the simulation tests information summarized in **Table 4**.

- Boundary conditions on the internal air:
 - Temperature BC on the first slice
 - Fluid flux BC on the first slice (-0.1 m/s) and the last slice (0.1 m/s)

Table 4 Simulation tests information (Ground configuration)

| Test number | Thermal activation mode | Input air temperature signal | Input tunnel temperature signal | Inflow velocity [m/s] | Internal Air flow velocity [m/s] |
|-------------|-------------------------|------------------------------|---------------------------------|-----------------------|----------------------------------|
| 1 | Ground_only summer | Turin | Turin | 0.9 | 0.1 |
| 2 | Ground_only winter | Turin | Turin | 0.9 | 0.1 |
| 3 | Ground_summer&winter | Turin | Turin | 0.9 | 0.1 |
| 4 | Ground_only summer | Turin -3 °C | Turin -3 °C | 0.9 | 0.1 |
| 5 | Ground_only winter | Turin -3 °C | Turin -3 °C | 0.9 | 0.1 |
| 6 | Ground_summer&winter | Turin -3 °C | Turin -3 °C | 0.9 | 0.1 |
| 7 | Ground_only summer | Turin +3 °C | Turin +3 °C | 0.9 | 0.1 |
| 8 | Ground_only winter | Turin +3 °C | Turin +3 °C | 0.9 | 0.1 |
| 9 | Ground_summer&winter | Turin +3 °C | Turin +3 °C | 0.9 | 0.1 |

The simulation is composed of one year with thermal activation off and another two years of thermal activation on, so to investigate the effect of thermal activation on the internal air and to study the energy cumulation effect due to continuous thermal activation.

5.3.2 Interpretation of simulation test result

It is possible to check the result in terms of temperature directly on FEFLOW, with the view component of temperature activated. In such a way, the temperature field of the whole 3D model composed of the tunnel opening and the ground is displayed with a color scale indicating different temperature as shown in **Fig. 58**, in which the temperature field corresponding to the last time step, so the end of the simulation test.

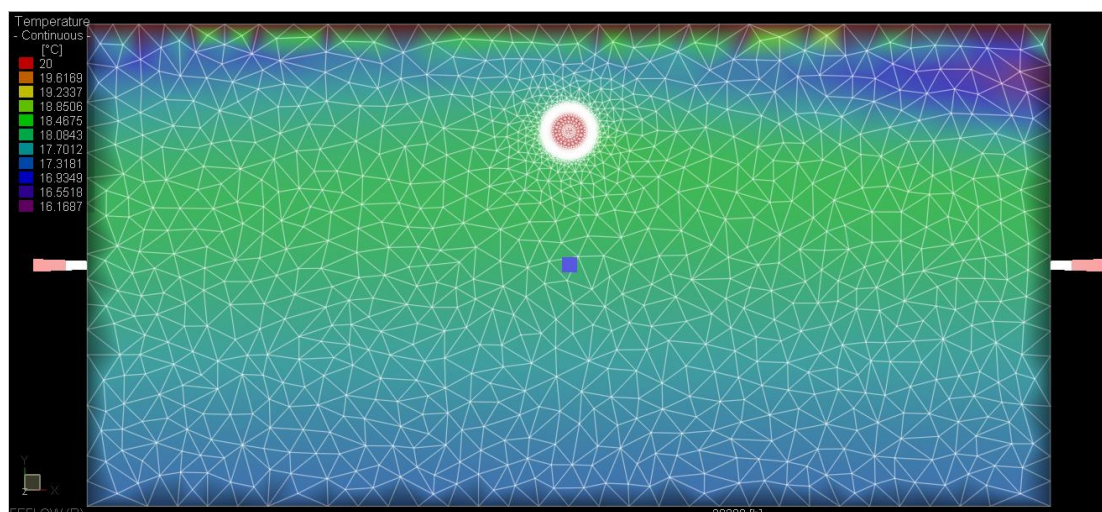


Fig. 58. Temperature field of the 3D model - Test 1

Besides inspecting the data on FEFLOW, data extraction is another option since the test result was recorded. In this study, the temperature history is featured and extracted. Afterwards, the temperature data is processed and plotted with Matlab, in which the data can be arranged in a way to be easily compared together with the maximum and minimum temperature information tapped. Furthermore, the input temperature data and the inflow temperature are plotted together as well so to provide comparison with the calculated internal air temperature, and the observation point location is also shown with an image attached.

The temperature history plot of Test 1 is shown in **Fig. 59**. As it is observed, the internal air temperature at the middle of the model (slice 43) is slightly different from the input one assigned with Temperature BC. Such difference is greater close to the lining than at the tunnel center. This is reasonable as it is the result of heat exchange between the internal air and the lining. Similar phenomenon can be observed in the other simulation tests as well. However, such difference is small and negligible under the air flow velocity of 0.1 m/s, which is sufficiently strong to guarantee the strong convection. Furthermore, the temperature variation due to thermal activation with ground configuration at the peak temperature point in summer are approximately +0.22 °C at Observation point A and +0.86 °C at Observation point B. The variation is greater at point B since it is closer to the thermal pipe circuit. The energy cumulation effect are of the order of 10^{-4} °C at A and 10^{-3} °C at B, which is rather small and negligible.

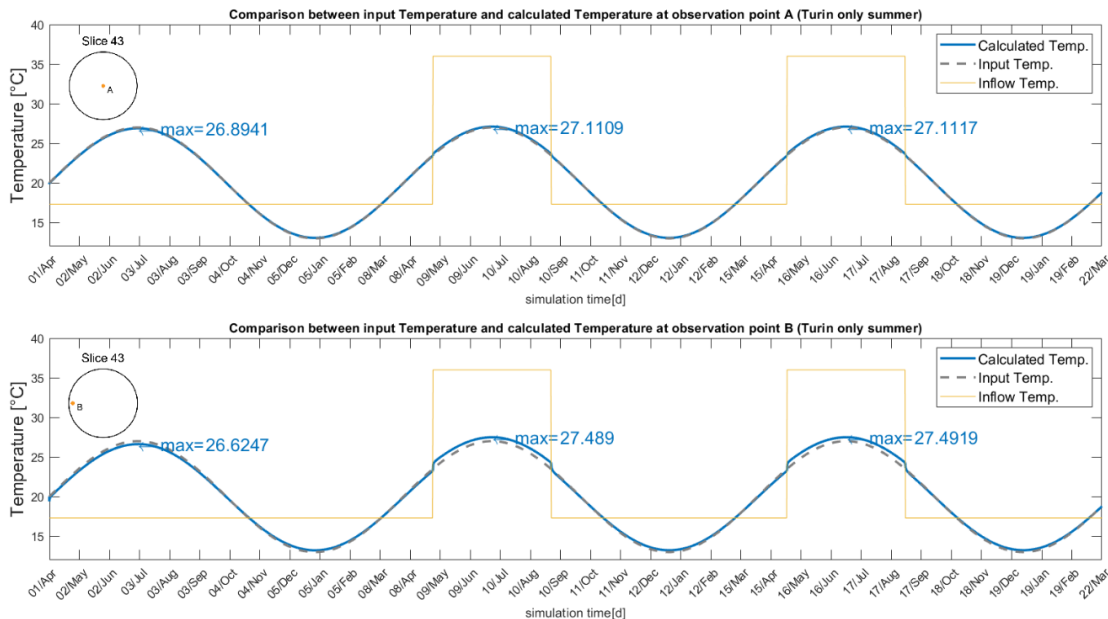


Fig. 59. Temperature variation at observation points A&B - Test 1

The temperature history plot of Test 2 is shown in **Fig. 60**. The temperature variation due to thermal activation with ground configuration at the lowest temperature point in winter are approximately $-0.22\text{ }^{\circ}\text{C}$ at Observation point A and $-0.90\text{ }^{\circ}\text{C}$ at Observation point B. The energy cumulation is not observed in winter. The min temperature is even higher in the third year than in the second year, which probably means that the model needs a longer time to get stable.

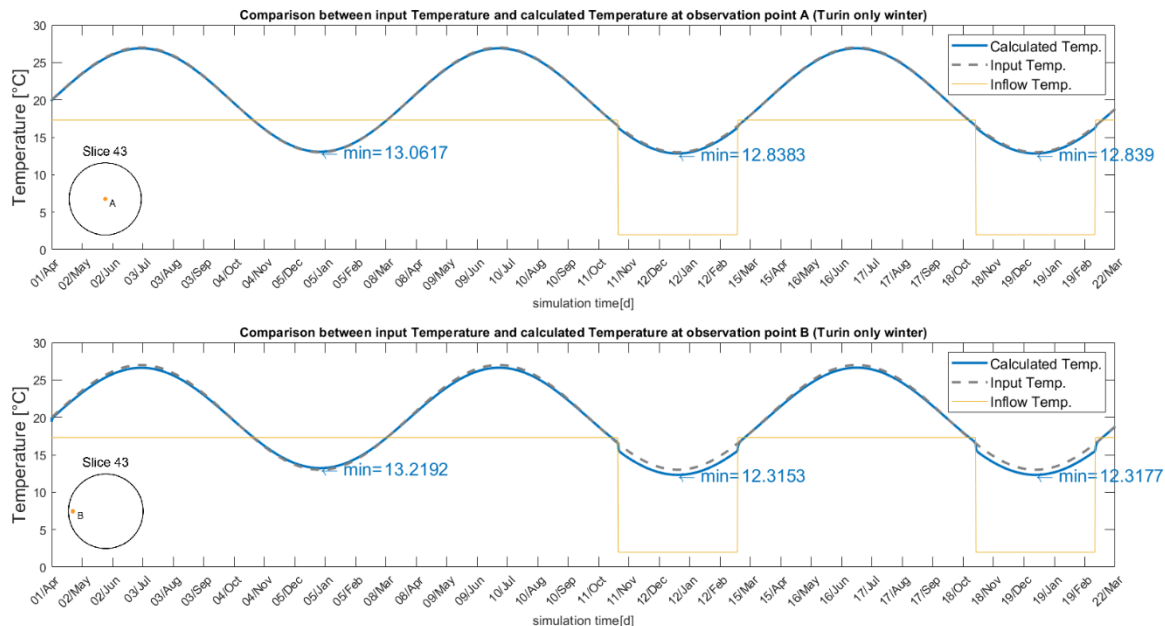


Fig. 60. Temperature variation at observation points A&B - Test 2

The temperature history plot of Test 3 is shown in **Fig. 61**. To compare with Fig. 58 and Fig. 59, it is found that the variation of temperature are the same as those obtained with thermal activation on only in summer or winter, which are approximately $+0.22\text{ }^{\circ}\text{C}$ at Observation point A and $+0.86\text{ }^{\circ}\text{C}$ at Observation point B in summer and approximately $-0.22\text{ }^{\circ}\text{C}$ at Observation point A and $-0.90\text{ }^{\circ}\text{C}$ at Observation point B in winter. The cumulation of energy is similar as well, which are of the order of $10^{-4}\text{ }^{\circ}\text{C}$ at point A and $10^{-3}\text{ }^{\circ}\text{C}$ at point B in summer.

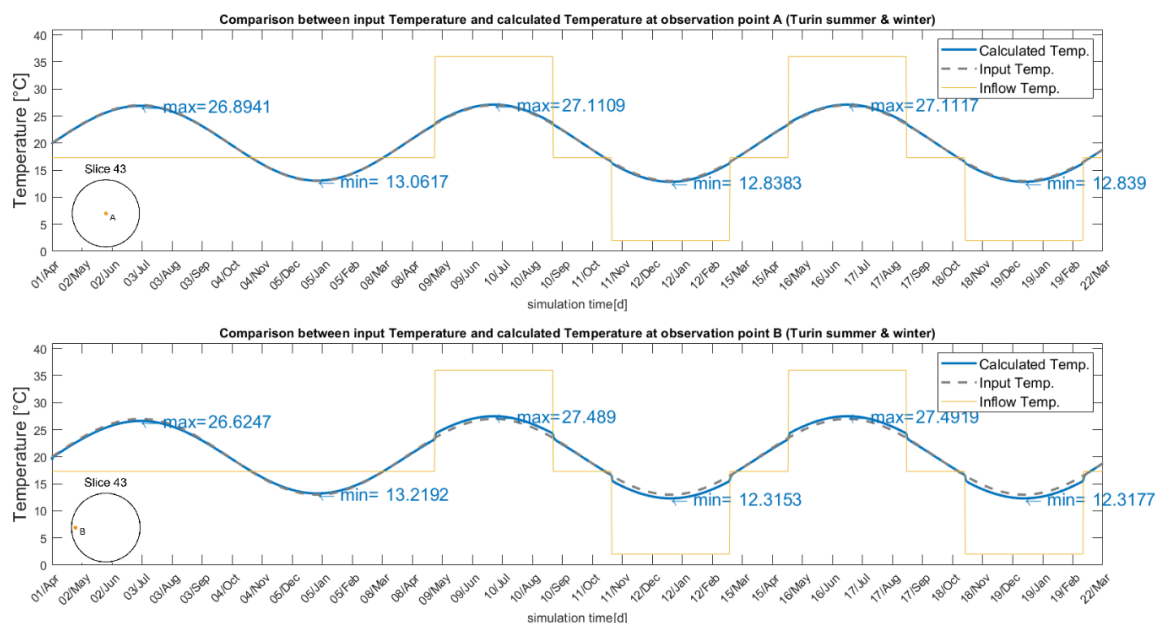


Fig. 61. Temperature variation at observation points A&B - Test 3

For Test 4, Test 5 and Test 6, the input air and tunnel internal air temperature are reduced by $3\text{ }^{\circ}\text{C}$ while the temperature of ground remains always the same as $17.3\text{ }^{\circ}\text{C}$. The 3D temperature field of Test 4 at the end of the simulation test is shown in **Fig. 62**, where the color scale changed due to the change in the input data. As it is observed, with such reduction of the temperature, the internal air temperature is getting so close to the ground temperature.

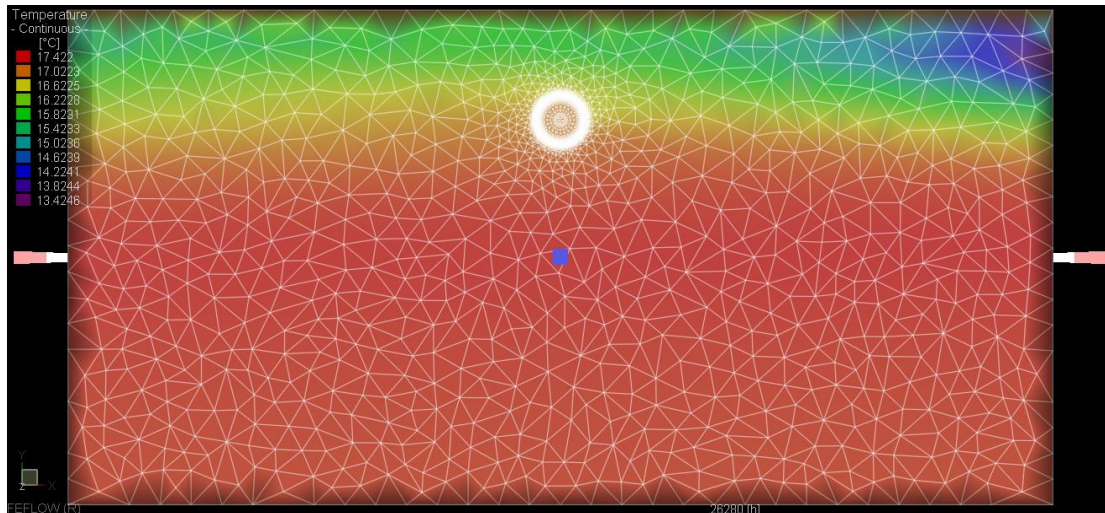


Fig. 62. Temperature field of the 3D model - Test 4

The temperature history plot of Test 4 is shown in **Fig. 63**. As it is observed, the temperature variation in the internal air due to the thermal activation in summer increases to approximately +0.25 °C at point A and +1 °C at point B. Obviously, this is due to the increase of the temperature difference between the tunnel internal air and the fluid of the pipe circuit. However, the difference in terms of the energy performance of the internal air following this change in the input temperature is quite small. Furthermore, in Test 4, energy cumulation due to thermal activation in summer is not observed any more as compared to Test 1.

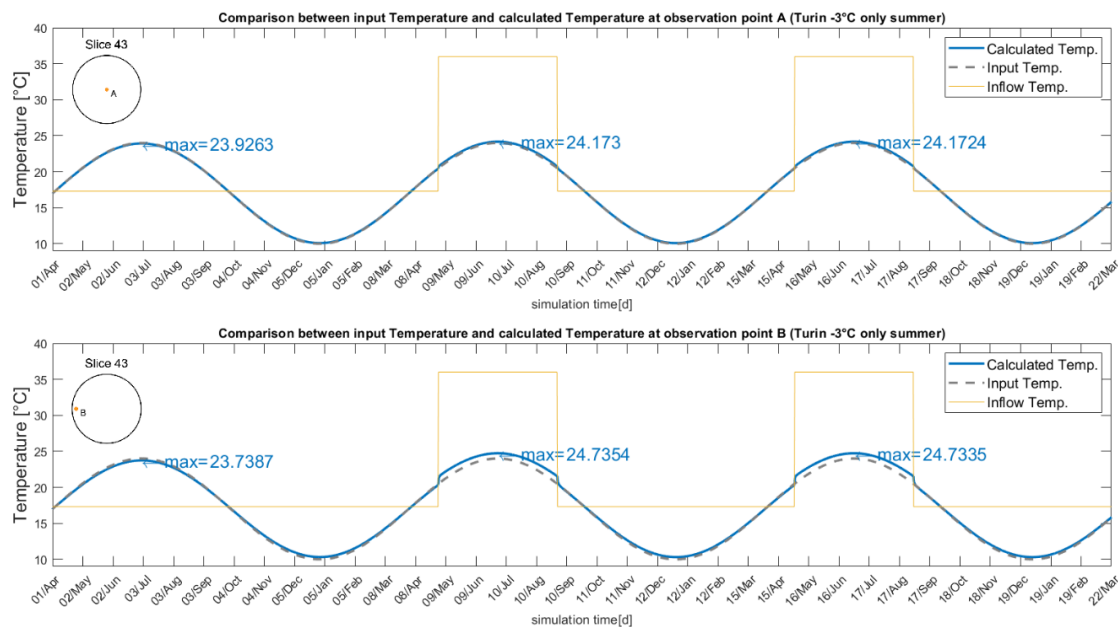


Fig. 63. Temperature variation at observation points A&B - Test 4

The temperature history plot of Test 5 is shown in **Fig. 64**. Knowing that the input temperature of air and internal air of tunnel are reduced by 3 °C, the simulation result of Test 5 shows a smaller temperature variation of the internal air due to the thermal activation in winter, as expected. The temperature variation is approximately -0.19 °C at point A and -0.76 °C at point B. However, energy cumulation is observed in this test simulation, which is not observed in winter before as in Test 2 and Test 3. The order of energy cumulation is 10^{-4} °C at point A and 10^{-3} °C at point B.

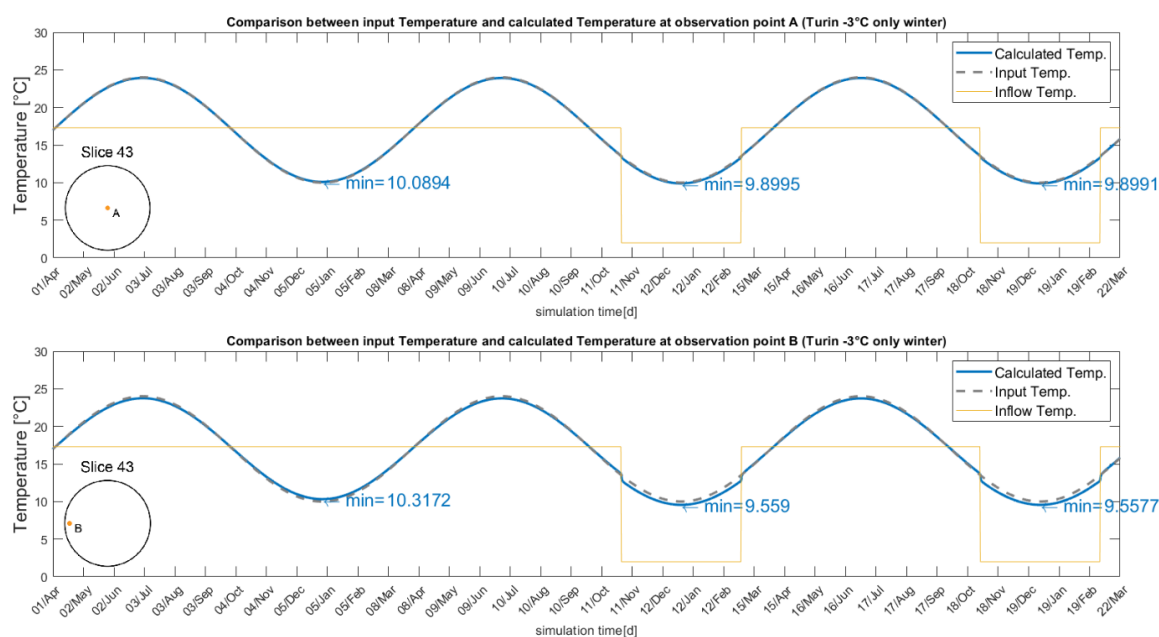


Fig. 64. Temperature variation at observation points A&B - Test 5

The temperature history plot of Test 6 is shown in **Fig. 65**. As it is observed, to activate the pipe circuit both in summer and winter does not lead to change in the value of temperature variation due to the thermal activation of tunnel lining, which is similar to that observed in Test 1, 2 and 3. At point A, the temperature variations are approximately +0.25 °C in summer and -0.19 °C in winter. While at point B, they are approximately +1 °C in summer and -0.76 °C in winter. Also, energy cumulation is observed only in winter, which are of 10^{-4} °C at point A and 10^{-3} °C at point B.

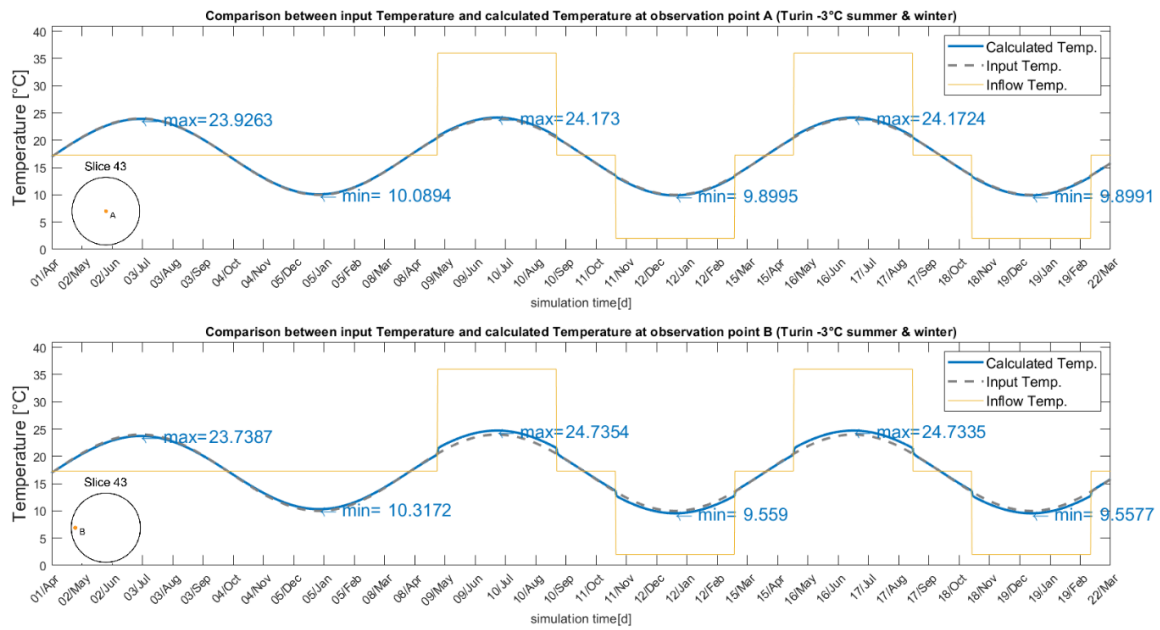


Fig. 65. Temperature variation at observation points A&B - Test 6

Comparing the results of Test 4, 5 and 6 with those of Test 1, 2 and 3, it is found that the reduction of input temperature in both the external air and tunnel internal air, with the same temperature as 17.3 °C for the ground, leads to a higher temperature difference in summer and lower temperature difference in winter between the internal air temperature and pipe circuit fluid temperature. Consequently, a higher temperature variation of the internal air temperature in summer and a lower temperature variation in winter are reasonable. Furthermore, the reduction of input temperature changes also the energy cumulation condition. For Test 1, 2 and 3, energy cumulation is observed only in summer, while for Test 4, 5 and 6 it is observed only in winter.

For Test 7, Test 8 and Test 9, the input air and tunnel internal air temperature are increased by 3 °C but the ground temperature remains as 17.3 °C. The 3D temperature field of Test 7 at the end of the simulation test is shown in **Fig. 66**. It is clearly seen that with the increasement of the input temperature, the internal air temperature of tunnel is so different from the ground temperature, as the color scales of tunnel opening and the surrounding ground is different by almost 7 grades.

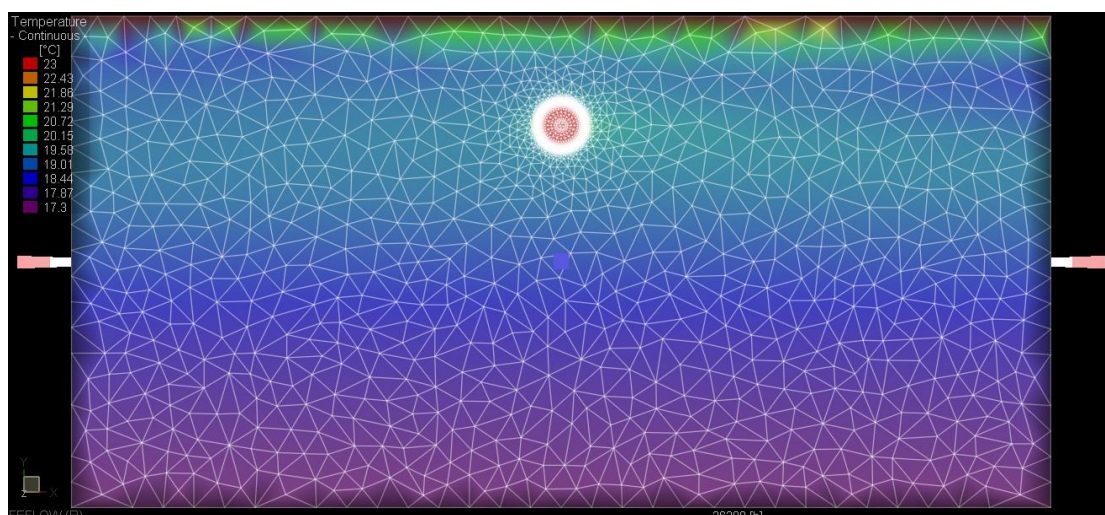


Fig. 66. Temperature field of the 3D model - Test 7

The temperature history plot of Test 7 is shown in **Fig. 67**. Hence, as it is observed, the temperature variation in the internal air due to the thermal activation in summer reduces to approximately +0.19 °C at point A and +0.74 °C at point B. The smaller difference between the input temperature and the inflow temperature of the pipe circuit leads to a smaller temperature variation due to the thermal activation. Furthermore, the higher input temperature produces a higher level of energy cumulation in summer, which are both of 10^{-3} °C at point A and point B, but apparently higher at point B.

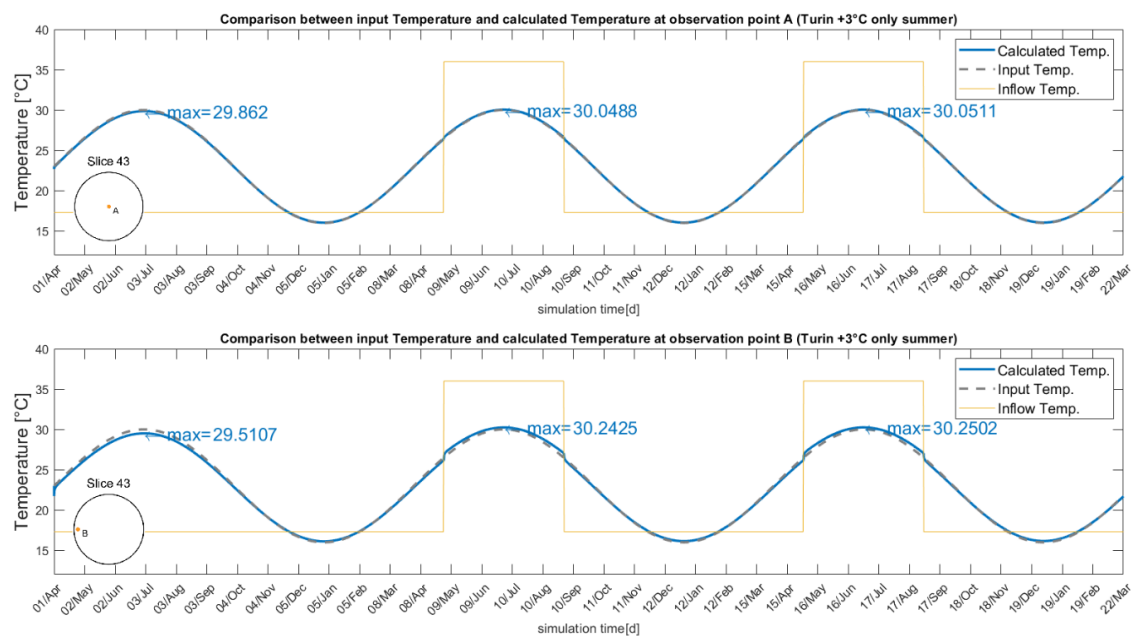


Fig. 67. Temperature variation at observation points A&B - Test 7

The temperature history plot of Test 8 is shown in **Fig. 68**. As it is expected, the higher difference between the input temperature and the inflow temperature of the pipe circuit in winter leads to a greater temperature variation in the internal air due to the thermal activation. The temperature variations decrease down to approximately $-0.26\text{ }^{\circ}\text{C}$ at point A and $-1.05\text{ }^{\circ}\text{C}$ at point B. Energy cumulation due to the thermal activation is not observed in winter.

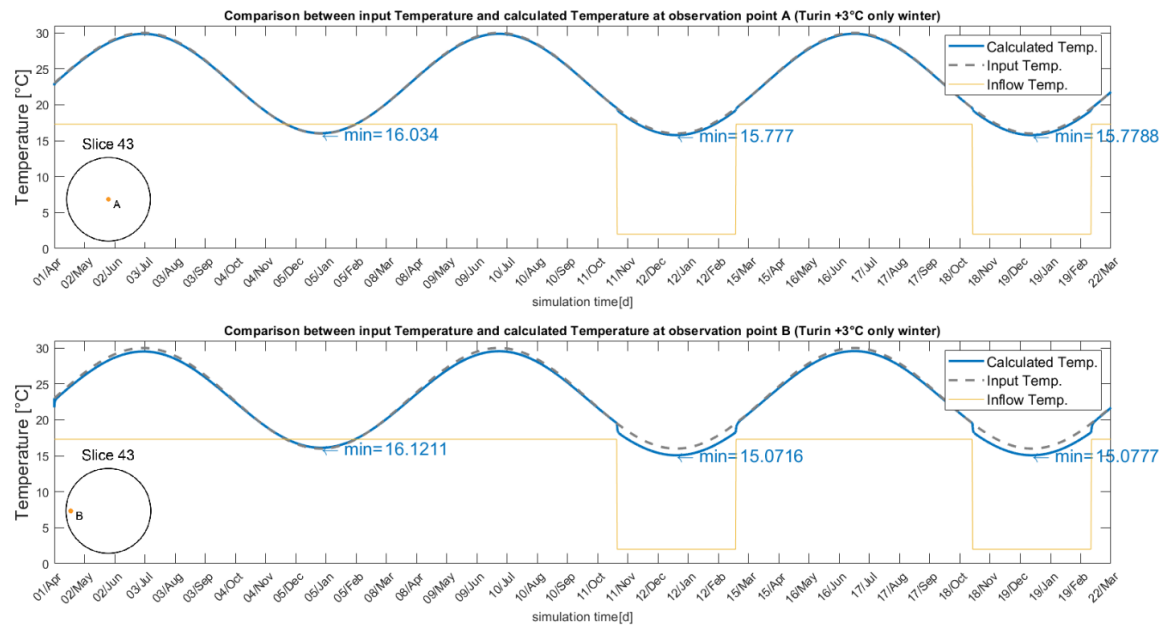


Fig. 68. Temperature variation at observation points A&B - Test 8

The temperature history plot of Test 9 is shown in **Fig. 69**. Similarly, the thermal activation in both summer and winter brings the same effect to the internal air as they are with the thermal activation in summer and winter separately, which are approximately $+0.19\text{ }^{\circ}\text{C}$ at point A and $+0.74\text{ }^{\circ}\text{C}$ at point B in summer and approximately $-0.26\text{ }^{\circ}\text{C}$ at point A and $-1.05\text{ }^{\circ}\text{C}$ at point B in winter. Also, the energy cumulation is observed only in summer as well under the input temperature used in this case, which are both of $10^{-3}\text{ }^{\circ}\text{C}$ at point A and a bit higher at point B.

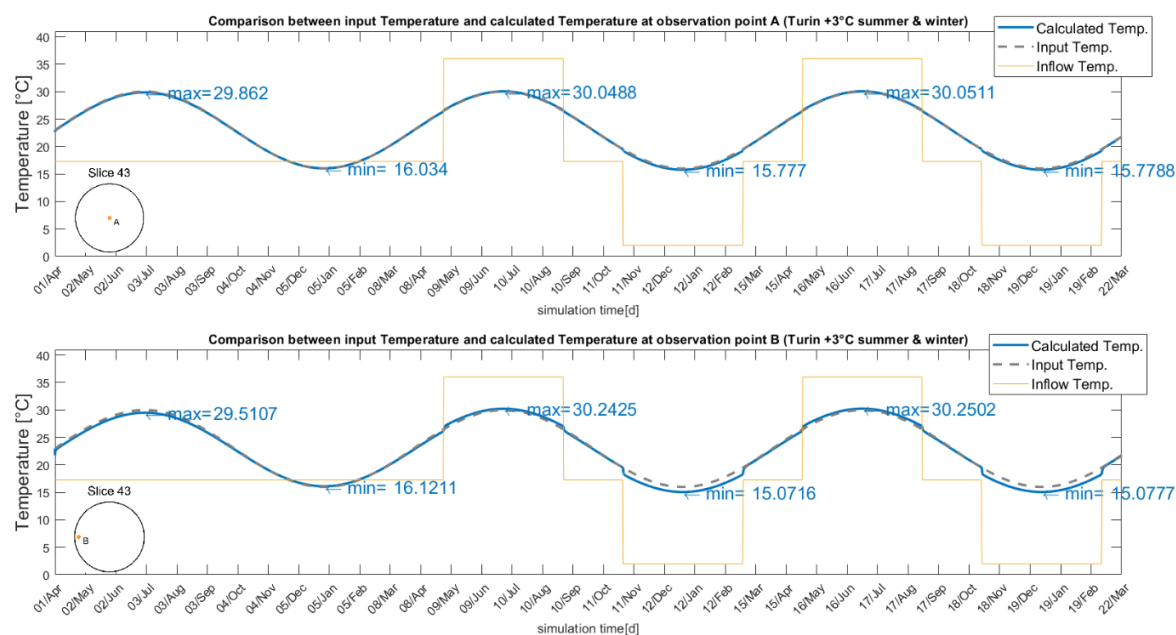


Fig. 69. Temperature variation at observation points A&B - Test 9

The increment of input temperature brings an inverse effect to the temperature variation in the internal air due to the thermal activation compared with the effect following the reduction of input temperature. In summer, the temperature variation of the internal air due to thermal activation is lower while in winter it is higher. In terms of energy cumulation, the situation is similar as it is observed only in summer but with a higher level of cumulation.

All the interpretation results of different tests with Ground configuration are summarized in **Table 5** for observation point A and in **Table 6** for observation point B, respectively.

From the simulation test result, it is found that the thermal response of the internal air due to the thermal activation with the pipe circuit of ground configuration is not so strong, which are around ± 0.2 °C at point A and ± 0.8 °C at point B. The intensity of the temperature variation due to thermal activation is affected by the level of the input temperature. Furthermore, energy cumulation is observed but quite limited, which is strongly influenced by the input temperature as well. Different input temperature can even change the period during which the energy cumulation phenomenon is observed.

Table 5 Test interpretation result summary (Observation point A, Ground configuration)

| Test number | Peak (normal summer) | Lowest (normal winter) | Peak (thermo-active summer) | Lowest (thermo-active winter) | Variation (summer) | Variation (winter) | Order of cumulation |
|-------------|----------------------|------------------------|-----------------------------|-------------------------------|--------------------|--------------------|---------------------|
| - | [°C] | [°C] | [°C] | [°C] | [°C] | [°C] | [°C] |
| 1 | 26.8941 | - | 27.1117 | - | 0.2176 | - | 1.00E-04 |
| 2 | - | 13.0617 | - | 12.8383 | - | -0.2234 | - |
| 3 | 26.8941 | 13.0617 | 27.1117 | 12.8383 | 0.2176 | -0.2234 | 1.00E-04 |
| 4 | 23.9263 | - | 24.173 | - | 0.2467 | - | - |
| 5 | - | 10.0894 | - | 9.8991 | - | -0.1903 | 1.00E-04 |
| 6 | 23.9263 | 10.0894 | 24.173 | 9.8991 | 0.2467 | -0.1903 | 1.00E-04 |
| 7 | 29.862 | - | 30.0511 | - | 0.1891 | - | 1.00E-03 |
| 8 | - | 16.034 | - | 15.777 | - | -0.257 | - |
| 9 | 29.862 | 16.034 | 30.0511 | 15.777 | 0.1891 | -0.257 | 1.00E-03 |

Table 6 Test interpretation result summary (Observation point B, Ground configuration)

| Test number | Peak (normal summer) | Lowest (normal winter) | Peak (thermo-active summer) | Lowest (thermo-active winter) | Variation (summer) | Variation (winter) | Order of cumulation |
|-------------|----------------------|------------------------|-----------------------------|-------------------------------|--------------------|--------------------|---------------------|
| - | [°C] | [°C] | [°C] | [°C] | [°C] | [°C] | [°C] |
| 1 | 26.6247 | - | 27.4919 | - | 0.8672 | - | 1.00E-03 |
| 2 | - | 13.2192 | - | 12.3153 | - | -0.9039 | - |
| 3 | 26.6247 | 13.2192 | 27.4919 | 12.3153 | 0.8672 | -0.9039 | 1.00E-03 |
| 4 | 23.7387 | - | 24.7354 | - | 0.9967 | - | - |
| 5 | - | 10.3172 | - | 9.5577 | - | -0.7595 | 1.00E-03 |
| 6 | 23.7387 | 10.3172 | 24.7354 | 9.5577 | 0.9967 | -0.7595 | 1.00E-03 |
| 7 | 29.5107 | - | 30.2502 | - | 0.7395 | - | 1.00E-03 |
| 8 | - | 16.1211 | - | 15.0716 | - | -1.0495 | - |
| 9 | 29.5107 | 16.1211 | 30.2502 | 15.0716 | 0.7395 | -1.0495 | 1.00E-03 |

5.4 Response on thermal activation with Air configuration

5.4.1 Simulation test introduction

To simulate the response of internal air on thermal activation of the tunnel linings with Air configuration, several simulations are run with the boundary conditions summarized as followed and the simulation tests information summarized in **Table 7**.

- Boundary conditions on the internal air:
 - Temperature BC on the first slice
 - Fluid flux BC on the first slice (-0.1 m/s) and the last slice (0.1 m/s)

Table 7 Simulation tests information (Air configuration)

| Test number | Thermal activation mode | Input air temperature signal | Input tunnel temperature signal | Inflow velocity [m/s] | Internal Air flow velocity [m/s] |
|-------------|-------------------------|------------------------------|---------------------------------|-----------------------|----------------------------------|
| 10 | Air_only summer | Turin | Turin | 0.9 | 0.1 |
| 11 | Air_only winter | Turin | Turin | 0.9 | 0.1 |
| 12 | Air_summer&winter | Turin | Turin | 0.9 | 0.1 |
| 13 | Air_only summer | Turin -3 °C | Turin -3 °C | 0.9 | 0.1 |
| 14 | Air_only winter | Turin -3 °C | Turin -3 °C | 0.9 | 0.1 |
| 15 | Air_summer&winter | Turin -3 °C | Turin -3 °C | 0.9 | 0.1 |
| 16 | Air_only summer | Turin +3 °C | Turin +3 °C | 0.9 | 0.1 |
| 17 | Air_only winter | Turin +3 °C | Turin +3 °C | 0.9 | 0.1 |
| 18 | Air_summer&winter | Turin +3 °C | Turin +3 °C | 0.9 | 0.1 |
| 19 | Air_summer&winter | Turin | Turin | 0.9 | 0 |
| 20 | Air_summer&winter | Turin | Turin | 0.9 | 0.0001 |

The simulation with Air configuration is composed of one year with thermal activation off and another two years of thermal activation on as well.

5.4.2 Interpretation of simulation test result

To activate the tunnel lining thermally with Air configuration leads to a stronger influence to the internal air of the tunnel, apparently due to the fact that the pipe circuit of Air configuration is closer to the internal air than Ground configuration.

The 3D temperature field of the Test 10 at the end of the simulation test is shown in **Fig. 70**. As it is observed, the temperature field is similar to that with the same input data and Ground configuration, since the effect of the thermal activation fades away quickly, either with Air configuration or Ground configuration.

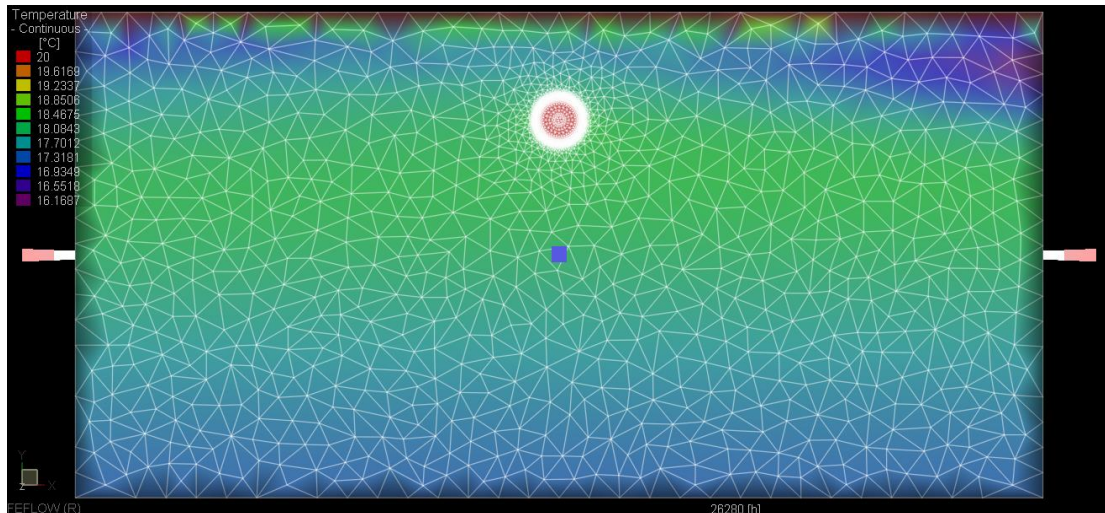


Fig. 70. Temperature field of the 3D model - Test 10

The temperature history plot of Test 10 is shown in **Fig. 71**. As it is observed, before the thermal activation, the internal air temperature at point A and B are the same as in Test 1, which are slightly different from the input temperature of the internal air. the temperature variation due to thermal activation with ground configuration at the peak temperature point in summer are approximately +0.29 °C at Observation point A and +1.17 °C at Observation point B, which are greater than those observed in Test 1. Furthermore, the energy cumulation observed in the internal air is more intense, which are of the order of 10^{-3} °C at both point A and point B, compared to Test 1.

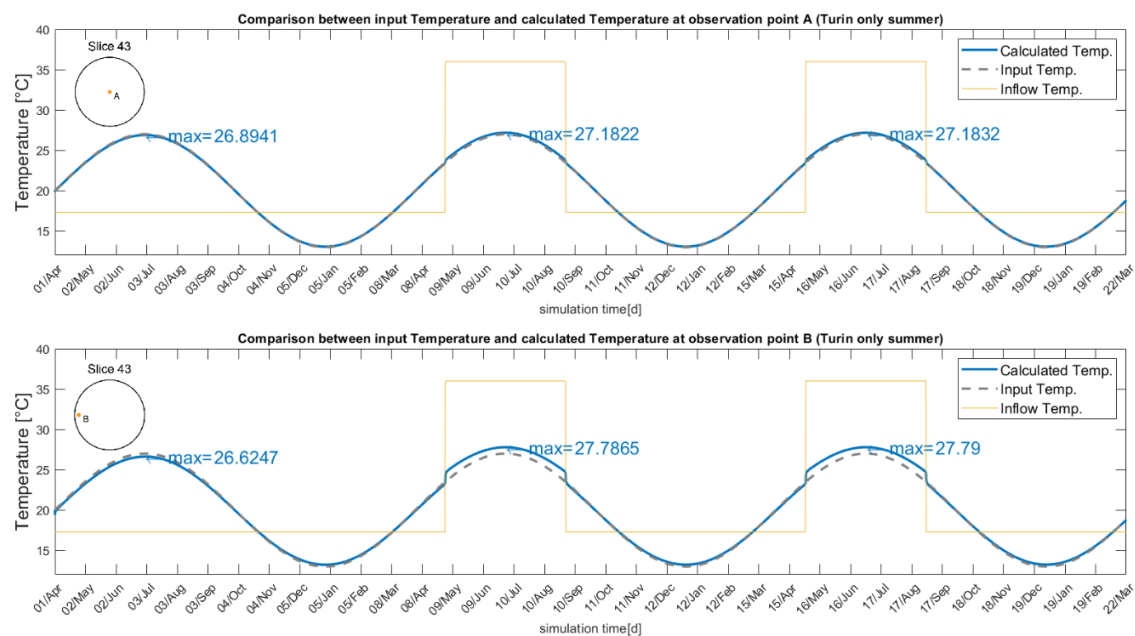


Fig. 71. Temperature variation at observation points A&B - Test 10

The temperature history plot of Test 11 is shown in **Fig. 72**. As it is expected, the effect of thermal activation in winter on the internal air is also stronger with Air configuration than that with Ground configuration. The temperature variations are approximately $-0.32\text{ }^{\circ}\text{C}$ at point A and $-1.29\text{ }^{\circ}\text{C}$ at point B. Similarly, energy cumulation is not observed in this test as it is in Test 2.

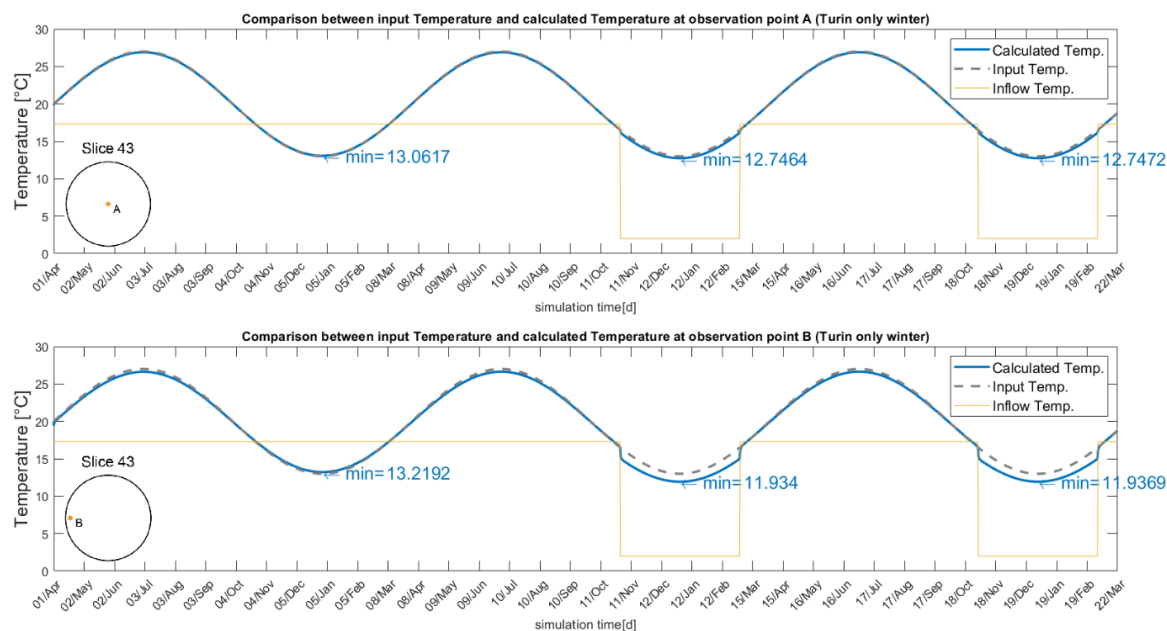


Fig. 72. Temperature variation at observation points A&B - Test 11

The temperature history plot of Test 12 is shown in **Fig. 73**. As it is observed, again, the thermal activation in both summer and winter will not bring different effect to the internal air compared to thermal activation in summer and winter separately. The temperature variations in summer and winter are of the same value as they are in Test 10 and 11, which are approximately $+0.29\text{ }^{\circ}\text{C}$ at Observation point A and $+1.17\text{ }^{\circ}\text{C}$ at Observation point B in summer and approximately $-0.32\text{ }^{\circ}\text{C}$ at Observation point A and $-1.29\text{ }^{\circ}\text{C}$ at Observation point B in winter. It is worth pointing out that, similarly like in Test 3, the energy cumulation phenomenon is observed in only summer again with the order of $10^{-3}\text{ }^{\circ}\text{C}$ at both point A and point B.

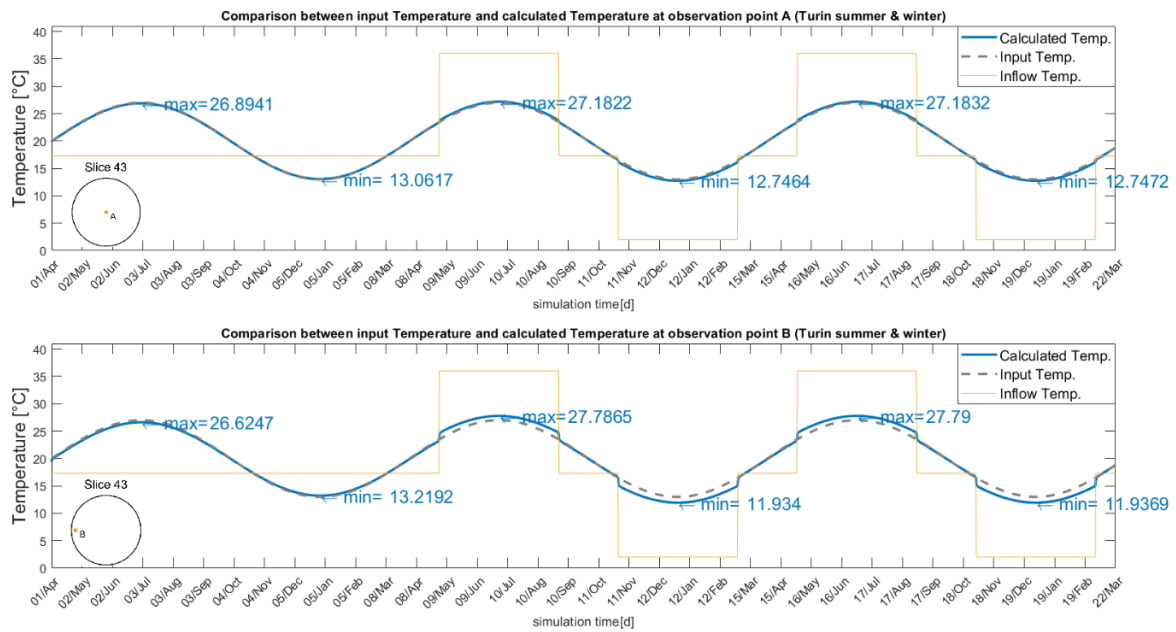


Fig. 73. Temperature variation at observation points A&B - Test 12

For Test 13, 14 and 15, the input temperature of external air and internal air inside tunnel are reduced by 3 °C while the temperature of ground remains as 17.3 °C. The 3D temperature field of Test 13 at the end of the simulation test is shown in **Fig. 74**, in which we can observe the similar temperature field and color scale as in Test 4 with the same input data and Ground configuration.

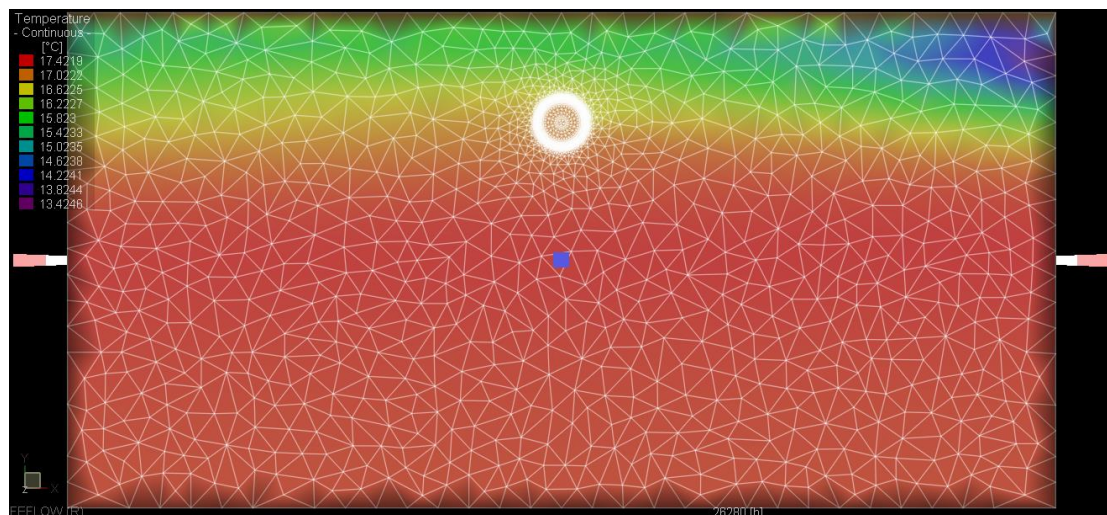


Fig. 74. Temperature field of the 3D model - Test 13

The temperature history plot of Test 13 is shown in **Fig. 75**. Hence a greater temperature variation of the internal air due to the thermal activation in summer and a smaller one in winter compared to Test 9, 10 and 11 are expected. As it is observed in **Fig. 75**, the temperature variations of the internal air due to thermal activation in summer are approximately $+0.35\text{ }^{\circ}\text{C}$ at Observation point A and $+1.41\text{ }^{\circ}\text{C}$ at Observation point B, which meets the expectation. Furthermore, energy cumulation is no longer observed in summer with the reduction of the input temperature. The same phenomenon is observed in Test 4 with the same input temperature but different thermal pipe circuit in use.

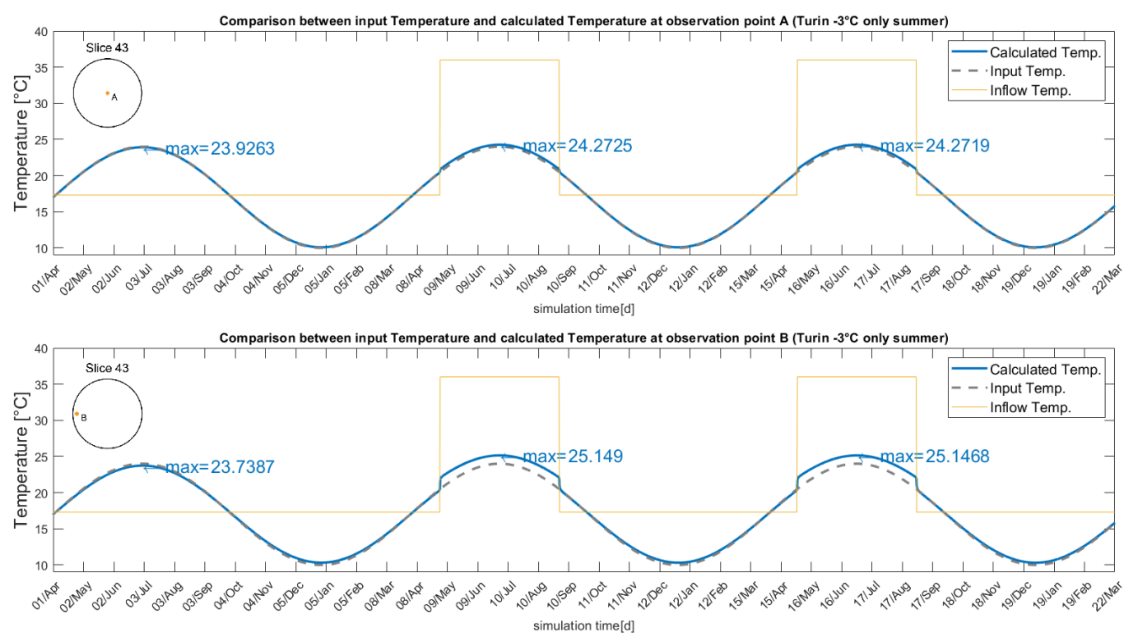


Fig. 75. Temperature variation at observation points A&B - Test 13

The temperature history plot of Test 14 is shown in **Fig. 76**. Due to the reduction of the input temperature, with the same temperature of ground as 17.3°C , the temperature variation in the internal air due to thermal activation in winter does reduce compared to Test 11. They are approximately $-0.25\text{ }^{\circ}\text{C}$ at point A and $-1.03\text{ }^{\circ}\text{C}$ at point B. The energy cumulation phenomenon is observed but with a lower intensity as well, which are of the order of $10^{-4}\text{ }^{\circ}\text{C}$ at point A and $10^{-3}\text{ }^{\circ}\text{C}$ at point B.

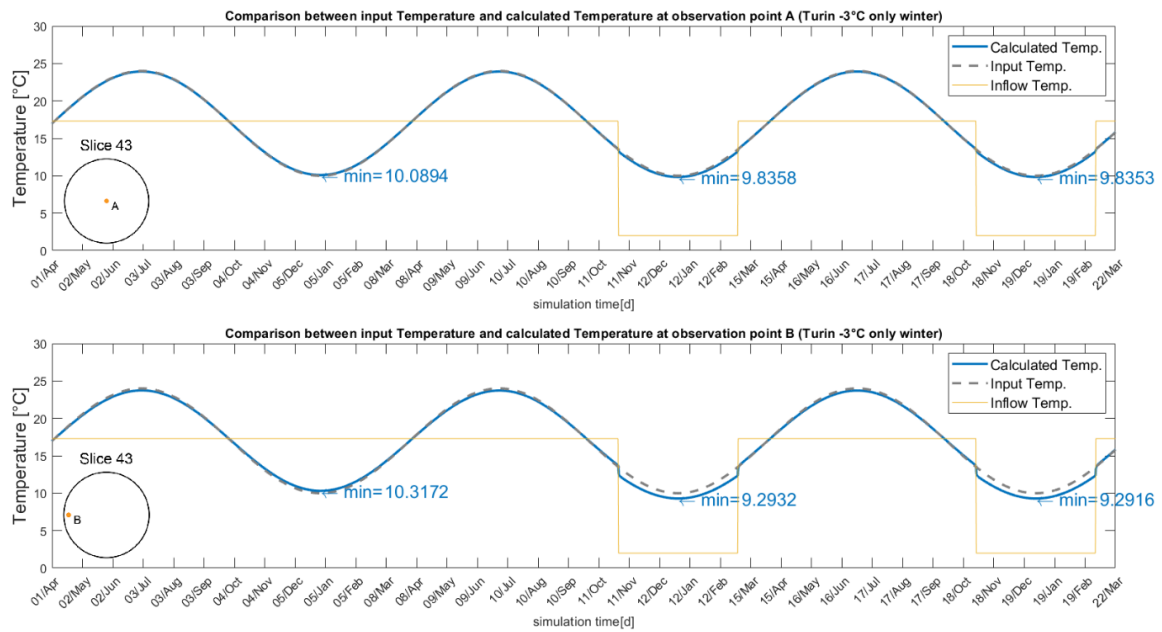


Fig. 76. Temperature variation at observation points A&B - Test 14

The temperature history plot of Test 15 is shown in **Fig. 77**. Again, thermal activation in both summer and winter does not lead to a different effect of temperature variation in the internal air compared to thermal activation in summer and winter separately. The temperature variations of the internal air are approximately +0.35 °C at Observation point A and +1.41 °C at Observation point B in summer and approximately -0.25 °C at Observation point A and -1.03 °C at Observation point B in winter. The energy cumulation is observed in only winter as well with the same quantity of those observed in Test 15.

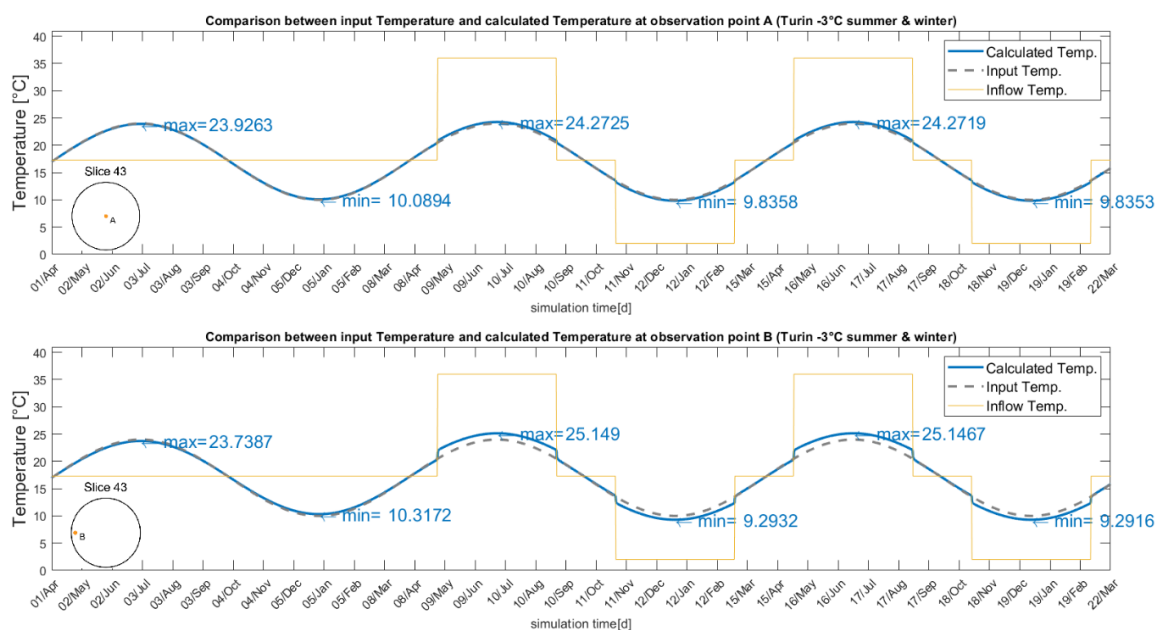


Fig. 77. Temperature variation at observation points A&B - Test 15

Generally, the effect of thermal activation on the internal air are amplified in summer and are conversely reduced in winter due to the reduction of the input temperature compared to Test 10, 11 and 12. Meanwhile, the level of energy cumulation is lowered as well.

Moreover, the simulation tests with an increased input temperature, with the ground temperature remains as 17.3 °C, were performed seen as Test 16, 17 and 18. A reverse effect, which are higher temperature variation due to thermal activation in winter and lower temperature variation in summer, can be expected compared to reduction of the input temperature.

The 3D temperature field of Test 16 at the end of the simulation test is shown in **Fig. 78**, similar as that of Test 7 since the same input data is used but with Air configuration.

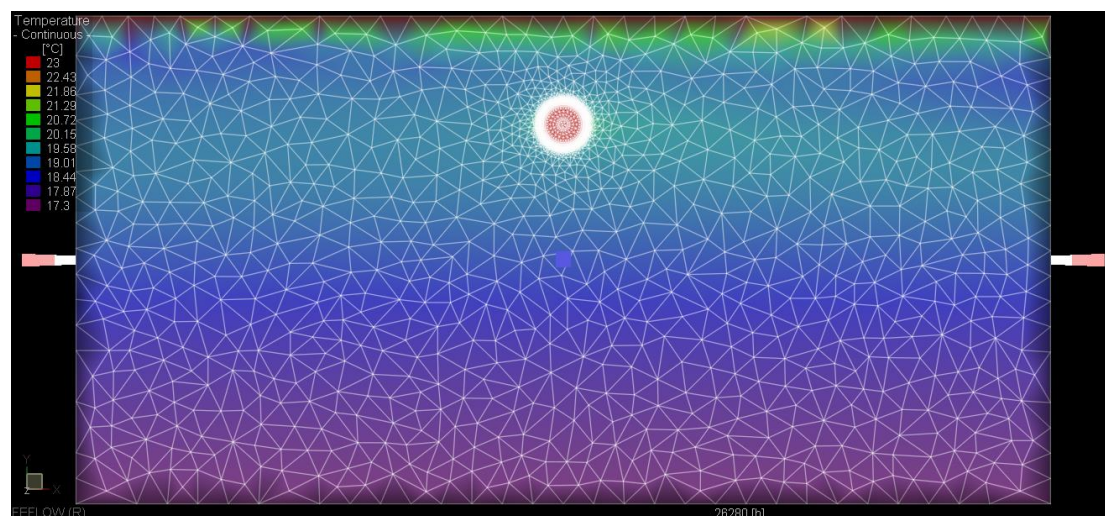


Fig. 78. Temperature field of the 3D model - Test 16

The temperature history plot of Test 16 is shown in **Fig. 79**. As expected, the effect of thermal activation on the internal air under such input temperature is lower than those found in Test 10 and 13. The temperature variation are approximately +0.23 °C at point A and +0.92 °C at point B. However, the energy cumulation is higher in this case, which are of the order of 10^{-3} °C at point A and almost 10^{-2} °C at point B.

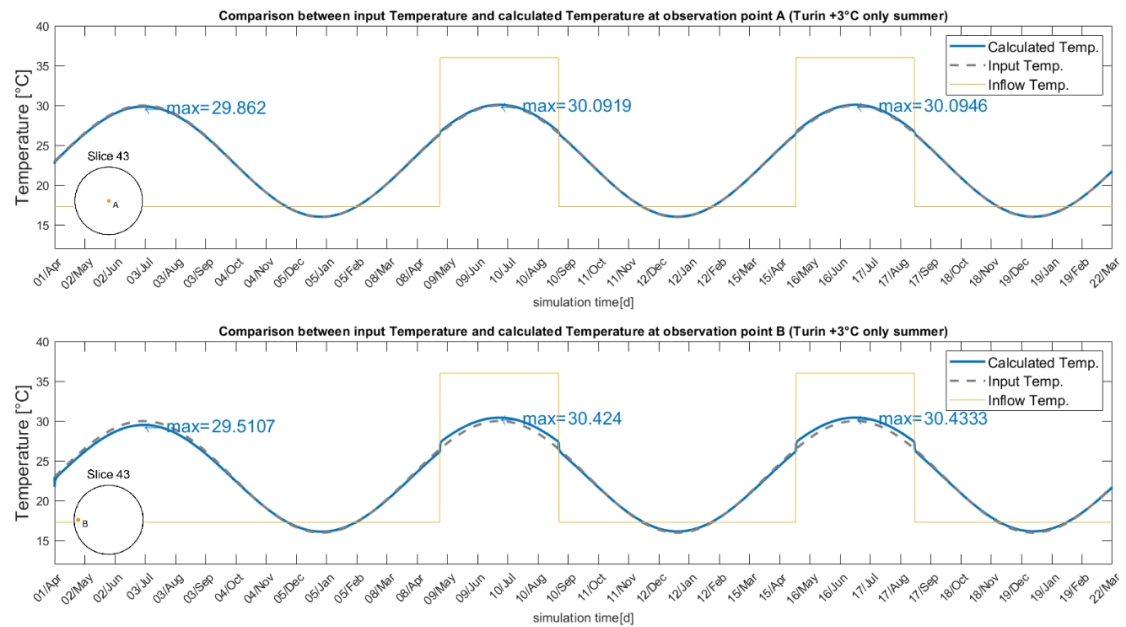


Fig. 79. Temperature variation at observation points A&B - Test 16

The temperature history plot of Test 17 is shown in **Fig. 80**. The temperature variation of the internal air in winter is greater than in Test 11 and 14 as expected in this case, which are approximately -0.38 °C at point A and -1.55 °C at point B. The energy cumulation phenomenon is not found in this test.

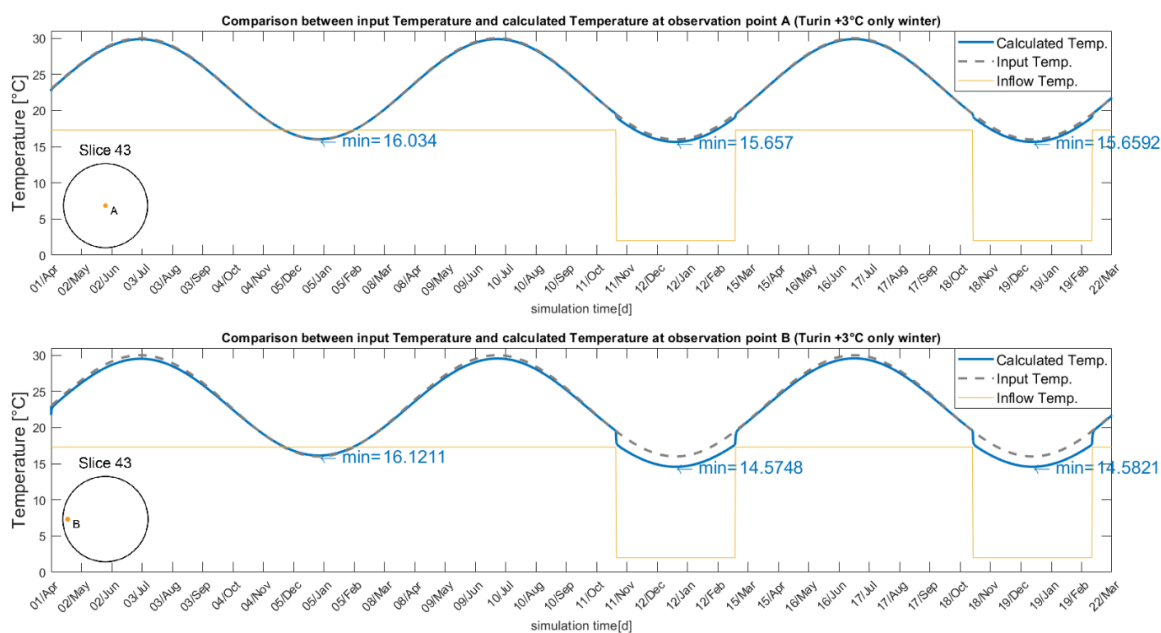


Fig. 80. Temperature variation at observation points A&B - Test 17

The temperature history plot of Test 18 is shown in **Fig. 81**. Without surprise, thermal activation in both summer and winter leads to the same effect as it possesses in summer and winter separately both in terms of temperature variation and energy cumulation. The temperature variation in this test are approximately +0.23 °C at Observation point A and +0.92 °C at Observation point B in summer and approximately -0.38 °C at Observation point A and -1.55 °C at Observation point B in winter. The energy cumulation is of the order of 10^{-3} °C at point A and almost 10^{-2} °C at point B.

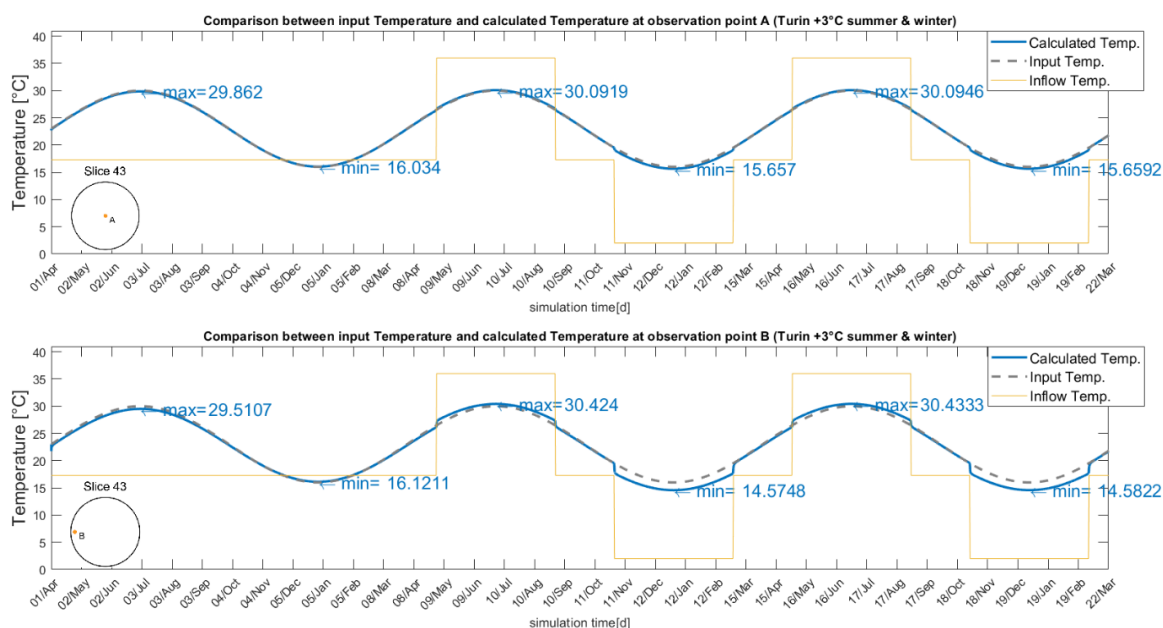


Fig. 81. Temperature variation at observation points A&B - Test 18

As found in Test 16, 17 and 18, the effect due to the increase in the input temperature leads to a stronger effect of thermal activation on the internal air in winter in terms of temperature variation and a lower one in summer, which can be expected. However, a lower temperature variation does not necessarily mean a lower level of energy cumulation. In fact, the energy cumulation in summer is even higher in Test 16 and 18.

Predictably, the effect of thermal activation with Air configuration on the internal air is generally stronger than that with Ground configuration. With Air configuration, the intensity of temperature variation is around ± 0.3 °C at point A and ± 1.2 °C at point B. Meanwhile, the level of energy cumulation in the internal air rises up to the order of 10^{-3} °C at both point A and point B in general.

Furthermore, it is also worth investigating the effect due to the internal air flow velocity, which is apparently another main feature influencing the response of internal air to the thermal activation of tunnel lining.

To maximize the effect, the internal air flow velocity is set to be 0 and Air configuration, which gives rise to a stronger influence on the internal air, is implemented as seen in Test 19.

The temperature history plot of Test 19 is shown in **Fig. 82**. As it is observed, without the input air flow, say, without the convection inside the internal air, the internal air temperature at the middle length of the tunnel is barely influenced by the input temperature applied at the first slice. The oscillation of the internal air temperature due to season change is weak and greatly delayed, especially at point B. Both for point A and B, before the thermal activation, the internal air temperature is around 18 °C with little fluctuation. Furthermore, the effect of thermal activation on the internal air is dramatically increased. The temperature variations are approximately +13.58 °C at Observation point A and +14.85 °C at Observation point B in summer and approximately -12.09 °C at Observation point A and -13.32 °C at Observation point B in winter. Moreover, it takes a longer time for the internal air temperature to return to the normal temperature level after the thermal activation. In terms of energy cumulation, it is of the order of 10^{-2} °C both at point A and point B in summer.

Such result shows that the insulating effect of the static air is quite strong. Furthermore, since the observation points are far away from the slice 1 where the input internal air temperature is applied but closer to the tunnel lining, the effect from lining to the internal air is more relevant. It is also worth pointing out that the thermal capacity of heat carrier fluid is much higher than that of air, which provides a much higher energy level for the heat carrier fluid with the applied temperature.

However, the internal air temperature should not reach the same temperature as the inflow fluid temperature, since it gets stable a few hours after the thermal pipe circuit is activated and remain at approximately the same level all along the thermal activation period. Furthermore, the flowing ground water takes a part of the heat from the heat carrier fluid as well.

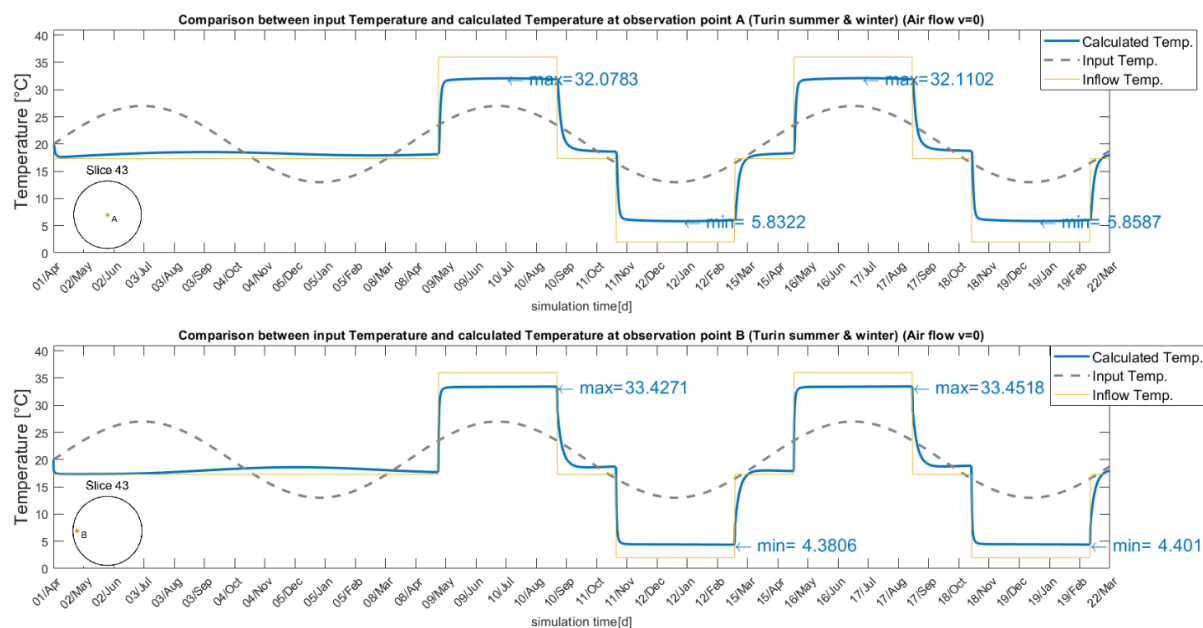


Fig. 82. Temperature variation at observation points A&B - Test 19

Apart from the static air condition, another test is performed with the air flow velocity of 0.0001 m/s seen as Test 20, which also aims to examine the influence of the air flow velocity on the internal air temperature under thermal activation of tunnel lining. The temperature history plot of Test 20 is shown in **Fig. 83**. The temperature variations are approximately +4.63 °C at Observation point A and +14.85 °C at Observation point B in summer and approximately -4.12 °C at Observation point A and -12.44 °C at Observation point B in winter.

Differently from Test 19, seasonal oscillation of the internal air temperature can be observed clearly at observation point A, though the amplification does not reach the input temperature level. It is rather staggering that such a small air flow velocity can bring such a great difference in the result. However, the temperature history observed at point B is similar to that observed in Test 19, apparently since that point B is much closer to the lining intrados and consequently more influenced by the tunnel linings.

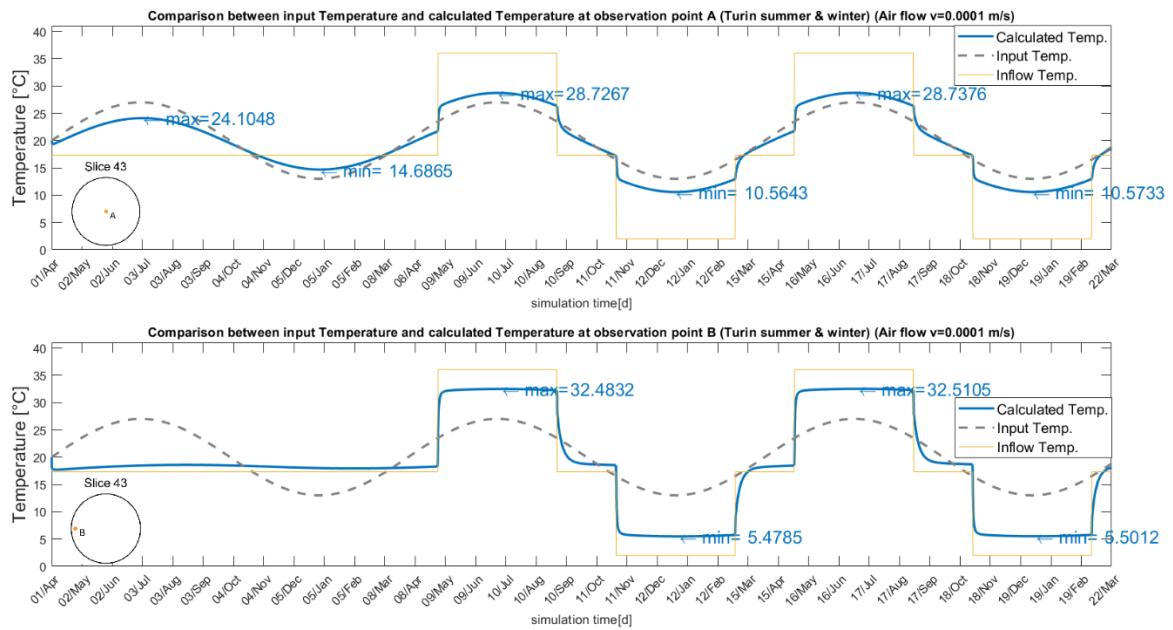


Fig. 83. Temperature variation at observation points A&B - Test 20

All the interpretation results of different simulation tests with Air configuration are summarized in **Table 8** for observation point A and in **Table 9** for observation point B, respectively.

Table 8 Test interpretation result summary (Observation point A, Air configuration)

| Test number | Peak (normal summer) | Lowest (normal winter) | Peak (thermo-active summer) | Lowest (thermo-active winter) | Variation (summer) | Variation (winter) | Order of cumulation |
|-------------|----------------------|------------------------|-----------------------------|-------------------------------|--------------------|--------------------|---------------------|
| - | [°C] | [°C] | [°C] | [°C] | [°C] | [°C] | [°C] |
| 10 | 26.8941 | - | 27.1832 | - | 0.2891 | - | 1.00E-03 |
| 11 | - | 13.0617 | - | 12.7464 | - | -0.3153 | - |
| 12 | 26.8941 | 13.0617 | 27.1832 | 12.7464 | 0.2891 | -0.3153 | 1.00E-03 |
| 13 | 23.9263 | - | 24.2725 | - | 0.3462 | - | - |
| 14 | - | 10.0894 | - | 9.8353 | - | -0.2541 | 1.00E-04 |
| 15 | 23.9263 | 10.0894 | 24.2725 | 9.8353 | 0.3462 | -0.2541 | 1.00E-04 |
| 16 | 29.862 | - | 30.0946 | - | 0.2326 | - | 1.00E-03 |
| 17 | - | 16.034 | - | 15.657 | - | -0.377 | - |
| 18 | 29.862 | 16.034 | 30.0946 | 15.657 | 0.2326 | -0.377 | 1.00E-03 |
| 19 | 18.53 | 17.92 | 32.1102 | 5.8322 | 13.5802 | -12.0878 | 1.00E-02 |
| 20 | 24.1048 | 14.6865 | 28.7376 | 10.5643 | 4.6328 | -4.1222 | 1.00E-02 |

Table 9 Test interpretation result summary (Observation point B, Air configuration)

| Test number | Peak (normal summer) | Lowest (normal winter) | Peak (thermo-active summer) | Lowest (thermo-active winter) | Variation (summer) | Variation (winter) | Order of cumulation |
|-------------|----------------------|------------------------|-----------------------------|-------------------------------|--------------------|--------------------|---------------------|
| - | [°C] | [°C] | [°C] | [°C] | [°C] | [°C] | [°C] |
| 10 | 26.6247 | - | 27.79 | - | 1.1653 | - | 1.00E-03 |
| 11 | - | 13.2192 | - | 11.934 | - | -1.2852 | - |
| 12 | 26.6247 | 13.2192 | 27.79 | 11.934 | 1.1653 | -1.2852 | 1.00E-03 |
| 13 | 23.7387 | - | 25.149 | - | 1.4103 | - | - |
| 14 | - | 10.3172 | - | 9.2916 | - | -1.0256 | 1.00E-03 |
| 15 | 23.7387 | 10.3172 | 25.149 | 9.2916 | 1.4103 | -1.0256 | 1.00E-03 |
| 16 | 29.5107 | - | 30.4333 | - | 0.9226 | - | 1.00E-03 |
| 17 | - | 16.1211 | - | 14.5748 | - | -1.5463 | - |
| 18 | 29.5107 | 16.1211 | 30.4333 | 14.5748 | 0.9226 | -1.5463 | 1.00E-03 |
| 19 | 18.6 | 17.7 | 33.4518 | 4.3806 | 14.8518 | -13.3194 | 1.00E-02 |
| 20 | 18.56 | 17.92 | 32.5105 | 5.4785 | 13.9505 | -12.4415 | 1.00E-02 |

5.5 Conclusions from the simulation tests

- Thermal activation with Ground configuration leads to a temperature variation in the internal air at middle length of tunnel with the intensity of around $\pm 0.2^{\circ}\text{C}$ at the tunnel center and $\pm 0.8^{\circ}\text{C}$ close to the lining intrados, while the input temperature variation of $\pm 3^{\circ}\text{C}$ leads to a temperature variation in the internal air of the range of around $\pm 0.03^{\circ}\text{C}$ at the tunnel center and $\pm 0.13^{\circ}\text{C}$ close to the lining intrados, when internal air flow velocity equals to 0.1 m/s.
- Thermal activation with Air configuration leads to a stronger temperature variation in the internal air at middle length of tunnel with the intensity of around $\pm 0.3^{\circ}\text{C}$ at the tunnel center and $\pm 1.2^{\circ}\text{C}$ close to the lining intrados, while the input temperature variation of $\pm 3^{\circ}\text{C}$ leads to a temperature variation in the internal air of the range of around $\pm 0.06^{\circ}\text{C}$ at the tunnel center and $\pm 0.24^{\circ}\text{C}$ close to the lining intrados, when internal air flow velocity equals to 0.1 m/s.
- Energy cumulation due to continuous thermal activation is observed in some cases but with a rather small intensity ranging from 10^{-4}°C to 10^{-3}°C .
- Internal air flow velocity can influence the result strongly. Under the static air condition, without the convection due to the internal air flow inside the tunnel, the temperature variation due to thermal activation of the tunnel lining dramatically increases up to more than 10°C . Moreover, since there is only conduction inside the tunnel opening, the seasonal oscillation of the internal air temperature is barely seen and greatly delayed. While with a rather small internal air flow of 0.0001 m/s, such temperature variation at the tunnel center of middle length reduces down to approximately 4.6°C .

Conclusions

A numerical study on the role of the internal air inside a thermo-active tunnel was performed with the software of finite-element modelling under the function of thermo-hydraulic analysis, in order to reveal the mutual effect between the internal air of tunnel and the tunnel linings equipped with pipe circuit circulating the heat carrier fluid. The main conclusions are followed:

- Thermal activation of tunnel lining can influence the internal air temperature inside the tunnel, while the intensity varies depending on the pipe circuit configuration to be implemented, the input temperature data, the internal air flow velocity, etc.
- Thermal activation with Air configuration leads to a stronger effect on the internal air compared with Ground configuration. When the applied internal air flow velocity equals to 0.1 m/s and the simplified temperature data of Turin is implemented, the thermal activation with Air configuration leads to a temperature variation of approximately $\pm 0.3^{\circ}\text{C}$ at the tunnel center and $\pm 1.2^{\circ}\text{C}$ close to the lining intrados in the internal air at the middle length of the tunnel, while that with Ground configuration leads to a temperature variation of approximately $\pm 0.2^{\circ}\text{C}$ and $\pm 0.8^{\circ}\text{C}$ at the same observation points.
- Different input temperature ($\pm 3^{\circ}\text{C}$ based on the simplified external and internal air temperature of Turin) leads to a different temperature variation in the internal air due to thermal activation. Depending on the season and the thermal activation mode, the intensity of such effect is different. The range of such additional temperature variation are around $\pm 0.06^{\circ}\text{C}$ at the tunnel center and $\pm 0.24^{\circ}\text{C}$ close to the lining intrados with Air configuration, while those with Ground configuration is relatively less intense. To be noted that, the total temperature variation considering the varied input temperature is the sum of the base temperature variation with the simplified temperature data of Turin and the additional temperature variation.
- Energy cumulation due to continuous thermal activation is observed in some cases with a minor intensity ranging from 10^{-4}°C to 10^{-3}°C , when internal air flow velocity equals to 0.1 m/s.
- With the model built in this thesis, the internal air flow is found to be a strong factor influencing the response of internal air to thermal activation of tunnel lining. When the internal air flow is absent, the static air acts as a strong insulating media. As a result, the air at middle length of the tunnel can barely follow the seasonal oscillation of the input temperature and is strongly influenced by the thermal activation of tunnel lining with a temperature variation of more than 10°C . It is worth pointing out that the huge difference of the thermal capacity between the heat carrier fluid and air also contributes to such a strong temperature variation, since the great amount of heat applied through Temperature BC on the heat carrier fluid can easily heat up or cool down the internal air. However, the internal air at observation point will not reach the same temperature as the heat carrier fluid since a great part of the heat is absorbed by the flowing ground water.

- With a rather small air flow of 0.0001 m/s inside the tunnel opening, the temperature variation due to thermal activation drops down to approximately 4.7 °C, which demonstrates again a strong influence of the internal air flow on the response of internal air to the thermal activation.
- Based on the assumption of this thesis and the numerical result from the model built up in this thesis, various factors can influence the test results while the internal air flow velocity is one of the most relevant. However, a lot of simplifications were made and the boundary conditions applied may not be able to fully describe the realistic situations of the site. For example, the internal air flow velocity may not be uniform among the tunnel opening in the radial direction. Also, the heat transfer efficiency between the internal air and the tunnel linings is yet to be examined as well.

Reference

- Barla, M., Di Donna, A., & Insana, A. (2019). A novel real-scale experimental prototype of energy tunnel. *Tunnelling and Underground Space Technology*, 87, 1-14.
- Barla, M., & Di Donna, A. (2018). Energy tunnels: concept and design aspects. *Underground Space*, 3(4), 268-276.
- Barreca, D. (2017). *Gallerie energetiche: Studio dell'influenza dell'attivazione termica sulla temperatura dell'aria interna*. Politecnico di Torino, Torino.
- Brandl, H. (2006). Energy foundations and other thermo-active ground structures. *Géotechnique*, 56, 81–122.
- Crandall, A.C. (1946). House Heating with Earth Heat Pump. *Electrical World*, 126/19, 94-95.
- Di Donna, A., Cecinato, F., Loveridge, F., & Barla, M. (2016). Energy performance of diaphragm walls used as heat exchangers. *Proceedings of the Institution of Civil Engineers - Geotechnical Engineering*, 170(3), 232-245.
- Florides, G., & Kalogirou, S. (2007). Ground heat exchangers-a review of systems, models and applications. *Renew Energy*, 32(15), 2461–2478.
- Franzius, J. N., & Pralle, N. (2011). Turning segmental tunnels into sources of renewable energy. *Proceedings of the Institution of Civil Engineers*, 164, 35–40.
- Insana, A. (2020). *Thermal and Structural Performance of Energy Tunnels*. Politecnico di Torino, Torino.
- Insana, A., & Barla, M. (2020). Experimental and numerical investigations on the energy performance of a thermo-active tunnel. *Renewable Energy*, 152, 781-792.
- Kemler, E.N. (1947). Methods of Earth Heat Recovery for the Heat Pump. *Heating and Ventilating*, 9/1947, 69-72.
- Lee, K.S. (2013). Underground Thermal Energy Storage. In *Underground Thermal Energy Storage* (pp. 15-26). Green Energy and Technology. Springer, London.
- Lee, C., Park, S., Won, J., Jeoung, J., Sohn, B., & Choi, H. (2012). Evaluation of thermal performance of energy textile installed in Tunnel. *Renewable Energy*, 42, 11–22.
- Markiewicz, R., & Adam, D. (2009). Energy from earth-coupled structures, foundations, tunnels and sewers. *Géotechnique*, 59, 229–236.
- Ohnishi, Y., & Kobayashi, A.R. (1993). 7 - Thermal–Hydraulic–Mechanical Coupling Analysis of Rock Mass. In C. Fairhurst (Eds.), *Analysis and Design Methods* (pp. 191-208). Pergamon.
- Rosso, E. (2020). *Gallerie energetiche: ottimizzazione termo-idraulica e studio del comportamento stagionale*. Politecnico di Torino, Torino.
- Sanner, B. (2017). Ground Source Heat Pumps – history, development, current status and future prospects. *12th IEA Heat Pump Conference 2017*.
- Sanner, B., & Nordell, B. (1998). Underground thermal energy storage with heat pumps, *IEA Heat Pump Cent. Newsl*, 16(2), 10–14.

- Wang, G., Wang, W., Luo, J., & Zhang, Y. (2019). Assessment of three types of shallow geothermal resources and ground-source heat-pump applications in provincial capitals in the Yangtze River Basin, China. *Renewable and Sustainable Energy Reviews*, 111, 392-421.
- Zhang, G., Xia, C., Sun, M., Zou, Y., & Xiao, S. (2013). A new model and analytical solution for the heat conduction of tunnel lining ground heat exchangers. *Cold Regions Science and Technology*, 88, 59–66.